Multi-scale Characterization Studies of Aged Li-ion Battery Materials for Improved Performance

Dissertation

Presented in Partial Fulfillment of the Requirements for the Degree Doctor of Philosophy in the Graduate School of The Ohio State University

By

Shrikant C. Nagpure, M.S

Graduate Program in Mechanical Engineering

The Ohio State University

2012

Dissertation Committee:

Prof. Bharat Bhushan, Advisor

Prof. Sudarsanam Suresh Babu, Co-advisor

Prof. Giorgio Rizzoni

Prof. Yann Guezennec

© Copyright by

Shrikant C. Nagpure

2012

Abstract

Among various electrical energy storage devices the recent advances in Li-ion battery technology has made this technology very promising. Li-ion batteries can be used in stationary applications such as conventional or renewable energy power plants or also in development of electric vehicles. The advantage of these batteries is high energy and power density. As these batteries are deployed in various applications there is a need to understand the aging mechanisms of these batteries to improve the cycle life. Aging of the cells at the macroscopic or system level is quantified by the change in the internal resistance measured by impedance techniques. To understand the related loss of capacity, it is imperative to understand the degradation of the electrode materials of the battery. The degradation of the material is caused by several simultaneous physiochemical processes that occur within the batteries which makes material characterization of the electrodes a challenging task.

Performance of any new electrode material is investigated by testing the materials in a small experimental (so-called coin) cell. In commercial batteries the electrodes are made up of nanomaterials to leverage the effects of high surface area. Thus commercial batteries are larger in size as they provide the necessary building blocks for the battery packs. The effects of scaling in the commercial cell might be overlooked

if the results of the so-called coin cell experiments are to be believed alone. This further adds to the complexity of analyzing the degradation mechanisms in commercial batteries.

As such a systematic multi-scale characterization plan has been developed to understand the degradation mechanisms of the battery. Various materials characterization techniques have been chosen to understand the degradation at a particular length scale and providing a direction for higher length scales. Along with certain physical and morphological characterization, techniques that characterize the functional properties such as resistance and surface potential has also been included in this scheme of multi-scale techniques. Certain chemical characterization techniques are also included to understand the chemical changes during the life of the battery. This thesis provides an discussion of these various techniques and an overview of the degradation studies of Li-ion batteries.

Dedicated to my parents

Chandrakant Nagpure and Jayashree C. Nagpure

and my sister

Vijaya C. Nagpure

Acknowledgments

First and foremost I would like to thank my parents and sister for their continuous encouragement, patience, guidance. This opportunity has turned into a reality because of their blessings and support. I am indebted to them forever.

This work would not have been possible without the opportunity offered to me by Prof. Bhushan. I am thankful to him for this opportunity and the faith he has showed in me while developing, planning and fulfilling the challenges of this cutting-edge research in the field of energy materials. His expertise and energy has driven me through this work to achieve the goals in ambitious time frame. He will for always remain as one of the sources of inspiration for hard work and dedication for my research activities.

This entire dissertation plan would not have started without the leadership, and foresight shown by Prof. Rizzoni. I truly admire, appreciate and thank him for his support and guidance in developing my dissertation. I am thankful to Prof. Babu who has helped me at every step of my research. I thank him for his mentoring at every step of this work and his guidance in expanding the horizons of my research activities. I am also thankful to Prof. Guezennec for his support, advising and assistance. I thank Prof. Noltimier for serving as the Graduate school representative and providing detailed comments on my dissertation.

My topic required an interdisciplinary approach. As such a collaboration was sought between Mechanical engineering, Nuclear Engineering and Material Science Engineering. This collaboration was successful due to the interest and dedication shown by different team members. I am thankful to my collaborators, Prof. Windl, Rohan Mishra, Ashutosh Kumar and Libor Kovarik from Material Science Engineering and Dr. Cao and Danyal Turkoglu from Nuclear Engineering.

I am also thankful to Caterina Runyon-Spears for preparing manuscripts for my various publications. I am also thankful to support staff at Center for Automotive Research. I would also like to express sincere thanks to my colleagues in Nanoprobe Laboratory for Bio- and Nanotechnology and Biomimetics, Center for Automotive Research and Prof. Babus group.

I have met some incredible personalities outside The Ohio State University while conducting this research and they have influenced me forever. I am blessed to have an opportunity to work with Dr. Gregory R. Downing at National Institute of Standards and Technology who, I thank for this mentorship and teachings of conducting scientific experimental work. I am also thankful to Tim Frech from Edison Welding Institute for his timely help with various environmental and sample storage devices. I am also thankful to Dr. Ralph Dinwiddie from Oak Ridge National Laboratory for his support during the initial stages of this research work.

Last but not least I take this opportunity to thank many of my friends who have supported me and encouraged me during my time at The Ohio State University. I would like to extended my gratitude to my childhood friend Gajanan Keskar. He has always stood by me and encouraged me in my difficult times. I am thankful to Parag Kandekar who has always motivated me in achieving my goals. I am grateful

to Anurag Chandorkar, Prashant Patel and Deepak Devasagayam for their support and encouragement. I am also thankful to Sandip Bapat and Niket Khanolkar for making my stay in Columbus calm, peaceful and enjoyable.

Vita

July 11, 1979	Born - Pune, India
2000	B.E. Mechanical Engineering, University of Pune
2005	M.S. Mechanical Engineering, Old Dominion University
2006-present	Graduate Research Assistant, The Ohio State University

Publications

Journal Publications

1. Nagpure, S. C., Bhushan, B., Babu, S., and Rizzoni, G., "Scanning Spreading Resistance Characterization of Aged Li-ion Batteries using Atomic Force Microscopy," *Scripta Mater* **60**, 933-936 (2009).

2. Nagpure, S. C., Dinwiddie, R., Babu, S., Rizzoni, G., Bhushan, B., and Frech, T., "Thermal Diffusivity Study of Aged Li-Ion Batteries using Flash Method," *J Power Sources* **195,** 872-876 (2010).

3. Nagpure, S. C., Bhushan, B., and Babu, S.S., "Surface Potential Measurement of Aged Li-ion Batteries using Kelvin Probe Microscopy," *J Power Sources* **196,** 1508-1512 (2011).

4. Nagpure, S.C., Downing, R.G., Bhushan, B., Babu, S.S., and L. Cao, "Neutron Depth Profiling Technique for Studying Aging in Li-Ion Batteries," *Electrochim Acta* **56(13),** 4735-4743 (2011).

5. Nagpure, S.C., Babu, S.S., Bhushan, B., Kumar, A., Mishra, R., Windl, W., Kovarik, L., and Mills, M., "Local Electronic Structure of $LiFePO_4$ Nanoparticles in Aged Li-Ion Batteries," *Acta Mater* **59,** 6917-6926 (2011).

6. Nagpure, S. C., Bhushan, B, and Babu, S. S., "Raman Spectroscopy of Carbon Coating on the Cathode during Aging of Li-Ion Batteries," (*submitted for publication*).

Book Chapters

1. Nagpure, S.C. and Bhushan B., (2009), Applied Scanning Probe Methods - Biomimetics and Industrial Applications, Bhushan, B. and Fuchs, H. (Eds.) vol. 13, Springer- Verlag, Heidelberg, pp. 203-233.

2. Nagpure, S. C. and Bhushan, B. (2012), Encylopedia of Nanotechnology, Bhushan, B. (Eds.) Springer-Verlag, Heidelberg (in press).

Fields of Study

Major Field: Mechanical Engineering

Table of Contents

Page

Abstract ii

Dedication iv

Acknowledgments v

Vita viii

List of Tables xiii

List of Figures xiv

Acronyms xx

1. Introduction 1

2. Electrical Energy Storage Devices 5

2.1 Electrochemical double layer capacitors 5
2.2 Fuel cell 8
2.3 Batteries 11
2.3.1 Lead-acid 11
2.3.2 Nickel-Cadmium 12
2.3.3 Nickel-Metal Hydride 12
2.3.4 Lithium-ion 13
2.4 Comparison of different electrochemical energy storage devices Ragone plot 17

3. Li-ion Batteries 20

3.1 Electrochemistry of Li-ion batteries 20
3.2 Requirements of automobile industry 22

4. Materials for Li-ion Batteries 24

4.1 Anode 25
4.2 Cathode 27
4.3 Electrolytes 29

5. Aging Cycles for Li-ion Batteries 33

6. Multi-scale Characterization of Cathode - Physical and Morphological . . 38

6.1 Introduction 38
6.2 Thermography (mm) 45
6.3 Digital microscopy (microns) 53
6.4 Scanning electron microscopy (SEM) (microns) 56
6.5 Atomic force microscopy (AFM) (micron nm) 57
6.6 Transmission electron microscopy (TEM) (nm) 60
6.7 Summary 62

7. Multi-scale Characterization of Cathode - Electrical 65

7.1 Introduction 65
7.2 System level capacity fade and resistance increase 65
7.3 Scanning spreading resistance microscopy (SSRM) 68
7.3.1 Kelvin probe microscopy (KPM) 72
7.4 Summary 79

8. Multi-scale Characterization of Cathode - Structural and Chemical . . . 81

8.1 Introduction 81
8.2 X-ray diffraction (XRD) 81
8.3 Raman Spectroscopy (RS) 82
8.4 Electron energy loss spectroscopy (EELS) (nm) 90
8.5 Nuclear Magnetic Resonance (NMR) 101
8.6 Neutron depth profiling (NDP) 106
8.7 Summary 122

9. Outlook and Summary 125

Appendices 129

A. A Guide to Understanding Battery Specifications 129

Bibliography 135

List of Tables

Table **Page**

2.1 Characteristics of commonly used rechargeable batteries [Buchmann, 2001] 14

2.2 Advantages and limitations of commonly used rechargeable batteries (Adapted from [Buchmann, 2001]) 16

4.1 Properties of certain anode materials suitable for lithium-ion batteries. [Adapted from [Mantia, 2008]] 27

4.2 Properties of certain cathode materials suitable for lithium-ion batteries. [Adapted from [Mantia, 2008]] 29

4.3 Properties of certain solvent and solutes for lithium-ion battery electrolytes. [Adapted from [Mantia, 2008]] 31

5.1 Aging cycles 37

8.1 Initial lattice parameters and relaxed lattice parameters for structures with varying lithium content obtained by generalized gradient approximation (GGA) with PW91 type of pseudopotentials, enhanced by a U term to include strong correlation effects (GGA+U). The structural co-ordinates were adapted from [Tang and Holzwarth, 2003] for $FePO_4$ and $LiFePO_4$, while the intermediate structures were created by subsequently removing lithium from $LiFePO_4$ structure. 95

List of Figures

Figure **Page**

1.1 A typical electrical power demand profile for a 24 hr period. During early morning hours the demand is below the capacity of the power plant while the demand is at peak in the evening around 6 PM. During off-peak hours an electrochemical energy storage (EES) device would store the energy and during the peak hours the EES will be discharged. Thus EES would level the load and the actual demand cycle will be as shown by the solid line. (adapted from [Whittingham, 2008]) 2

2.1 Schematic showing operation of an electrochemical capacitor (EC). During charging the ions in the electrolyte are attracted to the nanoporous electrodes with opposite charge. This creates the charge separation at the electrode-electrolyte interface and the energy is stored in EC. During discharging, as the electrons flow through the load the ions disperse in the electrolyte solution and the electrode-electrolyte interface fades 7

2.2 (a) Schematic showing operation of a solid oxide fuel cell (SOFC). Oxygen is reduced at cathode and the resulting O^{2-} ions are conducted through the solid oxide electrolyte membrane (SOM) to the anode where they are oxidized with the hydrogen to form water. (b) Schematic showing operation of a proton exchange membrane fuel cell (PEMFC). Hydrogen is oxidized at anode and the resulting H^{+} ions are conducted through the proton exchange membrane (PEM) to cathode where they are reduced with O to form water 10

2.3 Ragone chart showing the comparison of the power density and energy density for batteries, capacitors, and fuel cells and internal combustion engine. Energy density represents the capacity while power density represents the rate of the charging/discharging of EES device. [adapted from [Whittingham, 2011] 18

3.1 Schematic of intercalation-deintercalation process. During charging Li^+ ions are inserted in the anode structure by virtue of intercalation and during discharging, these Li^+ ions are removed from the anode structure by virtue of deintercalation and transferred to the cathode [Anonymous, 2007; Nagpure et al., 2011c] 22

5.1 Synthesis of aging cycle from real life driving cycle 35

6.1 (a) Schematic of a cylindrical lithium-ion battery. The components are rolled and packed in a cylindrical case. (b) Schematic of a prismatic lithium-ion battery. The components are stacked in layers and enclosed in a rectangular casing. (c) Schematic of a pouch cell. The components are stacked in layers and enclosed in a foil envelope [Anonymous, 2007] 40

6.2 (a) A picture of a typical cylindrical cell. The cell is typically referred to as 18650 where the diameter of the cell is 18 mm and the length is 1650 mm. The jelly roll of the cell components is also seen here. (b) A picture of the dissembled and unrolled components of the cell. The length strip on the left is the anode and the strip on the right is cathode. The length of each electrode is $\sim$ 1.5 m long and 25 mm wide 41

6.3 A chart displaying the various techniques useful at different length scales for multi-scale characterization of the materials 44

6.4 Schematic of thermal diffusivity measurement by Flash Method (adapted from [Anonymous, 1992]) 47

6.5 (a) Sectioning of the cathode for the thermal imaging. Section # 1 is near the core of the cylinder and section # 5 is near the out edge of the cylinder. (b) Thermal maps of unaged and aged cathode samples for all 5 sections 48

6.6 (a) Temperature rise curves for unaged and aged samples (section # 4). (b) Comparison of thermal diffusivity between unaged and aged samples 51

6.7 (a) Temperature rise curves for unaged and aged samples (section # 4). (b) Comparison of thermal diffusivity between unaged and aged samples 53

6.8 Digital micrographs of unaged and aged graphitic anode and $LiFePO_4$ cathode across the thickness 55

6.9 SEM micrographs of unaged and aged $LiFePO_4$ cathode samples extracted from section # 4 57

6.10 Principle of operation of a commercial AFM. (The schematic is for Multimode™ AFM (Veeco Instruments, Inc.). (Adapted from [Bhushan, 2008]) 58

6.11 Surface height maps of a $LiFePO_4$ cathode sample harvested from unaged and aged cells. A +1V DC bias is applied to the sample 59

6.12 Steps showing TEM sample preparation using FEI Helios 600™ dual beam focused ion beam system (FIB) 61

6.13 (a) TEM images of unaged and aged $LiFePO_4$ cathode samples at lower magnification (b) TEM images of unaged and aged $LiFePO_4$ cathode samples at higher magnification. The images are from the central area in (a) 62

6.14 (A schematic showing coarsening of the $LiFePO_4$ nanoparticles during aging of the battery. 63

7.1 (a) A typical set of discharge curves (voltage versus time) is shown. The knee of the voltage curve is approached faster as the capacity of the cell decreases. (b) Internal resistance increases with aging of the cells. 66

7.2 Capacity drop and resistance increase in cells C3 and C4 for multi-scale characterization studies 67

7.3 Schematic of the AFM-based resistance measurement technique where the surface height is measured in contact mode, and the resistance is measured by the current resulting from the applied sample DC bias voltage. (The schematic is for DimensionTM AFM (Veeco Instruments, Inc.). (Adapted from [Anonymous, 2004]) 70

7.4 Surface resistance maps of a $LiFePO_4$ cathode sample harvested from unaged and aged cells. A +1V DC bias is applied to the sample . . . 70

7.5 Schematic of a proposed mechanism explaining increase in the surface resistance of a $LiFePO_4$ cathode due to aging 71

7.6 (a) Schematic of the two pass interleave scan method used in KPM. (Adapted from Rice, 2002). (b) Electrostatic potential and interaction force between a conducting tip and a sample (for illustration $\Phi_{tip}\Phi_{sample}$ is assumed), (c) external DC voltage applied to nullify the force, and (d) external AC voltage with adjustable DC offset is applied to the tip which leads to its vibration. (Adapted from [Bhushan and Goldade, 2000]) 75

7.7 Surface potential map of the unaged (left column) and the aged (middle column) $LiFePO_4$ cathode samples with external voltage of +1.0 V and +3.3 V The data for sample without any external voltage is shown for comparison. The right column shows the normal probability density distribution of the surface potential values obtained for the unaged and aged samples. The mean value of the surface potential decreases after aging. 78

8.1 XRD spectra of unaged and aged samples. Both the samples show presence of $LiFePO_4$ and $FePO_4$ phases 83

8.2 Deconvolution method used for fitting of experimental Raman spectra. The method is demonstrated with the experimental Raman spectra (dots) for C0 battery. The data is deconvoluted in two peaks (dotted line) and then fitted (solid line). The D peak is fitted wth Lorentzian and G peak is fitted with Breit-Wigner-Fano (BWF) line shape. . . . 86

8.3 Raman spectra of all the cells. Each spectra was fitted with the deconvolution method shown in **Figure 8.2**. 87

8.4 Intensity ratio analyses (I_D/I_G). The intensity is calculated as the area under the respective curve. The intensity increases with the C-rate indicating poor quality of carbon leading to loss of electrical conductivity in batteries cycled at higher C-rate. 88

8.5 (a) TEM images of unaged and aged $LiFePO_4$ cathode samples showing the location of EELS spectrum (b) and (c). (b) O K edge of the unaged and aged $LiFePO_4$ cathode samples. There exists a pre-peak in the case of the aged sample suggesting a change in the density of states of O. (c) Fe $L_{2,3}$ edge of the unaged and aged $LiFePO_4$ cathode samples. The edges shift to the right in case of the aged sample. The EELS data was normalized with the O $L_{2,3}$ edge peak. The individual spectra were offset vertically in order to present the details 92

8.6 Crystal structure of $LiFePO_4$ showing one unit cell constructed with Materials Studio™ 94

8.7 (a) The O K edge electron energy loss near edge structure (ELNES) calculated within the Z+1 approximation and dipole selection rules using the Vienna ab-initio simulation package (VASP). (b) Analogous calculation of the Fe $L_{2,3}$ edge ELNES. The energies are set at the Fermi energy, which is 0 eV on the x-axis. The ELNES intensities were normalized to the O K edge peak. The individual spectra were offset vertically in order to present the details. 97

8.8 O p states Fe d states, and P s and p states and their hybridization showing how the states move with Li concentration and thus give rise to variations in the intensity of O K edge pre-peak. The black line is the Fermi level given by Vienna Ab-initio Simulation Package (VASP). 99

8.9 Calculated energy at the Fe $L_{2,3}$ edge peak vs. Li concentration in Li_xFePO_4. The data fits a straight line with slope -1.9 eV. Based on this plot it is estimated that the aged sample was $Li_{0.2}FePO_4$. 100

8.10 NMR spectra of samples harvested from C0 and C6 batteries. An isotropic ^{7}Li peak is observed in C0 while similar speak is absent in C6 106

8.11 A schematic layout of the cold neutron depth profiling chamber at NIST (adapted from [Tun et al., 2010]). At the center of the chamber the sample is mounted using a 21 cm diameter aluminum ring shaped disk concentrically covered with a thick dielectric sheet. The dielectric has a 1 cm dia. hole at the center of the disk which serves as the defining window for charged particles exiting from the sample in the direction of the detector 109

8.12 Effect of C-rate on the lithium concentration in anode and cathode. The profiles were measured in all six sections from C0, C1, C3, and C4; only profiles over section 1, 3 and 5 are shown here. Based on the Li concentration profile in the anode, the lithium tends to build up at the surface of the anode samples aged with higher C-rates, whereas the lithium concentration drops along the thickness of the cathode anode samples. The SOC varies from 0 to 10 % 112

8.13 Effect of state of charge (SOC) and C-rate on the lithium concentration profile in anode and cathode, (a) in section 1, 3 and 5 from C4 and C6, and (b) comparison between section 5 from C0 and C16. The lithium buildup on the anode surface from a cell cycled at higher SOC is less but increases with increasing C-rate. The lithium concentration drops in the cathode with higher SOC and higher C-rate. The SOC varies from 0 to 10 % for C4, 45 to 55 % for C6, and 60 to 70 % for C16 during cycling of the cell. 115

8.14 Lithium concentration profiles measured at different locations on section # 3 in the anode and cathode of C0 and C6 cell. The profiles were measured at three different spots along a straight line on one face (front) and on two spots on the opposite face (back). There is no change in the concentration profiles along the straight vertical line in a section. 117

8.15 (a) Surface lithium concentration of the anode samples taken from cells aged with different C-rate. The surface concentration increases linearly with C-rate. The surface concentration also increases from section 1 to 5 within a cell. (b) Lithium concentration gradient in section # 3 of the anode samples taken from cells aged with different C-rate. The concentration gradient increases with C-rate up to a certain depth of the anode. The depth at which concentration gradient disappears increases with C-rate 118

8.16 Lithium concentration gradient in section # 3 of the cathode samples taken from cells aged with different C-rate. The concentration gradient decreases with C-rate 120

Acronyms

AFM Atomic force microscopy

C-rate Charge-discharge rate of the battery. 1C is the current it takes fully charge or discharge the battery in 1 hour

CSAFM Current sensing atomic force microscope

DFT Density functional theory

DOS Density of states

EC Electrochemical capacitor

EDLC Electric double layer capacitor

EDS Energy dispersive spectroscopy

EELS Electron energy loss spectroscopy

EES Electrical energy storage devices

EIS Electrochemical impedance spectroscopy

ELNES Electron loss near edge structure

EOL End of life

EV Electric vehicle

EWF Electronic work function

GGA Generalized gradient approximation

HEV Hybrid electric vehicle

IR Infrared

KPM Kelvin probe microscopy

MAS Magic angle spinning

NDP Neutron depth profiling

NMR Nuclear magnetic resonance

PAW Projector augmented wave

PHEV Plug-in hybrid vehicle

RS Raman spectroscopy

SEM Scanning electron microscopy

SOC State of charge

SOFC Solid oxide fuel cell

SSRM Scanning spreading resistance microscopy

STEM Scanning transmission electron microscopy

PSD Photo sensitive diode

TEM Transmission electron microscopy

USABC United States Advanced Battery Consortium

USCAR United States Council for Automotive Research

VASP Vienna ab-initio simulation package

XRD X-ray diffraction

Chapter 1: Introduction

The modern economies across the globe depend on availability of affordable and environment friendly energy. Electricity is the most widely used form of energy. In 2007, according to Energy Information Administration, the US generated 4.05 trillion kWh of electricity. Most of the energy supply in the US is based on fossil fuels. This raises environmental concerns such as global warming due to CO_2 emissions. In power plant, the demand for electric power varies based on the season, day of the week, hour, and also due to transients. **Figure 1.1** shows a typical electrical power supply and demand curve over a 24-hour period [Whittingham, 2008]. The power plants are always designed to meet the peak power demand. However, in a 24-hour cycle, there are instances when the demand for the power supply is less than the peak power available. Thus, at times power plants are forced to operate at lower output levels which prove to be uneconomical as the power plants are most efficient at their rated capacity.

Electrical energy storage (EES) devices can help balance this demand in modern power plants by shifting the load from peak to off-peak hours. During the off-peak hours the electrical energy can be stored in an EES device, and then this stored energy would be used during the peak hours. This load-leveling would help in designing power plants with lower rated capacity, thus reducing the cost of installation. The

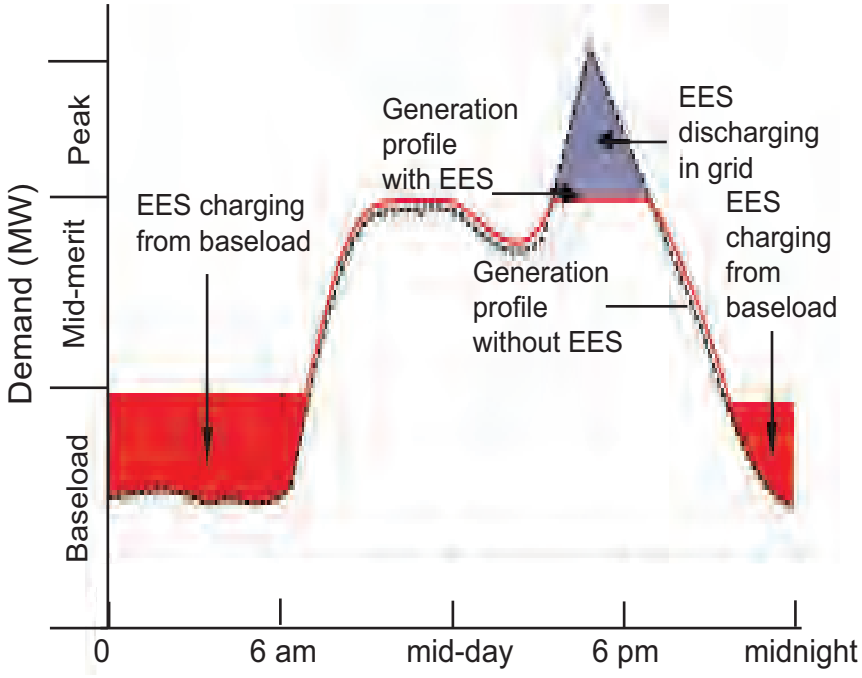

Figure 1.1: A typical electrical power demand profile for a 24 hr period. During early morning hours the demand is below the capacity of the power plant while the demand is at peak in the evening around 6 PM. During off-peak hours an electrochemical energy storage (EES) device would store the energy and during the peak hours the EES will be discharged. Thus EES would level the load and the actual demand cycle will be as shown by the solid line. (adapted from [Whittingham, 2008])

CO_2 emissions level can be lowered due to the lower capacity of the power plant. The operating cost of a power plant can be reduced by operating the plants at the rated capacity for most of the time during its life.

EES can not only help in existing or future fossil fuel based power plants but it can also play a vital role in design and development of power plants based on other unconventional renewable energy sources, such as solar, wind or nuclear energy [Whittingham, 2008]. The energy harvested in such power plants varies largely due to

operating conditions such as weather, wind speed, and temperature. In this case, EES devices can be used to store the energy during the smooth operation of the plant and overcome the intermittent nature of it. Thus, harvesting energy from unconventional sources would be more feasible. These types of power plants can greatly reduce the CO_2 emissions.

The distributed source of CO_2 emissions is major concern than concentrated source in power plants. The internal combustion engines are a major contributor of the distributed source. It also exposes nations dependency on foreign oil. EES devices can play a major role in reducing the emissions due to internal combustions engines and dependency on foreign oil. EV has reduced levels of emissions as well as can alleviate the dependency on foreign oil.

These issues of CO_2 emissions and dependency on foreign oil can be effectively dealt with development of efficient and affordable EES. The typical EES are batteries and electrochemical capacitors. We can also include fuel cell in this list though they are not truly EES but are actively studied for automobile application. Battery technology has already helped revolutionize the electronic gadget industries with application in cell phones, laptops, and tablets. In such applications the life of battery usually exceeds the life of the electronic gadget. So the life of the battery has never been a critical issue in such applications. But in power plants and automobile applications the life of the battery is very critical. For successful development of electric vehicles longevity of battery cycle life is essential. There are on-going efforts to understand the atomic- and molecular level processes that govern the operation of the batteries. Fundamental research is needed to identify the damage mechanisms in batteries in order to improve the cycle life and longevity.

Due to the advances in material science and material synthesis, several different materials have been created for different types of EES devices. Mostly the materials designed for these applications are nanomaterials to improve the energy and power density of the device. But as the demand for such devices has increased and the technology progressed newer materials are introduced. This has limited the testing and characterization of the current materials for identification of damage mechanism to small number of cycles. In all these various applications EES device undergoes several charge and discharge cycles with varying current currents and at varying temperature. This cycling reduces the life of the device. Also these devices come in various shapes and sizes. So geometry may also play role in aging of these devices. Here an overview of various material characterization techniques that can be very useful for understanding the degradation of the materials has been presented.

A brief overview of various EES devices is provided to build the background about such devices. Later the discussion is focused on Li-ion batteries. Various experimental techniques suitable at different length scales are discussed along with some recent results from studies of commercial Li-ion batteries. The review concludes with a brief summary of the damage mechanism identified at various length scales.

Chapter 2: Electrical Energy Storage Devices

The energy storage devices considered for automotive applications are based on some electrochemical process. The energy is stored in form of a chemical energy during charging and the stored energy is released as an electrical energy during discharging. Several different electrochemical energy storage devices are being researched for automotive applications. A brief introduction to operation of electrochemical double layer capacitor and fuel cell has been presented in following sub-section. The operation of the Li-ion batteries is discussed in the later section.

2.1 Electrochemical double layer capacitors

Capacitors are commonly used in power and consumer electronic circuits. However they have very low capacitance in the range of few millifarads which make them unsuitable for large storage devices. In 1957, Becker filed the first patent describing the concept of electrochemical capacitors (EC) which have capacitance in the range of a few hundred farads [Simon and Gogotsi, 2008]. It was then commercialized by Nippon Electric Company (NEC), Japan under a license from Standard Oil of Ohio (SOHIO) [Simon and Gogotsi, 2008]. EC are also called supercapacitors or ultracapacitors. The two different types of EC are the electric double layer capacitor (EDLC) and the pseudocapacitor.

A schematic showing operation of an EDLC is shown in **Fig. 2.1**. EDLC consists of two electrodes with a thin coating of active material having very high surface area. These electrodes are immersed in an electrolyte, mostly sulfuric acid or acetonitrile, containing both positive and negative ions. When the capacitor is connected to the external power source, the electric field attracts the opposite charged ions towards the surface of the electrode. The charge separation occurs near the surface of the electrode, and energy is stored in the EDLC. During discharging, as the electrons flow through the load the ions disperse in the electrolyte solution and the electrode-electrolyte interface fades [Kötz and Carlen, 2000; Miller and Simon, 2008]. A separator is used to prevent the tunneling of the electrons between the electrodes through the electrolyte. The other type of EC capacitor, the pseudocapacitor, has essentially the properties of the EDLC as well as a battery. Thus a charge is stored by the surface as well as sub-surface activities. In EDLC there is no physical or chemical change in the electrode, and the ion adsorption process is highly reversible. Thus, theoretically EDLC can be charged/discharged without any damage to its components [Miller and Burke, 2008].

The charge separation at the electrode-electrolyte interface is given by Helmholtzs double layer capacitance C:

$$C = \frac{\epsilon_r \epsilon_o A}{d} \tag{2.1}$$

where $\epsilon_r$is the electrolyte dielectric constant, $\epsilon_o$is the dielectric constant of the vacuum, d is the effective thickness of the double layer (charge separation distance), and A is the electrode surface area.

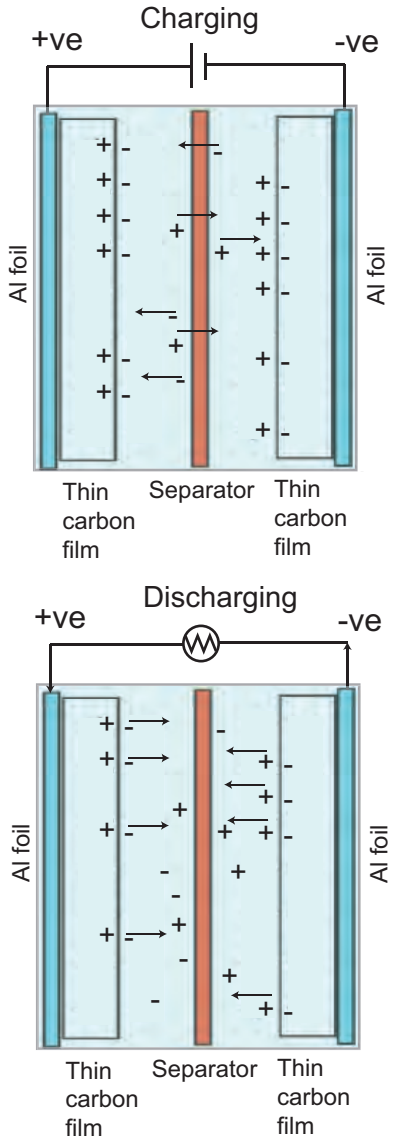

Figure 2.1: Schematic showing operation of an electrochemical capacitor (EC). During charging the ions in the electrolyte are attracted to the nanoporous electrodes with opposite charge. This creates the charge separation at the electrode-electrolyte interface and the energy is stored in EC. During discharging, as the electrons flow through the load the ions disperse in the electrolyte solution and the electrode-electrolyte interface fades

2.2 Fuel cell

A fuel cell converts the energy stored in the source fuel to usable electrical energy. It is different from other EES in that the reactants flow through the cell rather than being sealed within the cell. There are several types of fuel cells, but the most common are the solid oxide fuel cell (SOFC) and the proton exchange membrane fuel cell (PEMFC) [Carrette et al., 2000]. A schematic of SOFC is shown in **Fig. 2.2a** and schematic of PEMFC is shown in **Fig. 2.2b**. SOFC is the most fuel flexible among all fuel cells. Other than pure hydrogen, it can run on hydrocarbon, methanol or even gasoline, but in the case of PEMFC pure hydrogen is the only choice of fuel. Essentially both fuel cells have similar principles of operation except that in SOFC, O^{2-} ions are conducted through the solid oxide membrane (SOM) while in PEMFC H+ ions are conducted through the proton exchange membrane (PEM) [Haile, 2003; and Jacobson, 2010].

In SOFC, the oxygen is oxidized to O^{2-} as per the following half-cell reaction at the cathode:

$$\tfrac{1}{2}\,O_2 + 2\,e^- \longrightarrow O^{2-} \tag{2.2}$$

These O^{2-} ions are conducted through the solid oxide membrane to the anode where they are reduced by hydrogen with water as a by-product. The anode half-cell reaction is:

$$H_2 + O^{2-} \longrightarrow H_2O + 2\,e^- \tag{2.3}$$

In the case of PEMFC, hydrogen is reduced at the anode, and the H^+ ions are formed as per the following half-cell reaction:

$$H_2 \longrightarrow 2\,H + 2\,e^- \tag{2.4}$$

These H^+ ions are conducted through the proton exchange membrane, and they are combined with oxygen at the cathode to form water as the byproduct of the reactions. The half-cell reaction at the cathode is:

$$\tfrac{1}{2}\,O_2 + 2\,H^+ + 2\,e^- \longrightarrow H_2O \tag{2.5}$$

Due to the high operating temperatures, in the range of the 500 and 1000 °C, SOFC is more cost effective as it does not need an expensive catalyst such as Pt, used in PEMFC, but the disadvantage of high operating temperatures is that the components of SOFC should demonstrate higher thermal and thermo-mechanical stability. In the case of the PEMFC the operating temperature is lower (70-100 °C), but the proton exchange membrane needs to be hydrated to optimum levels to maintain the proton conductivity [Haile, 2003]. Too much wetting of the membrane causes flooding of the cell. If the membrane is dry then it can also lead to cracking of the membrane and overheating of the cell [Haile, 2003].

A good electrolyte membrane for a fuel cell should have high ionic conductivity, low electronic conductivity, should be stable in both oxidizing and reducing environments, good mechanical properties, and good thermal stability. The electrodes should have high electronic conductivity and high (electro) catalytic activity. The anode catalyzes the oxidation of the fuel components by the ions transported

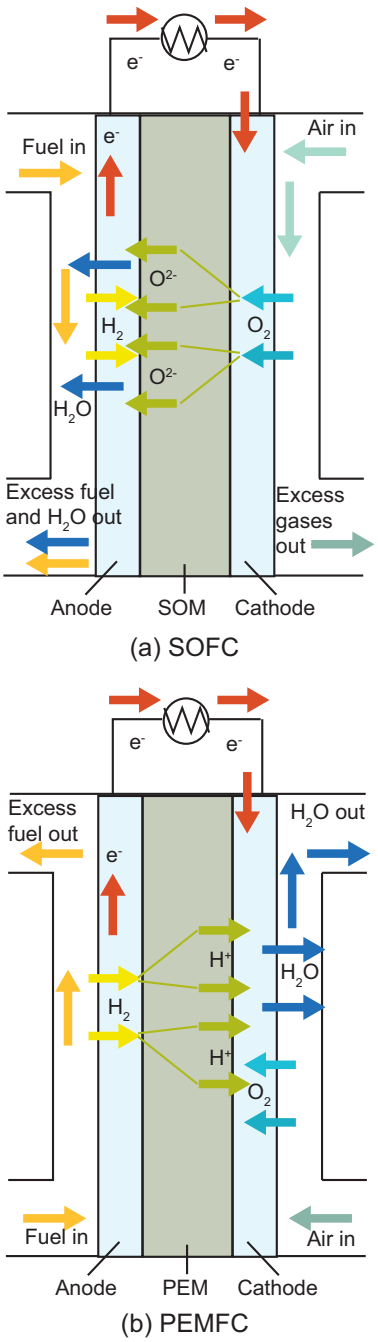

Figure 2.2: (a) Schematic showing operation of a solid oxide fuel cell (SOFC). Oxygen is reduced at cathode and the resulting O^{2-} ions are conducted through the solid oxide electrolyte membrane (SOM) to the anode where they are oxidized with the hydrogen to form water. (b) Schematic showing operation of a proton exchange membrane fuel cell (PEMFC). Hydrogen is oxidized at anode and the resulting H^{+} ions are conducted through the proton exchange membrane (PEM) to cathode where they are reduced with O to form water

through the electrolyte membrane and the cathode catalyzes the reduction of oxygen [Jacobson, 2010].

2.3 Batteries

A battery is a device that stores electrical energy in chemical form, and by the principle of a galvanic cell, it converts this chemical energy into electricity when connected to an external load. A galvanic cell is a device consisting of an anode and a cathode dipped in an electrolyte, and it produces electricity by spontaneous reduction-oxidation (redox) reaction. Batteries are classified according to their chemistries. Depending on the chemistry of the battery, different materials are used to make its components. **Table 2.1** summarizes the properties of various battery chemistries, while **Table 2.2** lists the advantages and limitations of these batteries. These different battery chemistries and their advantages and limitations are briefly discussed here.

2.3.1 Lead-acid

French physician Gaston Plant introduced the lead acid battery in 1859. It was the first commercially available rechargeable battery. Though many battery chemistries were introduced later on, lead acid is still used in a lot of applications due its cost effectiveness and ruggedness. Because of gassing and water depletion, this battery can never be charged to its full capacity. Also, each time the battery is discharged completely, it tends to lose a small amount of its capacity. Because of the lead content, this battery is treated as non-friendly to the environment. They are used in wheelchairs, hospital equipment, automobiles for auxiliary equipments, and uninterruptible power supply systems.

2.3.2 Nickel-Cadmium

The nickel-cadmium battery was invented in 1899 by a Swedish man, Waldmar Jungner. In 1947, Neumann was successful in introducing the completely sealed version of this battery. This battery has a moderate energy density and a long cycle life. The main drawback in this battery is the memory effect, in which the battery gradually loses its maximum energy capacity if it is repeatedly recharged after being only partially discharged. Though the metals used are toxic, it remains a favorite choice in areas where the most rigorous charge-discharge cycles are expected. Because of its ability to draw heavy load currents, it is also a favorite choice in applications like power tools.

2.3.3 Nickel-Metal Hydride

Development of the nickel-metal hydride battery started in 1970. Only after stable metal hydride alloys were developed in 1980, was this battery available for consumers. The cathode in the Ni-MH battery is composed of nickel hydroxide. The anode is mostly composed of an intermetallic compound of type AB5 where A is a rare earth mixture of lanthanum, cerium, and titanium, and B is nickel, cobalt, manganese and/or aluminum. The materials used in this battery are non-toxic. Though it is better in some aspects than the nickel-cadmium battery, it shares some of its drawbacks with the nickel-cadmium battery due to the nickel technology. The cycle life of this battery is less than that of nickel-cadmium. It has a higher energy density compared to nickel-cadmium and shows no memory effect. Before the lithium-ion battery was

introduced, the nickel-metal-hydride battery was used in mobile computing and wireless communications. It is often believed among researchers that nickel-metal-hydride led to the development of the lithium-based battery.

2.3.4 Lithium-ion

The research for lithium-ion battery technology started with lithium batteries. In 1912, G. N. Lewis began working on lithium batteries. Lithium (atomic number 3, group 1, period 2) was used as an anode in lithium batteries. Lithium is an alkali metal, and being the lightest of the metals with greatest electrochemical potential, has the largest energy density for weight. But, lithium is very unstable, as it has only one valence electron. This made lithium batteries very unsafe for commercial use and so, research shifted from a lithium battery to a lithium-ion battery, which is a much safer option. As lithium-ion batteries are the main topic of this article, they have been discussed in detail in chapter 3.

Table 2.1: Characteristics of commonly used rechargeable batteries [Buchmann, 2001]

	Lead-acid (sealed)	Ni-Cd	Ni-MH	Li-ion cobalt oxide	Li-ion manganese	Li-ion phosphate
Commercial use since	1970	1950	1990	1991	1996	2000
Gravimetric energy density (Wh/kg)	30-50	45-80	60-120	150-190	100-135	90-120
Internal resistance ($m\Omega$)	100 12V pack	100 to 200 6V pack	200-300 6V pack	150-300 pack 100 - 130 per cell	25-75 100 - 130 per cell	25-50 100 - 130 per cell
Cycle life (to 80% of initial capacity)	200-300	1500	300-500	300-500	Better than 300 to 500	> 1000
Fast charge time (h)	8 to16	1	2 to 4	1.5 to 3	1 or less	
Overcharge tolerance	High	Moderate	Low	Low. Cannot tolerate trickle charge		
Self-discharge per month (room temperature)	5%	20%	30%	$< 10\%$		
continued...						

Table 2.1 continued ...

		Lead-acid (sealed)	Ni-Cd	Ni-MH	Li-ion cobalt oxide	Li-ion manganese	Li-ion phosphate
Cell voltage (V)		2	1.25	1.25	Nominal 3.6 Average 3.7	Nominal 3.6 Average 3.8	3.3
Load current	Peak	5	20	5	< 3	> 30	> 30
	Best	0.2	1	0.5 or lower	1 or lower	10 or lower	10 or lower
Operating temperature (C)		-20 to 60	-40 to 60	-20 to 60	-20 to 60		
Maintenance requirement		3 to 6 months	30 to 60 days	60 to 90 days	Not required		
Safety		Thermally stable	Thermally stable Fuse recommended	Thermally stable Fuse recommended	Protection circuit mandatory Stable to 150 (C)	Protection circuit mandatory Stable to 150 (C)	Protection circuit mandatory Stable to 150 (C)
Toxicity		Toxic lead and acids harmful to environment	"Highly toxic Harmful to environment	Relatively low toxicity, should be recycled	Low toxicity, can be disposed in small quantities		

Table 2.2: Advantages and limitations of commonly used rechargeable batteries (Adapted from [Buchmann, 2001])

Chemisty	Advantages	Limitations
Lead-acid (sealed)	Very inexpensive and simple to manufacture Well-developed technology Lowest self-discharge Low maintenance- no memory effect, no electrolyte to fill on sealed version Capable of high discharge rates	Low energy density limits use to stationary and wheeled applications Voltage should never drop below 2.1V Allows only limited number of full discharge cycles Environmentally unfriendly due to the lead content Thermal runaway can occur due to improper charging Some versions can never be charged to their full potential
Nickel-cadmium	Fast and simple charge High cycle life Good load performance Long shelf life Easy storage and transportation Good low temperature performance One of the most rugged rechargeable batteries Lowest in terms of cost per cycle Available in a wide range of sizes and performance options	Relatively low energy density Shows memory effect Environmentally unfriendly and so some countries restrict its use Relatively high self-discharge- needs recharging after storage
Nickel-metal -hydride	30-40% higher capacity than standard nickel-cadmium Less prone to memory effect than nickel-cadmium Simple transportation Environmentally friendly - contains only mild toxins; profitable for recycling	Limited service life of 200-300 cycles Relatively short storage life Limited discharge current More complex charge algorithm due to heat generated during charging
continued...		

Table 2.2 continued ...		
Chemisty	Advantages	Limitations
		Trickle charge settings are critical because the battery cannot absorb overcharge High self-discharge Should be stored in cool place at 40C High maintenance
Lithium-ion	Highest gravimetric energy density (Wh/kg) Does not need prolonged priming Relatively low self-discharge Low Maintenance - no memory effect Cells with high current capacity can be manufactured for power tool applications	Requires protection circuit to maintain voltage and current within safe limits Aging is a major issue Expensive to manufacture

2.4 Comparison of different electrochemical energy storage devices Ragone plot

A Ragone plot, shown in **Fig. 2.3**, is used to compare the energy density and power density of various electrochemical energy storage (EES) devices [Whittingham, 2008, 2011]. Energy is defined as the capacity to do work, so energy density represents the capacity of the EES, i.e., amount of energy stored in the device. Power is defined as the rate of doing work, so power density represents the rate at which the EES is charged or discharged.

As seen in the Ragone plot (**Fig. 2.3**), a fuel cell has the highest energy density but poor power density, so fuel cells are suitable for applications where high energy

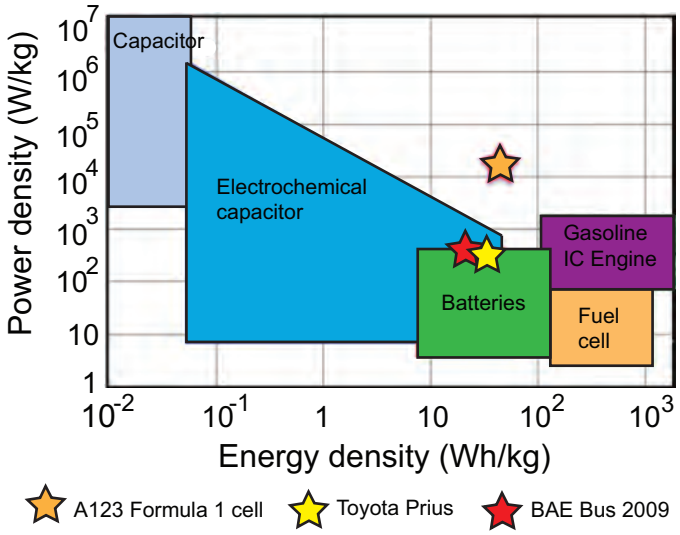

Figure 2.3: Ragone chart showing the comparison of the power density and energy density for batteries, capacitors, and fuel cells and internal combustion engine. Energy density represents the capacity while power density represents the rate of the charging/discharging of EES device. [adapted from [Whittingham, 2011]

storage is necessary. They also tend to operate at optimum efficiency only at a constant output. They have a certain warm-up time necessary to bring them to operating conditions, and as such they are often coupled with other EES. As opposed to fuel cells, an electrochemical capacitor has high power density but low energy density, so they are suitable for applications where rapid charge/discharge in necessary. However the output of the electrochemical capacitor depends largely on its state of charge, and thus it fails to deliver energy at constant voltage [Whittingham, 2008, 2011]. Batteries lie in between the fuel cell and the electrochemical capacitor on the Ragone plot. They have higher power density than fuel cells and do not require any warm-up time. They also have higher energy density than an electrochemical capacitor and have a

flat voltage curve during discharge. Thus, batteries have been actively pursued as the EES for immediate future applications.

Chapter 3: Li-ion Batteries

Sony commercialized the lithium-ion battery in 1991, and since then it has been growing and gaining popularity at a rapid pace. The lithium-ion battery was initially used in mobile phones and laptop computers. This battery shows no memory effect and requires minimal maintenance. Its energy density is the highest among the other chemistries. Recently, due to its improved load characteristics and ability to draw high currents, it has also been used in power tools and medical devices. A protection circuit is often found in lithium-ion battery systems to limit charge and discharge, voltages and currents for safety reasons. Also, to avoid any thermal runaway and consequential fire hazard, the temperatures are continuously monitored in a lithium-ion battery system. In spite of requiring a protection circuit and a risk of thermal runaway, lithium-ion batteries have emerged as the single most favorite for portable applications, due to the other advantages it has over the alternate battery chemistries. The different types of lithium-ion batteries are discussed in **Table 2.1**.

3.1 Electrochemistry of Li-ion batteries

The anode in a lithium-ion battery is mostly made up of graphitic carbon , while different materials such as $LiCoO_2$, $LiMnO_2$, and $LiFePO_4$ are being tried for the cathode. The electrolyte in a lithium-ion battery is a lithium salt, such as

$LiPF_6$, $LiBF_4$, and $LiClO_4$, soluble in an organic solvent, such as dimethyl carbonate (DMC) and/or ethylene carbonate (EC). The chemical reaction in the case of the lithium-ion battery is based on intercalation. In an intercalation reaction, guest ions are introduced in the host structure. The intercalation reaction is a reversible reaction and barely modifies the host structure. The host structure can be either two-dimensional or even three-dimensional.

Figure 3.1 shows a schematic of an intercalation reaction between a carbon anode and a $LiFePO_4$ cathode. As seen in the schematic, intercalation reaction occurs during charging, and Li^+ ions are transferred from the cathode into the anode. During discharging, a deintercalation reaction occurs, and Li^+ ions are transferred from the anode to the cathode while the electrons flow through the external circuit. The following chemical reaction occurs in a lithium-ion battery with a carbon anode and a $LiFePO_4$ cathode:

$$Li_{(1-x)}FePO_4 + Li_xC_6 \longleftrightarrow Li_{(1-x)}C_6 + Li_xFePO_4 \tag{3.1}$$

The Li^+ ions are never oxidized in this chemical reaction but are only intercalated and deintercalated to and from the anode or cathode. The Fe in $LiFePO_4$ undergoes oxidation from Fe_2^+ to Fe_3^+ during charging, and reduction from Fe_3^+ to Fe_2^+ during discharge. This is slightly different than the reaction in conventional batteries, where the anode undergoes oxidation and the cathode undergoes the reduction reaction.

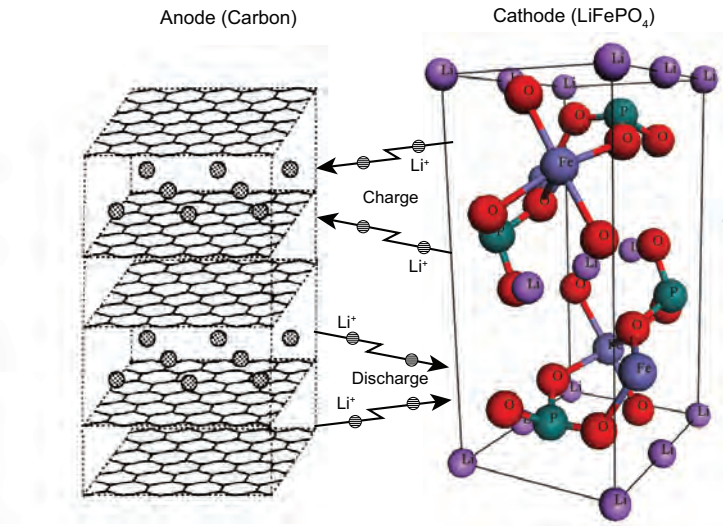

Figure 3.1: Schematic of intercalation-deintercalation process. During charging Li^+ ions are inserted in the anode structure by virtue of intercalation and during discharging, these Li^+ ions are removed from the anode structure by virtue of deintercalation and transferred to the cathode [Anonymous, 2007; Nagpure et al., 2011c]

3.2 Requirements of automobile industry

Lithium-ion batteries were introduced for devices like mobile phones and laptop computers. These devices undergo rapid development cycles, and newer versions arrive in a short period of time. As such, the age of the lithium-ion battery exceeded the age of these devices. Recently, lithium-ion batteries have been trying to acquire a market share in more durable goods, like the automobile industry. Lithium-ion batteries have found applications in electric vehicles (EV), hybrid electric vehicles (HEV), and temporary storage systems for renewable energy sources. EV or HEV not only reduce the burden on gasoline consumption and in turn on the non-renewable energy sources, but can also help protect the environment by lowering emissions. The US Advanced Battery Consortium (USABC, www.usabc.org) was established by the

US Council for Automotive Research (USCAR). One of the objectives of USABC is to continue the development of battery technology for EV and HEV. Any electric vehicle has a high voltage battery pack consisting of individual cells. The life of the individual cells depends on the cycling conditions such as operating temperature, state of charge, C-rate etc... The details about the battery pack, cell specification and conditions have been described in **Appendix A**. According to USABC, a 42-V battery in a HEV should have a calendar life of 15 years [Anonymous, 2002]. Electric vehicles should have a battery system that can last for 10 years [Anonymous, 2006a]. In terms of cycles, 1000 cycles at 80 % depth-of discharge are expected in EV and 300,000 cycles at 50Wh are expected in a plug-in HEV [Anonymous, 2006b]. This makes a prolonged life for a lithium-ion battery an absolute necessity, if it is to succeed in the automobile industry. End of life for the batteries used in automobiles is considered to be reached when the battery delivers only 80 % of its rated ampere-hour capacity.

Chapter 4: Materials for Li-ion Batteries

Lithium ion batteries are complex electrochemical system. The performance of these batteries is highly dependent on the thermal, mechanical and physical stability of its materials. The main components of the lithium ion battery are the anode, cathode, separator and the electrolyte.The electrodes are a composite structure comprising of active material, binders, and additives. The separator is made up of a polymer that prevents the contact between the anode and cathode but allows the lithium ions to pass through it. The electrolyte provides the path for the lithium ions to travel between the electrodes during the cycling of the cell. Due to the potential application of these batteries in the transportation industry, there have been great deals of efforts to develop cheaper, reliable and stable materials. In doing so often extraordinary claims are made about the long term electrochemical performance of the system and the intrinsic limitations are overlooked. In following sections certain active materials for anode and cathode and electrolytes have been discussed. These materials have been tested by several researchers and they have shown certain potential in furthering the lithium ion battery technology. The details of these sections have been adapted from in parts from Mantia [2008].

4.1 Anode

Lithium is an ideal anode material for Li-ion batteries, but because of the plating out of lithium during the charge/discharge cycle and subsequent formation of dendrites, there is a risk of the cell being short-circuited. Instead, carbonaceous materials are preferred for anodes in most commercially available Li-ion batteries [Kong et al., 2001]. Studies have been conducted on graphite [Bruce et al., 2008], C-C composite, mesocarbon microbeads (MCMB) [Hossain et al., 2003], carbon nanotubes [Whittingham, 1976; Fan et al., 2007] and carbon films. These anodes have a very good rate of lithium insertion/removal and thus improve the charge/discharge rate (power rating) of the battery, but in any Li-ion cell with a carbonaceous anode a solid electrolyte interphase (SEI) is formed during cycling of the cell [Peled, 1979; Kanno et al., 1992; Kong et al., 2001]. The SEI is formed from the electrolyte decomposition products [Vetter et al., 2005]. This SEI layer prevents the graphite surface from further exfoliation and also prevents further reduction of the electrolyte and consumption of active lithium. In the case of nanoparticulate graphite, the consumption of active lithium would be still higher, and the excessive charge developed between the graphite surface and the SEI would result in a loss of overall cell voltage. Also, it is important to note that the lithium is intercalated into graphite at potentials less than 100 mV versus Li/Li^+. There is always a risk of lithium depositing on the graphite surface resulting in dendrite formation and fatal short circuiting of the cell [Bruce et al., 2008]. Carbon nanotubes exhibit twice the lithium storage compared with graphite but have similar problems of surface-layer formation and safety [Bruce et al., 2008]. To overcome some disadvantages of graphite, the research has been focused on the titanium oxide. The nanoparticles of non-toxic $Li_4Ti_5O_{12}$ ($Li[Li_{1/3}Ti_{5/3}]O_4$) with

spinel structure have high diffusion rates due to short diffusion distance. In this spinel structured oxide, lithium can be intercalated to give a composition range of $Li_{4+x}Ti_5O_{12}$, 0<x<3 [Ferg et al., 1994; Jansen et al., 1999], but the capacity of the $Li_4Ti_5O_{12}$ is only 150 mAh/g compared to 300 mAh/g capacity of graphite. Instead nanotubes/nanowires composed of TiO_2-(B), are been actively studied [Bruce et al., 2008]. This fifth polymorph of titanium dioxide has all the advantages of $Li_4Ti_5O_{12}$ but also has a capacity of 300 mhA/g. TiO_2-(B) is also safer as it eliminates the risk of lithium plating on the electrode and can be cycled with higher rates as in $Li_4Ti_5O_{12}$. The TiO_2-(B) nanowires exhibit better performance than TiO_2-(B) nanoparticles as they have higher reversibility of intercalation (¿99.9 % per cycle, after the first cycle). Other similar oxide nanowire electrode materials of interest include Sn, Co, and V oxides [Bruce et al., 2008]. Lithium metal alloys such as $Li_{4.4}Sn$ (993 mAh/g) and $Li_{4.4}Si$ (4200 mAh/g) with high specific capacity are also being considered as anode materials in Li-ion batteries. The major drawback of these materials is the large volume change during the cycling of the cell to accommodate the large amounts of lithium [Bruce et al., 2008]. The following table lists the properties of the certain anode materials.

Table 4.1: Properties of certain anode materials suitable for lithium-ion batteries. [Adapted from [Mantia, 2008]]

Reduced form	Oxidized form	Eeq (Li/Li^+) (V)[a]	Qmax / (mAh g-1)[b]
Metals			
Li	Li^{+c}	0	3861
Graphite based compounds			
LiC_6	Graphite	0.1	372
$Li_{1/2}C_6$	Graphite	0.13	186
$Li_{1/3}C_6$	Graphite	0.22	124
Alloys			
LiAl	Al	0.35	993
$Li_{22}Sn_5$	Sn	0.42 - 0.66	994
Li_3Sb	Sb	0.9	660
$Li_{21}Si_5$	Si	0.3	4000
Titanates			
Li_xTiO_2	TiO_2	1.8	170
$Li_{4+x}Ti_5O_{12}$	$Li_4Ti_5O_{12}$	1.5	160

[a] The electrochemical activity can be observed in a range of potentials.
[b] The specific charge is relative to the weight of the pristine active material.
[c] Li^+ is in solution [Ohzuku et al., 1995; Winter et al., 1998]

4.2 Cathode

The potential area of greatest opportunity for nanomaterials is the cathode of the Li-ion battery [Whittingham, 2008]. The most common cathode materials are layered oxides $LiMO_2$, the spinels $Li[M_2]O_4$ and olivines $LiMPO_4$ where M is a transition metal atom [Goodenough, 2007]. The nanoparticulates of these materials reduce the diffusion length, provide a higher electrolyte/electrode contact area, and thus improve the charge/discharge kinetics of the Li-ion batteries. The nanoparticles of these lithium compounds are made by grinding, synthesis from solution, or by solgel approaches [Bruce et al., 2008].

LiCoO2, was developed as the cathode material for commercial Li-ion batteries [Goodenough, 2007; Bruce et al., 2008], but due to expensive and toxic cobalt they were later replaced by oxides such as $LiNi_{0.8}Co_{0.15}Al_{0.05}O_2$, $LiNi_{0.8}Co_{0.2}O_2$, $Li_{1-x}Ni_{1-y}Co_yO_2$, and $LiMn_{0.5}Ni_{0.5}O_2$ in commercial batteries [Kostecki and McLarnon, 2002, 2004; Goodenough, 2007]. These oxides have a high operating voltage, in the range of 2.75 V to 4.3 V [Goodenough, 2007]. They have very high energy density and power density but they lack the necessary structural stability for deep discharge cycles, during which the host oxide structure collapses upon removal of more than 50 % of the Li. Li spinel compounds, such as $LiMn_2O_4$ has good structural stability [Bruce et al., 2008]. They also have higher operating voltage and high charge/discharge rate but low energy density. The most recent among these lithium compounds has been the olivine structured $LiFePO_4$. It has a lower operating voltage of ~3.3 V but demonstrates higher power and energy density along with a good structural stability. The following table lists the properties of the certain cathode materials.

Table 4.2: Properties of certain cathode materials suitable for lithium-ion batteries. [Adapted from [Mantia, 2008]]

Reduced form	Oxidized form	Eeq (Li/Li^+) (V)[a]	Qmax (mAh g-1)[b]
Layered compounds			
$LiTiS_2$	TiS_2	1.5 - 2.4	239
$Li_3V_2O_5$	V_2O_5	2 - 3.5	442
$LiCoO_2$	$LixCoO_2$	3.5 - 4.2	274
$LiNiO_2$	$LixNiO_2$	3.5 - 4.2	274
$LiMnO_2$	$LixMnO_2$	3.5 - 4.2	285
$Li(NiMnCo)O_2$	$Lix(NiMnCo)O_2$	3 - 4.5[c]	274[c]
Olivines			
$LiMnO_4$	$LixMnO_4$	3 - 4	213
Spinel			
$LiFePO_4$	$FePO_4$	3.4	170

[a] The electrochemical activity can be observed in a range of potentials
[b] The specific charge is relative to the weight of the pristine active material and all lithium m ions removed
[c] The mixed oxides can show very different behavior depending on the exact composition ([Whittingham, 2004]).

4.3 Electrolytes

The function of the electrolyte is to provide a path for the ions while blocking any electronic charge flow. The electrolyte should be thermally stable in the operating range of the battery. It should be safe and environmentally compatible. The cycle life of the battery depends on the exact composition of the electrolyte [Peled, 1979]. The electrolyte should be electrochemically inert with the oxidizing or reducing electrode surfaces. Often a passivation film composed from reduction products of the electrolyte is formed on the electrode surface. This film affects the cycle life of the battery. The stability, and quality of the film depends on the electrolyte composition, additives and impurities. Usually electrolyte is composed of one or more liquid solvents and

one or more salts. The electrolytes used in lithium ion batteries are non-aqueous and aprotic.

The specific ionic conductivity of the electrolyte depends on the mobility of the ions and the number of the ions in the solvent. The Stokes-Einstein equation gives a relationship between the mobility of the ion and the viscosity of the solvent [Xu, 2004]:

$$\mu_i = \frac{1}{6\pi\eta r_i} \tag{4.1}$$

where μ_i is the ionic mobility, η is the viscosity of the solvent, and r_i is the ionic radius (inclusive of the solvation shell). Electrolytes with lower viscosity would have higher mobility for the ions. The lithium ions engage in the reaction at both the electrode surfaces. The transport number of the lithium ions is given by:

$$t_{Li^+} = \frac{\mu_{Li^+}}{\mu_{Li^+} + \mu_{A^+}} \tag{4.2}$$

where t_{Li^+} is the transport number, and A^+ is the corresponding anion of the lithium salt. The transport number of Li^+ in the electrolytes used for lithium-ion batteries is between 0.2 and 0.4 [Ue and Mori, 1995; Blint, 1995].

The preferred electrolyte for the lithium-ion batteries is combination of ethylene carbonate (EC) and dimethyl carbonate (DMC) with $LiPF_6$. EC is solid at room temperature. and has low viscosity [Xu, 2004]. The EC:DMC mixture is liquid for range of compositions. $LiPF_6$ exhibits good conductivity. A 1M LiPF6 solution of EC:DMC 1:1 (wt.) has a conductivity of 10^7 mS cm^{-1} , and it is stable and safe in the temperature range between -20 and 50 degC .The conductivity is quite high for a

nonaqueous electrolyte, but is still too low to avoid non-homogeneous usage of thick electrodes when high power is required.

Table 4.3: Properties of certain solvent and solutes for lithium-ion battery electrolytes. [Adapted from [Mantia, 2008]]

Solvents				
Solvent	Tm (C)	Tb (C)	h (cP[a])	e[a]
Cyclic carbonates				
EC	36.4	248	1.9[b]	89.8
PC	-48.8	242	2.5	64.9
Linear carbonates				
DMC	4.6	91	0.59	3.1
DEC	-74.3	126	0.75	2.8
EMC	-53	110	0.65	2.9
Salts				
Salt	T (C)	s (mS cm^{-1})		
		PC		EC:DMC
$LiBF_4$	> 100	3.4		4.9
$LiPF_6$	~80	5.8		10.7
$LiAsF_6$	> 100	5.7		11.1
$LiClO_4$	> 100	5.6		8.4

[a] Measured at 25 C.
[b] Measured at 40 C [Xu, 2004]]

The other choices of lithium salts are $LiBF_4$, $LiAsF_6$ and $LiClO_4$. Though these salts might be stable at higher temperature they have certain drawbacks as compared to $LiPF_6$. $LiBF_4$ has low conductivity [Ue and Mori, 1995]. $LiAsF_6$ prevents formation of dendrites but is undesirable due to toxicity of As [Koch et al., 1982]. $LiClO_4$ has advantage over $LiPF_6$ as it can form the SEI which has higher conductivity. But ClO_4 is not stable at high currents. Certain polymer and ionic liquids are being tested for future generations of lithium ion batteries [Xu, 2004]. Solid polymer electrolytes have

very poor conductivity (< 1 mS cm^{-1}) [Song et al., 1999]. Ionic liquids also need to be tested before they can be used in lithium ion batteries [Xu, 2004].

Chapter 5: Aging Cycles for Li-ion Batteries

Aging or cycling of the batteries for aging studies is very critical for material characterization. The aging cycles should be representative of an actual charge/discharge cycle a battery would experience on the vehicle. The operating temperature, SOC, DOD and the C-rate are generally considered to be the main factors affecting the aging of the batteries. As such these factors need to be included in the aging cycles. Thus designing the aging cycles based on actual cycle is a daunting task.

Typical driving cycles have been developed to represent the driving conditions experienced in the real world usage of the vehicle. These driving cycles are developed to quantity the fuel consumption and green house gas emissions for different driving conditions. The typical driving cycles developed for US are FTP-72 or Federal urban driving cycle (FUDS), FTP-75, US06. SC03, NYCC and HWFET. Among these driving cycles the FUDS and US06 driving cycles are used to simulate driving in different routes. FUDS represents driving on a urban route while US06 represents a more aggressive highway driving. Using these various cycles the fuel consumption and the green house gas emissions can be measured for various types of trips. These driving cycles represent certain energy demand at the wheel. Thus it gives energy demanded from the primary source on the vehicle.

There are several different types of electric vehicles based on the primary and the secondary source on the power. In a purely electric vehicle the primary and the only source is battery. The battery operates in the charge-depleting mode and can only be charged by plugging into an external power source. The hybrid vehicles have two or more sources of power that are directly or indirectly coupled with the drive train. The primary source in hybrid vehicles is usually internal combustion engine and the secondary source is the battery. In HEV the primary source is the IC engine and the secondary battery source is used intermittently. In HEV the battery is used in the charge-depleting and then charge-sustaining mode and the control strategy determines the range of operation of the battery. The PHEV combines the advantages of the EV and HEV. The battery can be used over larger range and it can be charged directly by plugging into the external power source. The ability to charge the batteries through external power source adds to the complexity of reproducing the aging cycle of the battery as the external charging would depend on several factors such as users choice to charging time, duration and location.

A synthetic driving cycle for HEV application was developed by Spagnol et al. [2010]. The temperature and the SOC were obtained from the operating condition and the initial charge. The DOD and the C-rates were extracted from the real data. **Figure 5.1a** shows the real driving data in HEV application that was used in this study. The real current profile (I) in the actual cycle is normalized with the nominal capacity of the pack (S_c):

$$C_{rate} = \frac{I}{S_c} \tag{5.1}$$

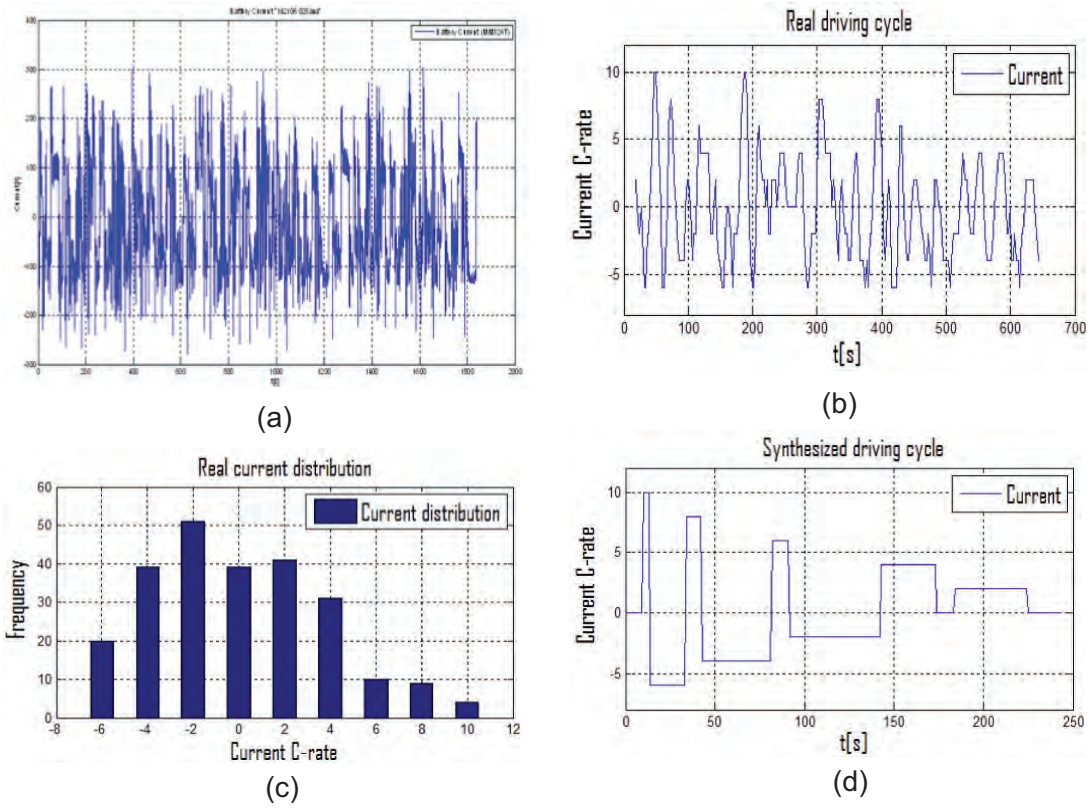

Figure 5.1: Synthesis of aging cycle from real life driving cycle

This normalized current profile is shown in **Fig. 5.1b**. This current profile is then discretized into 2-C length bins and the histogram is generated as shown in **Fig. 5.1c**. The number of bins is chosen to be as small as possible but also to capture the main aging effects. Then using the heuristic design based on statistical distribution approach a synthetic aging cycle as shown in **Fig. 5.1d**, which is easy to implement in the laboratory, is generated.

As stated earlier the batteries in EV are operated in charge depleting mode while batteries in the HEV and PHEV are operated in charge sustaining mode. Using this control and the synthetic aging cycle design [Marano et al., 2009] were able to

generalize the operating range for the batteries in various EVs. As battery is the only source of energy in EV they operate at much lower C-rate and higher range of SOC. While in HEV the SOC range is smaller but the C-rate is high. PHEV operate within these two extremes with moderate SOC and C-rate. Thus aging cycles in these types of studies are carefully designed based on the vehicle applications. Also as temperature affects the operation of the batteries, it can be included as one of parameters in the aging cycle.

As mentioned earlier multi-scale characterization is performed on commercial cells. The cells were cycled as lower SOC and lower C-rate. Commercial lithium ion cells used in these experiments have a graphite anode and a cathode comprising of LiFePO4 nanoparticles (40 nm - 50 nm). Graphite is bonded onto a copper substrate, and layers of LiFePO4 nanoparticles are bonded onto an aluminum substrate using a polyvinylidene difluoride (PVDF) binder. The anode and cathode strips, with a separator in between, are rolled and then packed into a can to form a cylindrical cell. The electrolyte used in this cell is a lithium hexafluorophosphate ($LiPF_6$) salt in 1:1 ethylene carbonate and dimethyl carbonate. The cell has an operating voltage of 3.3V and a nominal discharge capacity of 2.3Ah. $LiFePO_4$ has poor electronic conductivity ($\sigma = 2\times10^9$ S cm^{-1}) [Franger et al., 2005]. To improve the conductivity, the nanoparticles are coated with carbon (Benoit and Franger, 2008). **Table 5.1** describes the condition of the cells used in this study. The effect of charging or discharging current rate (C-rate) was studied with cells # C1, C3, and C4 cycled from 0% to 10% state of charge (SOC) with a C-rate of 1C, 3C and 4C, respectively (1C-rate = 2.3Ah). Two cells were cycled with higher C-rates and at higher SOC to study the effect of the SOC on the lithium concentration profiles. Cell C6 was cycled

from 60% to 70% SOC with 6C rate. Cell C16 was cycled with the highest C-rate of 16C from 45% to 55% SOC. All the cells were cycled at 45C. A cell that underwent only one complete charge-discharge cycle was established as the baseline cell in these studies (C0). The cycling of the cells was terminated when the cells reached ∼80% of their rated capacity. This protocol was found to be consistent with the automotive industry standard, which considers a cell to be dead when its capacity drops below 80% of the original rating [Anonymous, 2006b].

Table 5.1: Aging cycles

Sample	Aging condition	Residual capacity
C0	New- No aging	100%
C1	1C, 0-10% SOC, 45°C	∼80%
C3	3C, 0-10% SOC, 45°C	∼80%
C4	4C, 0-10% SOC, 45°C	∼80%
C6	∼6C, 60-70%, SOC 45°C	∼80%
C16	16C , 45-55%, SOC 45°C	∼80%

The cells were completely discharged after they had reached the ∼80% of their rated capacity. The cylindrical cells, C0, C1, C3, C4, and C6 were opened in a glove box filled with Argon atmosphere. The oxygen level was maintained at ∼88 ppm and the dew point was *sim* -34 C. The cell was unrolled, and the long anode and cathode strips were separated. Each electrode strip was then divided into six sections. Section # 1 is near the outer circumference and section # 6 is near the center of the cylindrical cell. Cell, C16 was opened in ambient environment and the cathode and anode strip was divided into five sections.

Chapter 6: Multi-scale Characterization of Cathode - Physical and Morphological

6.1 Introduction

The success of the electric vehicle market largely depends on the cheap and affordable battery technology with long cycle and calendar life. The continuous cycling of the batteries leads to decrease in capacity (charge acceptance) and increase in the internal resistance (power fade) [Chehab et al., 2006]. The decrease in capacity and increase in the internal resistance of the battery is a result of underlying damage or degradation of materials within the batteries caused by several simultaneously occurring physiochemical processes. The kinetics of the material degradation may exhibit cascading effects due to interactions between crystal structure, change in active material concentration, change in size, and shape of active material, as well as, precipitation of micro/nano-scale secondary phases. The mechanisms that lead to the degradation of the battery materials are often studied under laboratory conditions by building a coin cell with the material of interest. The coin cells due to their small size are often cycled for limited number of cycles with relatively lower C-rate. The number of charge/discharge cycles seen by commercial batteries before EOL could be much higher. Also the commercial batteries would see much higher

C-rate during their cycle life. Thus study of commercial batteries is more relevant to the identification of the degradation mechanisms of the various battery materials.

The commercial batteries vary in size and shape from the coin cells. The cylindrical cell (**Fig. 6.1a**) is the most widely used among the available battery shapes. The components are rolled and packed in a cylindrical case. The cylindrical cell can hold more active material than any other battery shape. Hence, it has more energy density. Also, they are easy to manufacture and have high mechanical stability [Buchmann, 2001].

The prismatic cell (**Fig. 6.1b**) was developed in early 1990s to serve the need of the semiconductor industry, where devices continue to get smaller and smaller. Due to its thinner geometry, it has lower energy density. Also, it becomes a manufacturing challenge to pack the components into a thinner geometry. They are mechanically less stable than cylindrical batteries and tend to bulge out due to a lack of proper venting for built up gases [Buchmann, 2001].

The introduction of the pouch cell (**Fig. 6.1c**) in 1995 drastically reduced the manufacturing cost of the battery systems. The components are stacked in a layer and enclosed in a foil instead of a metallic casing. It is very flexible and the most compact among the available battery shapes. It is lightest in weight as compared to any other battery shape, but has a slightly lower energy density and load current. The drawbacks of the pouch cell are swelling due to the evolution of gases and high sensitivity to twist [Buchmann, 2001].

Thus study of the coin cell would also fail to reveal the effect of size, shape, and packaging, which could be prominent in case of the commercial batteries. As shown in the **Fig. 6.2a** and **Fig. 6.2b** when a $LiFePO_4$ based commercial cylindrical cell

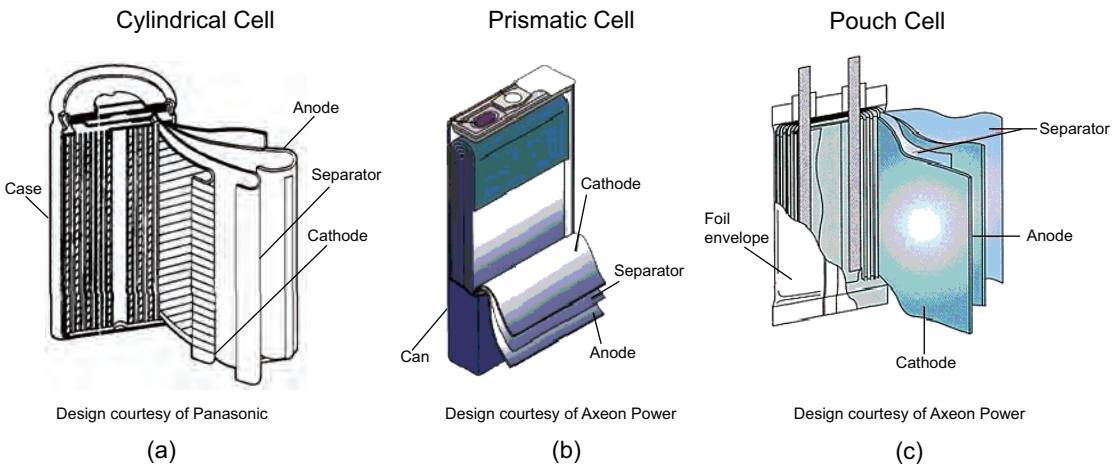

Figure 6.1: (a) Schematic of a cylindrical lithium-ion battery. The components are rolled and packed in a cylindrical case. (b) Schematic of a prismatic lithium-ion battery. The components are stacked in layers and enclosed in a rectangular casing. (c) Schematic of a pouch cell. The components are stacked in layers and enclosed in a foil envelope [Anonymous, 2007]

is disassembled and the jellyroll is unrolled, the length of each individual electrode is ~ 1.5 m. In case of the $LiFePO_4$ battery the active $LiFePO_4$ material is synthesized as a nanomaterial. Nanomaterials, due to their unique characteristics, are very instrumental in developing energy storage devices with high energy and power density. Energy conversion in energy storage devices takes place with a chemical reaction at the surface, charge transfer, etc. These processes occur at the nanoscale. Nanomaterials provide a large surface area to volume ratio for such processes to occur. A high surface area permits a high contact area with the electrolyte and a larger number of reaction sites. In certain cases they enable electrode reactions to occur that cannot take place for materials composed of micrometer-sized particles. The kinetics of the energy storage device are governed by the kinetics of the diffusion process within the

device elements. Nanomaterials help in reducing the diffusion length and hence improve the kinetics of the operation of an energy storage device. Thus, nanomaterials can improve the charge-discharge rates. The electron transport within the electrode is also improved by nanometer-sized particles.

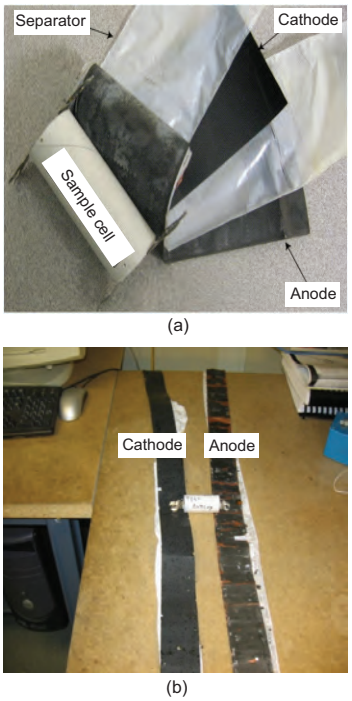

Figure 6.2: (a) A picture of a typical cylindrical cell. The cell is typically referred to as 18650 where the diameter of the cell is 18 mm and the length is 1650 mm. The jelly roll of the cell components is also seen here. (b) A picture of the dissembled and unrolled components of the cell. The length strip on the left is the anode and the strip on the right is cathode. The length of each electrode is $\sim$ 1.5 m long and 25 mm wide

One can not randomly pick an area on the long cathode strip and hope to see the effects of the aging mechanisms on the $LiFePO_4$ nanoparticles. Exhaustive search

over the entire electrode strips will be physically impossible with available microscopic characterization techniques. Thus to address this issue and still investigate the cascading effects of various physiochemical process on the nanoparticles a multi-scale characterization plan is necessary for understanding the degradation mechanisms in commercial batteries. Techniques such as SEM, TEM, XRD etc., could be used to study various properties such as the morphology, phase transformation, electronic properties etc. These characterization techniques could be coordinated with each other to focus on a specific location on the electrode surface. Thus the results are could be analyzed in conjuntion with each other and at different length scales based on the technique. As a result, these studies would provide a comprehensive understanding of the material degradation with spatial resolution.

With this objective in mind various experimental techniques shown in **Fig. 6.3** were chosen to address the physical/morphological changes, the electrical changes as well as the chemical and structural changes in the cathode material. The techniques were spanned over different length scales to understand the effects of aging on these three parameters. Thermography was chosen as the starting technique to scan the entire length of the cathode strip and identify the potential areas of degradation. It is assumed that the changes in the thermal properties also affect the electrical properties of the material. Based on the thermal maps the samples were prepared for further analysis with SEM, AFM and TEM. The capacity curves and the internal resistance are the aging metrics at the system level. But to understand the effects of the morphological changes on the electrical properties of the material at micro/nano scale, characterization techniques such as SSRM and KPM available with AFM were included. Chemical and structural analyses techniques were chosen to investigate the

local chemical changes, local Li environment and its bonding with the neighboring elements in the $LiFePO_4$ crystal structure as well as to identify the effect of aging on the Li concentration profiles within the electrodes. The physical/morphological studies are discussed in this chapter. **Chapter 7** discuss the electrical characterization and the chemical and structural characterization is discussed in **Chapter 8**.

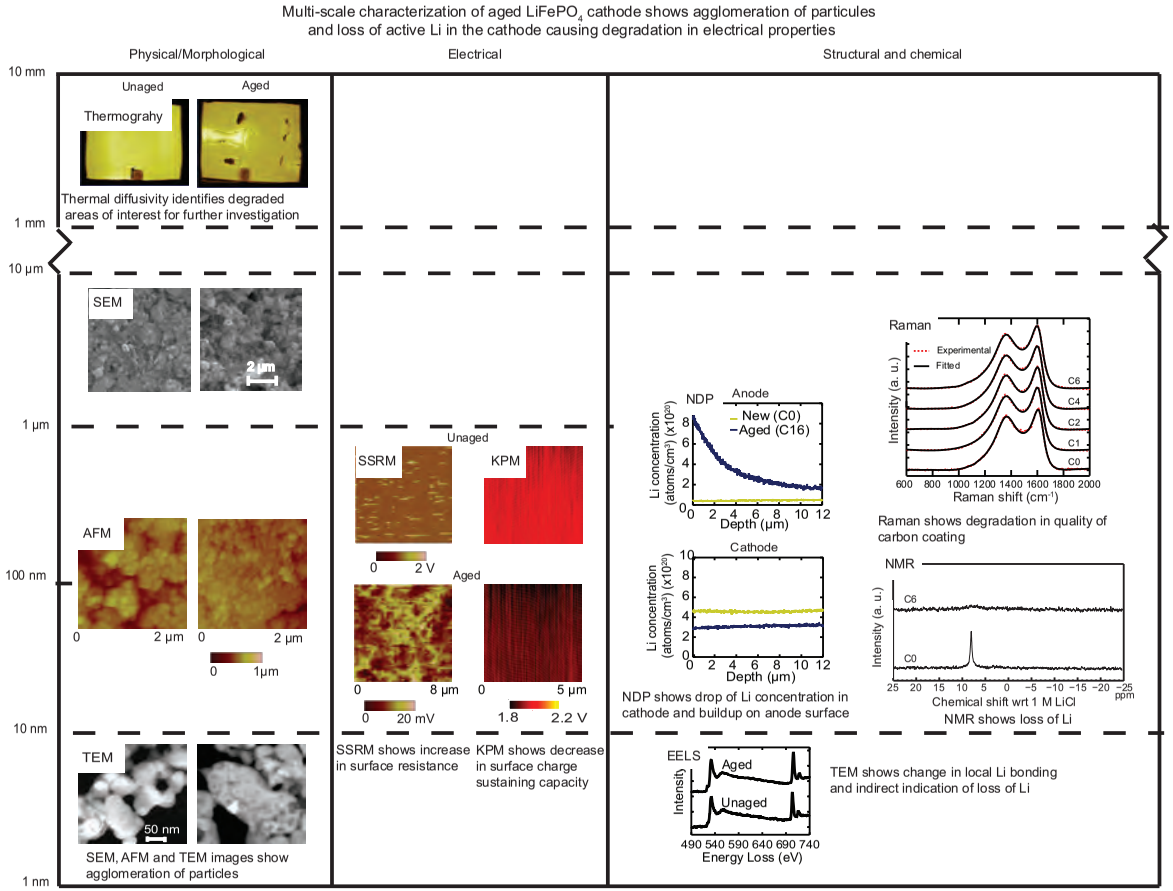

Figure 6.3: A chart displaying the various techniques useful at different length scales for multi-scale characterization of the materials

6.2 Thermography (mm)

Thermography is used to measure the variations in temperatures through thermal imaging of the objects. Here the thermography by flash method is used as the first step in the multi-scale characterization of the $LiFePO_4$ cathode material. The flash method, which was introduced by Parker et al. [1961] has been used extensively in measurement of thermal characteristics such as thermal diffusivity, thermal conductivity, etc... of various different kinds of materials. In this simple technique the front face of the sample with slab geometry receives a pulse of radiant energy coming from a laser or a flash lamp. The temperature rise of the opposite face is captured through high resolution, high frequency thermal imaging by an infrared (IR) camera . The average temperature rise in the sample is only few degrees above the initial value. This temperature rise curve is used for thermal characterization of the samples [Larsson and Koyama, 1968; Vozár and Hohenauer, 2003].

Several authors have successfully applied this technique for several different materials. Degiovanni et al. [1996], Krapez [1999] Lafond-Huot and Bransier [1982], Luc and Balageas [1984], and Philippi et al. [1995] used it to study the anisotropic materials. Batsale et al. [1996], Ramond et al. [1998], and Ramond et al. [1999] used it to study complex heterogeneous media. Azizi et al. [1989], Moyne et al. [1988], and Moyne et al. [1990] studied porous materials. Andre and Degiovanni [1995], Lazard et al. [2004], and Hahn et al. [1997] applied it to study semi-transparent materials. Conquard and Panel [2009] used it to study liquids or pasty materials. There are also several reviews published about the theoretical and practical applications of this technique by [Righini and Cezairliyan, 1973; Degiovanni, 1977; Taylor, 1979; Balageas,

1989; Taylor et al., 1984; Maglić et al., 1992; Sheindlin et al., 1998; Baba and Ono, 2001; Vozár and Hohenauer, 2001, 2003].

As large areas can be easily scanned with this technique, it becomes an ideal choice to scan the long cathode strips for any physical and/or morphological damages. Nagpure et al. [2010] have demonstrated the application of this technique in battery research by capturing 2D thermographs of the cathode strips harvested from unaged and aged commercial cells. The setup to capture the thermal maps of the samples is discussed in ASTM 1461 92 standard [Anonymous, 1992] and is shown in **Fig. 6.4**. The main features of this setup are the flash lamp, sample mount, high resolution IR camera, and data acquisition system. The high energy pulse required in this experiment was generated by Profoto, Acute 2, flash lamp with a 2400 W-s capacity. The flash lamp was operated to deliver a finite pulse of energy at 300 W-s. The sample mount was a custom made hollow box with a square slot of approximately 63.5 mm x 63.5 mm on one face. The flash lamp was centered over this slot. A circular hole of approximately 90mm was cut on the opposite face. The IR camera lens was inserted through this hole and focused on the sample. The thermal maps were taken with an IR camera from Indigo Systems, Phoenix Mid-wave IR Camera, with a 320 x 256 pixel resolution and InSb focal plane array. The frequency of the camera is set at 346 Hz. The data acquisition system was built into the IR camera equipment.

The long cathode strip was divided into equally spaced five sections each ~ 2.5 in wide. The sample was mounted flushed on the face with the square slot on the sample mount. The center of the flash lamp coincides approximately with the center of the sample so that the heat pulse is uniformly incident on the sample. The IR

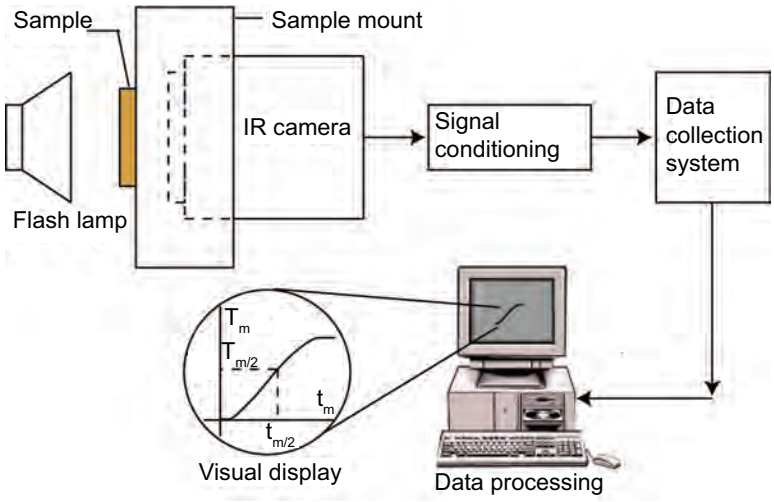

Figure 6.4: Schematic of thermal diffusivity measurement by Flash Method (adapted from [Anonymous, 1992])

camera lens was focused on the opposite face of the sample with the center of the lens aligned approximately with the center of the sample. The finite heat pulse from the flash lamp was incident on the front face of the sample. The heat gained by the sample from this pulse is conducted through its thickness to the rear face. As such the rear face of the sample is heated and its temperature increases. The IR camera captures this heat gained by the rear face at a frequency of 346 frames per second. The experimental setup was under ambient conditions and as such all the thermal maps were obtained under ambient conditions.

The thermal maps of the aged and unaged sample for all five sections (**Fig. 6.5a**), shown in **Fig. 6.5**, were taken when the temperature of the rear face of the sample reached the maximum value. In these thermal maps the dark spots represent the cold areas while the bright spots represent the hot areas. The dark spots are more

prominent in the aged sample (right side) as compared to the unaged sample (left side).

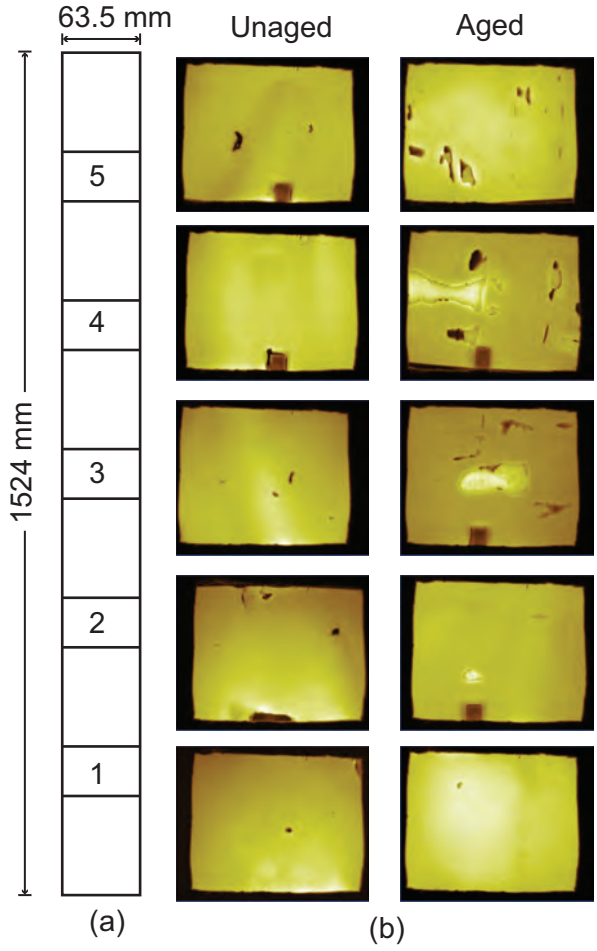

Figure 6.5: (a) Sectioning of the cathode for the thermal imaging. Section # 1 is near the core of the cylinder and section # 5 is near the out edge of the cylinder. (b) Thermal maps of unaged and aged cathode samples for all 5 sections

The dark spots are mostly in areas where the spalling of the cathode material from the current collector was observed. The spalling could be attributed to the disbonding, cracking or buildup of residual stress and strain between the current

collector and the cathode material interface. The spalling could also be attributed to the shocks and vibrations during disassembling of cells and/or handling of the long cathode strip. Thus the reason for spalling could not be conclusively attributed to any specific damage mechanism. Since spalling was a result or effect of certain underlying damage mechanism the aging studies were focussed on areas without any visible damage.

Thermal diffusivity was used as a damage metric in the areas without any visible damage (no spalling). **Figure 6.6a** shows the temperature rise of the rear face of the sample in terms of IR counts. The temperature rise shown here is for section # 4 of the aged and the unaged cathode samples shown in **Fig. 6.6b**. An area with a uniform IR intensity was randomly chosen in the thermal map of the aged and unaged sample for thermal diffusivity analyses. The IR counts are obtained over this area from the instant the heat pulse was incident on the sample until the temperature of the sample reaches a steady state value. A base line temperature was identified in these plots as the temperature just before the pulse is incident on the sample (T_{ini}). Then the maximum temperature was measured as the steady state temperature of the rear face of the sample (T_{max}). The half rise time ($t_{1/2}$), i.e. the time required from the initiation of the pulse on the front face of the sample to the time at which the temperature of the rear face of the sample reached half the difference between T_{ini} and T_{max}, was calculated. The thermal diffusivity for the sample was then calculated using the following formula [Anonymous, 1992]:

$$\alpha = 0.13879 \frac{L^2}{t_{1/2}} \tag{6.1}$$

where α is the thermal diffusivity (m^2/s), L is the thickness of the sample (m), and $t_{1/2}$ is the half rise time (s). It is important to note that the **Eq. 6.1** is not dependent on the absolute value of T_{max}. Therefore, the observed differences in maximum IR counts between aged and unaged samples as seen in **Fig. 6.6a** are not important in these analyses.

Figure 6.6b shows comparison of the thermal diffusivity between the unaged and the aged sample over all 5 sections. As can be seen in this figure the thermal diffusivity of the aged sample was more than the unaged sample in all 5 sections. This indicates that the rate of heat conduction in aged samples is higher than the unaged sample which can be attributed to the change in the porosity of the cathode material. The differences in the thermal diffusivity values between aged and unaged samples are significantly less in sections 1 and 5. These sections are near the core of the cylinder and near the outer edge of the cylinder, respectively. The differences in the thermal diffusivity are more prominent in sections 2, 3, and 4 of the samples. Nagpure et al. [2010], believed that the different rate of change in the porosity in various sections leads to the non-uniform change in the thermal diffusivity across the sections.

Theoretically, thermal diffusivity is given as the ratio of the thermal conductivity to volumetric heat capacity as follows:

$$\alpha = \frac{k}{\rho c_p} \tag{6.2}$$

where α is the thermal diffusivity (m^2/s), k is the thermal conductivity ($W/m-K$), and $\rho\ c_p$ is the volumetric heat capacity (J/m^3K). The **Eq. 6.2** is strictly applicable only to monolithic material. Since, the cathode material is a composite,

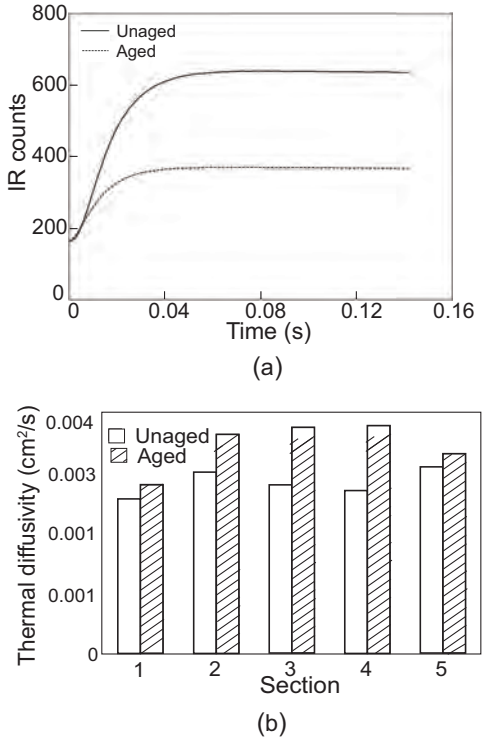

Figure 6.6: (a) Temperature rise curves for unaged and aged samples (section # 4). (b) Comparison of thermal diffusivity between unaged and aged samples

Nagpure et al. [2010] associated the increase in thermal diffusivity with a change in k, ρ and/or c_p.

Figure 6.7 shows the schematic of a proposed mechanism explaining the increase in the thermal diffusivity of a $LiFePO_4$ cathode due to aging [Nagpure et al., 2010]. As a first order approximation the cathode can be considered as a porous medium. Also, it can be assumed here that the heat diffuses through the cathode only due to conduction. As the cathode ages the nanoparticles tend to coarsen by sintering. Due to this sintering of the nanoparticles, the effective surface area per unit volume decreases [Exner and Arzt, 1983], with an associated decrease in the porosity of the cathode. The decrease in the porosity can also expose larger area of the aluminum current collector. Since aluminum has high thermal diffusivity ($8.418 \times 10^{-5} m^2 s^{-1}$), the overall thermal diffusivity of the aged sample may show an apparent increase [Brown and Marco, 1958; Eckert and Drake, 1959; Holman, 2002]. It is interesting to note that the sintering of oxide particles takes place at high temperatures. The onset of sintering in the cathode material may be attributed to the high surface energy of the $LiFePO_4$ nanoparticles. [Zhang and Miser, 2006] have observed coalescence of oxide particles with no external heating. In general, as the porosity of the medium decreases, the thermal conductivity increases, and hence, the aged sample shows increase in thermal diffusivity [Kononenko et al., 1968; Bhattacharya et al., 2002].

In summary thermography bridges the gap between different length scales and proves to be an effective technique to relate the damage mechanisms of the cathode at mm length scale to micro/nanoscale. The thermal diffusivity increases as the cathode ages during the cycling of the batteries. The increase in the thermal diffusivity was attributed to the decreased porosity of the cathode samples due to the coarsening of

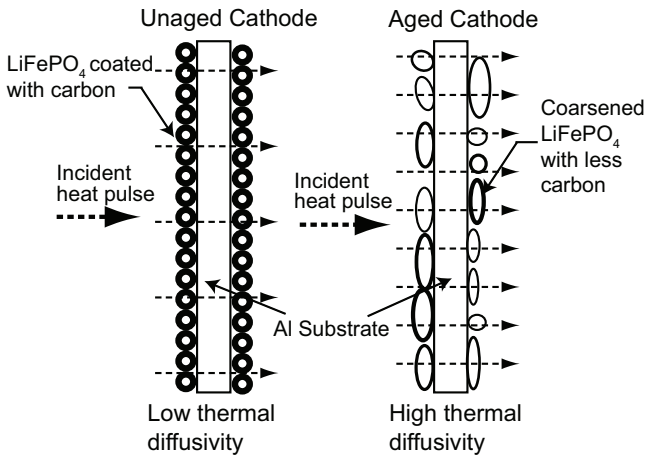

Figure 6.7: (a) Temperature rise curves for unaged and aged samples (section # 4). (b) Comparison of thermal diffusivity between unaged and aged samples

the $LiFePO_4$ nanoparticles. The 2D thermal maps and the thermal diffusivity calculations help in making samples for further mico/nano level characterization studies.

6.3 Digital microscopy (microns)

Advances in the lens design and manufacturing has helped the development of the high-resolution optical microscope. The issues such as optical aberrations, blurring of the images have been overcome in modern optical microscope. Coupled with these advances, the advances in the digital imaging have lead to the development of the digital microscopes. In digital microscope the eyepiece of an optical microscope is replaced with a charged coupled device cameras. Digital microscopes provide added advantages of precise computer control and greater flexibility in image analysis and

processing. They have been used regularly in the files of biological sciences, nanotechnology, as well as material science and metallography. They are very useful in imaging the texture of the samples for metallographic analysis.

Digital microscopy has not been used as widely as other techniques in the study of the battery materials. **Figure 6.8** shows the digital micrographs of the unaged and aged $LiFePO_4$ anode and cathode taken along the cross-section (thickness) of the electrode strips. They are very useful in understanding the basic construction and layout of the electrode strips. In **Fig. 6.8a** the middle vertical region represents the copper current collector. The graphite coating is seen on either side of this current collector. Similarly, in case of **Fig. 6.8b** the middle shiny vertical region in the images is the aluminum current collector. The active material ($LiFePO_4$) is coated on either side of this current collector substrate. Due to the dense packing of the active material the nanoparticles structure is not visible at the resolution available in these images. The edges of the current collector have been smeared off and the coating of the active material is not uniform on either side in case of the aged sample. Using digital image processing technique on these micrographs the thickness of the current collector and the coatings on each side is measured as $\sim 10\mu m$ and $\sim 75\mu m$ respectively. This data is very useful input to the electrochemical models of the battery performance [Marcicki et al., 2011].

In summary, digital micrography contributes very little towards identifying the degradation mechanisms of the cathode material. It is unclear if the uneven active material coating thickness is a manufacturing defect or an aging effect. Nonetheless these studies provide important information about the physical dimension of the cathode useful in electrochemical modeling of the battery performance.

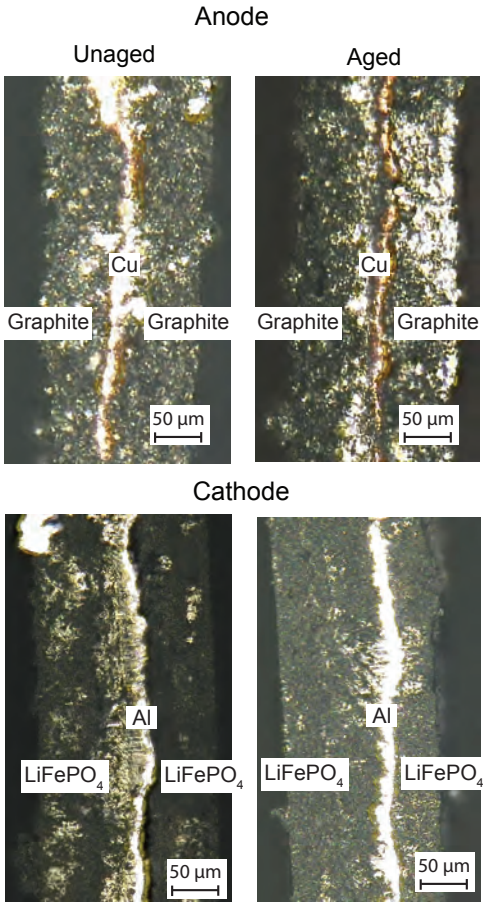

Figure 6.8: Digital micrographs of unaged and aged graphitic anode and $LiFePO_4$ cathode across the thickness

6.4 Scanning electron microscopy (SEM) (microns)

SEM is widely used as a non-destructive tool for characterization and analysis of the materials. The focused high-energy electron beam incident on the sample generates signals that are analyzed for the morphology, crystal structure, chemical composition, and material orientation. SEM is widely used in the lithium ion battery research to produce high magnification images of the nanostructured active materials. It is often used to understand the morphology of the synthesized cathode material and verify the nanostructure of the materials [Benoit and Franger, 2008]. SEM can be used to identify the major physical and or morphological structures in the active materials. Such studies can reveal any particle cracking, particle separation, and particle agglomeration [Abraham et al., 2006].

Figure 6.9 shows the SEM micrographs of the samples harvested from the unaged and aged cells. The SEM micrographs reveal the coarsening of the nanoparticles in the aged samples as compared to the unaged sample. The particles in the unaged sample are of the order 4050 nm while in the aged sample the particles are of the order 240350 nm. As can be seen in the **Fig. 6.9**, in commercial batteries the active material is densely packed on the current collector. Thus higher resolution and magnification SEM images would be necessary to analyze the particle size and its distribution on the cathode surface to study the effect of the coarsening on the overall performance characteristics of the battery.

The coarsening of the particles leads to a decrease in the effective surface area of the particles affecting the rate of the reaction. The change in the particle size would also affect the diffusion kinetics of the lithium ions during charging and discharging cycles. The coarsening phenomenon can also lead to the disbonding of these particles

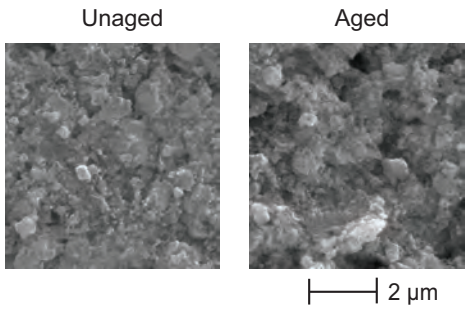

Figure 6.9: SEM micrographs of unaged and aged $LiFePO_4$ cathode samples extracted from section # 4

from the aluminum substrate causing physical failure or cracking of the active material and increase in the internal resistance due to loss of contact. The coarsening can also lead to separation of particles leading to loss of contact between the particles.

6.5 Atomic force microscopy (AFM) (micron nm)

Since its development by Binning et al. [1986] AFM has played a vital role is surface characterization of various different materials such as semiconductors, insulators, bio-materials etc... The commercial AFM is available in two different versions. Both the AFMs operate on same basic principle. The only difference is that in one version the tip is stationary and the sample moves relative to the tip while in the other version the sample it stationary and the tip moves relative to the sample. In either configuration, a sharp tip at the free end of a flexible cantilever is brought into contact with the sample. **Figure 6.10** shows the former version of the commercially available AFM. A laser beam from a diode laser (5 mW max peak output at 670 nm wavelength) is focused by a prism onto the back of a cantilever near its free end, tilted downward at about 12deg with respect to the horizontal plane. The reflected

beam from the cantilever is directed through a mirror onto a split photodetector with four quadrants (commonly called position-sensitive detector or PSD). The differential signal from the top and bottom photodiodes provides the AFM signal, which is a sensitive measure of the cantilever vertical deflection.During scanning a constant normal force is applied on the cantilever. The different features of the surface of the sample cause the cantilever to deflect vertically and laterally as the sample and the tip move relative to each other. The feedback circuit maintains the vertical deflection of the tip. The signal from the feedback circuit is thus the direct measure of the surface topography of the sample [Bhushan, 2008].

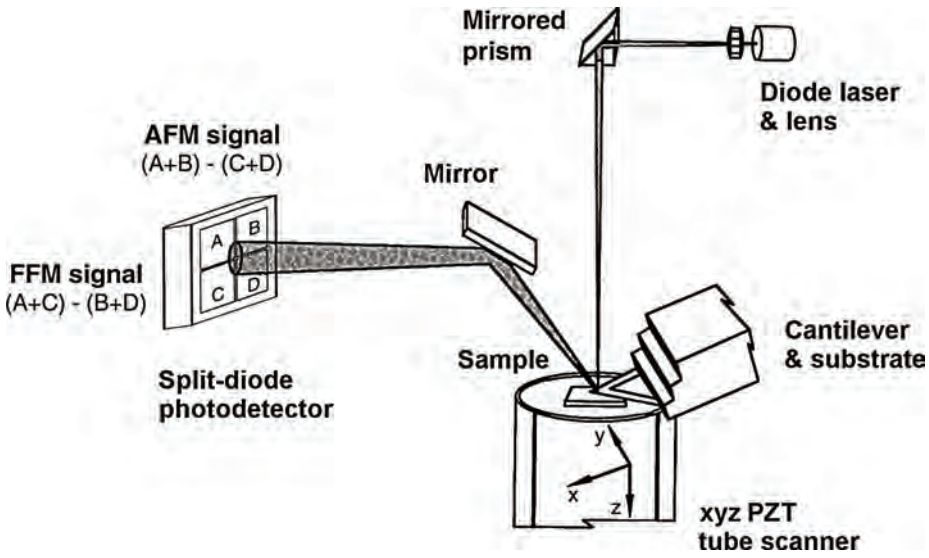

Figure 6.10: Principle of operation of a commercial AFM. (The schematic is for Multimode™ AFM (Veeco Instruments, Inc.). (Adapted from [Bhushan, 2008])

A brief review of AFM techniques used in Li-ion battery research has been provided by [Nagpure and Bhushan, 2009]. This technique provides surface morphology maps of the cathode samples with micron to nm resolution. These maps are useful in studying the grain coarsening phenomena. Along with this standard measurement, AFM modules are also helpful in measuring surface electrical properties. These studies have been discussed in **Section 7.3** and **Section 7.3.1**. **Figure 6.11** shows the AFM surface height image of the $LiFePO_4$ cathode sample harvested from the unaged and aged cells. As can be seen from the images, the $LiFePO_4$ nanoparticles tend to coarsen in the aged samples as compared to the unaged samples. The same phenomena was observed with SEM micrographs at micron length scales. The AFM surface height images have higher spatial resolution than the SEM micrographs. Hence they might be more useful in statistical quantification of the particle size distribution.

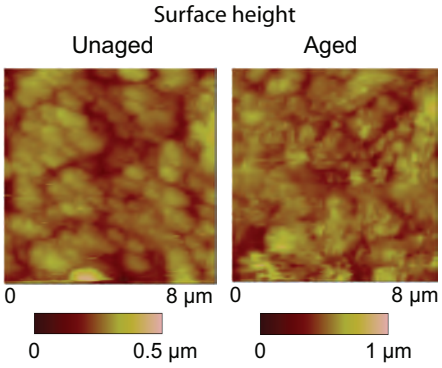

Figure 6.11: Surface height maps of a $LiFePO_4$ cathode sample harvested from unaged and aged cells. A +1V DC bias is applied to the sample

6.6 Transmission electron microscopy (TEM) (nm)

TEM is a highly effective and versatile electron microscope technique to image, analyze and characterize the materials at length scales of the order of nanometers [Williams and Carter, 2004]. Some of the application of TEM in lithium ion battery research has been for studying the nanoparticle morphology, phase change in the nano particles[Delmas et al., 2008; Laffont et al., 2006; Chen et al., 2006]. In multi-scale characterization plan TEM is used to provide high resolution images of the cathode samples for understanding the particle morphology at nanometer length scale.

TEM though very useful for high resolution imaging requires a very careful sample preparation which should be thin so that they are electron transparent. The TEM samples were prepared on a FEI Helios™ 600 -Dual beam, focused ion beam system (FIB). The TEM samples were extracted from the surface through the thickness of the sample using lift-out technique. The lift-out technique used here has been discussed in Giannuzzi et al. [1997] and Giannuzzi and Stevie [1999]. The steps followed in the lift-out technique are shown in **Fig. 6.12** and briefly discussed here. A clean area is found on the sample and imaged with the ion beam (1). Then Pt is deposited on the surface using a very small current of 2.8 nA (2). The sample is turned by 20deg in one direction, and the area around the Pt deposit is milled away using a milling current of 9.3 nA. A similar step is repeated to mill the area on the other side of the Pt deposit (3). The sample is then turned by 7deg, and a trench is cut along the depth of the sample (4) to extract the TEM foil. In step 5 the omniprobe is attached to the foil, and the foil is pulled from the rest of the sample. The foil is then welded onto a TEM Cu grid (GRD-0001.01.01) using Pt (6) and detached from

the omniprobe. Finally, the foil is further thinned to approximately ~ 200 nm using the ion beam to make it electron transparent.

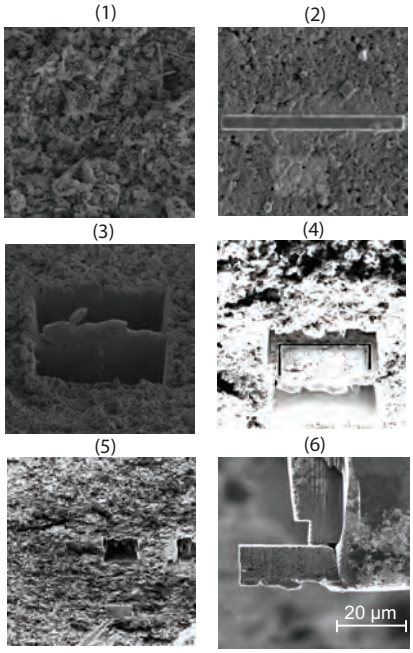

Figure 6.12: Steps showing TEM sample preparation using FEI Helios 600^{TM} dual beam focused ion beam system (FIB)

Morphologies and nanostructures of the $LiFePO_4$ samples are shown in the TEM images (**Fig. 6.13**). They have the same global morphologies. Particles of the aged sample were bigger than the particles of the unaged samples. The samples have several layers of nanoparticles and, as such, contrast exists among the overlapping particles. This makes particle size analysis difficult, but the coarsening phenomenon is clearly visible in **Figure 6.13b**. Good statistical analysis of the coarsening and the particle size variation can only be achieved with a more subtle TEM sample extraction process

that would allow quantitative measurement of the relative fractions of agglomeration and sintering, without destroying the configurations observed in the **Figure 6.13**.

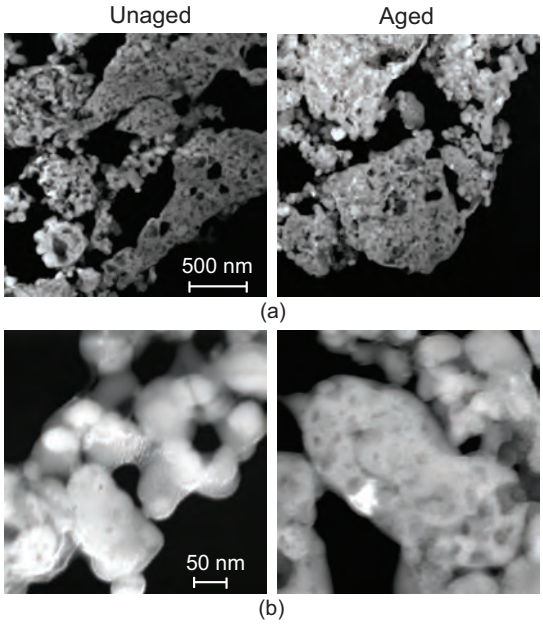

Figure 6.13: (a) TEM images of unaged and aged $LiFePO_4$ cathode samples at lower magnification (b) TEM images of unaged and aged $LiFePO_4$ cathode samples at higher magnification. The images are from the central area in (a)

6.7 Summary

The electrodes within the commercial battery have been characterized by several different techniques for physical and morphological changes with resolutions ranging from mm to nm. Techniques including thermography, SEM, AFM and TEM prove very helpful in characterizing the long cathode strip from mm to nm length scales.

The thermal maps along with thermal diffusivity measurement bridges the gap between different length scales and proves to be an effective technique to relate the

damage mechanisms of the cathode at mm length scale to micro/nanoscale. The samples for micro/nano studies are extracted based on the degradation observed on 2D thermographs. The thermal diffusivity increased as the cathode ages during the cycling of the batteries. The increase in the thermal diffusivity was attributed to the decreased porosity of the cathode samples due to the coarsening of the $LiFePO_4$ nanoparticles.

The physical/morphological studies reveal the main aging effect as the coarsening of the $LiFePO_4$ nanoparticles. A schematic of the coarsening phenomena is shown in **Fig. 6.14**. The average particle size increases during aging of the battery. The coarsening of the nanoparticles is visibile in the SEM micrographs, AFM surface height images, as well as high resolution TEM images.

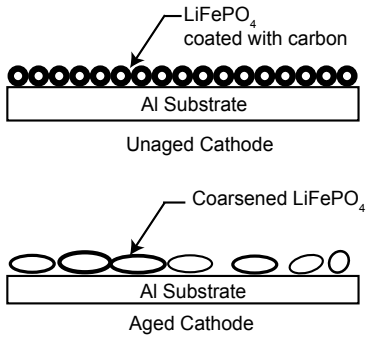

Figure 6.14: (A schematic showing coarsening of the $LiFePO_4$ nanoparticles during aging of the battery.

The coarsening has several effects on the performance of the battery. The coarsening of the particles leads to a decrease in the effective surface area of the

particles affecting the rate of the reaction. The change in the particle size would also affect the diffusion kinetics of the lithium ions during charging and discharging cycles. The coarsening phenomenon can also lead to the disbonding of these particles from the aluminum substrate causing physical failure or cracking of the active material and increase in the internal resistance due to loss of contact. The coarsening can also lead to separation of particles leading to loss of contact between the particles. The effect of coarsening on the electrical properties of the cathode material have been presented in **Chapter 7**.

Chapter 7: Multi-scale Characterization of Cathode - Electrical

7.1 Introduction

In this chapter the various tecnhiques used to characterize the electrical performance of the aged cathode materials are discussed. The physical/morphological characterization showed the coarsening go the $LiFePO_4$ nanoparticles in the aged cathode samples. The effects of this coarsening phenomena on the electrical properties of the cathode material are studied through different techniques. At the system level the charge/discharge curves and the change in the internal resistance are used as the metrics to characterize the electrical performance of the batteries. As shown earlier in **Fig. 6.3** SSRM and KPM are used to characterize the electrical properties of the cathode material at micron-nm scale lengths.

7.2 System level capacity fade and resistance increase

The continuous cycling of a battery leads to capacity fade and increase in the internal resistance. The capacity and the internal resistance are used as the metrics for measuring aging at the system level. **Figure 7.1a** shows typical discharge curves of a $LiFePO_4$ based Li-ion battery cycled at 16 C-rate between 45 and 55 % SOC. As

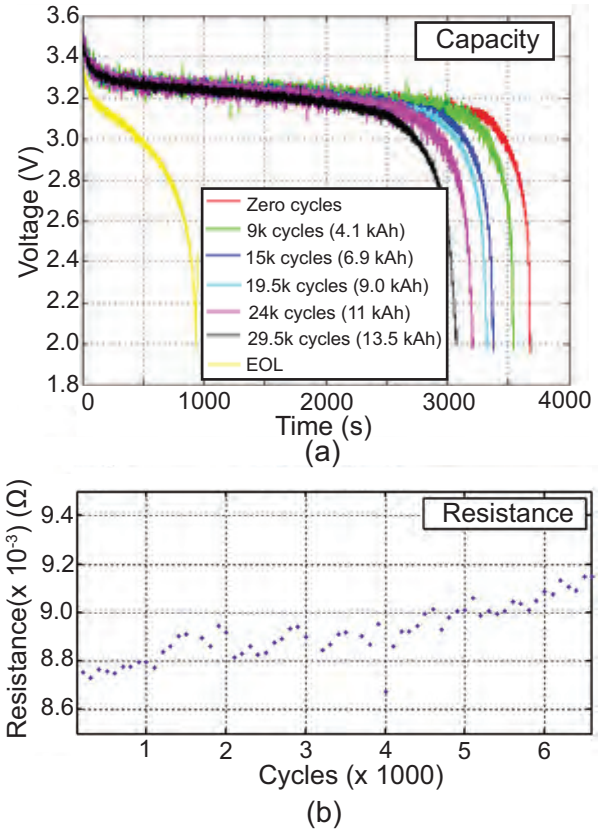

Figure 7.1: (a) A typical set of discharge curves (voltage versus time) is shown. The knee of the voltage curve is approached faster as the capacity of the cell decreases. (b) Internal resistance increases with aging of the cells.

seen in this figure, as the battery ages the knee of the discharge curve is approached much earlier than expected. Thus the total current drawn from the battery is less as compared to the beginning of the life. Similarly as seen in the **Fig. 7.1b** the internal resistance of the battery calculated from the open circuit potential, the loading current and the voltage drop due to the load increases during continuous cycling of the batteries.

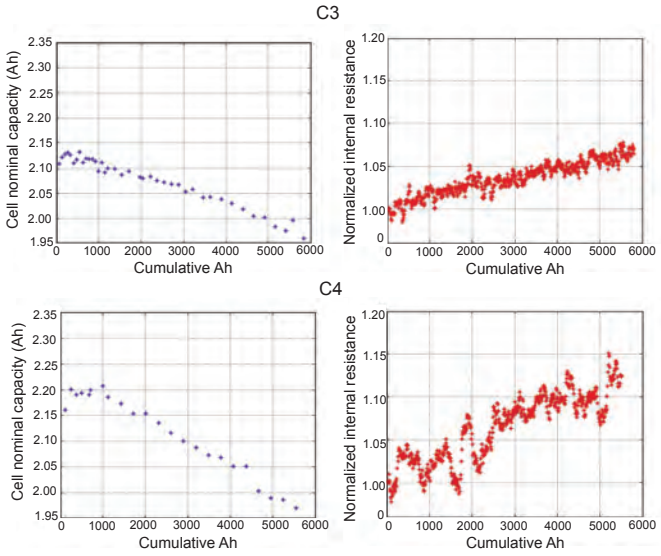

Figure 7.2: Capacity drop and resistance increase in cells C3 and C4 for multi-scale characterization studies

In **Fig. 7.2** the capacity and the internal resistance of the batteries C3, and C4 and are plotted against the cumulative Ah. The cumulative Ah is the total Ah used during charging and discharging of the cell. The data shows the drop in the capacity and increase in the internal resistance during the cycling of the batteries and thus measures the performance of the batteries according to the system level aging metrics. The drop in the capacity of C4 battery is at a slightly higher rate as compared to C3. Also the overall increase in the internal resistance of the C4 battery seems to be higher than C3. Thus the higher C-rate have negative effect on the performance of the batteries and the batteries tend to age faster at higher C-rates.

7.3 Scanning spreading resistance microscopy (SSRM)

Advances in AFM instrumentation has led to the development of a technique known as scanning spreading resistance microscopy (SSRM) [Bhushan, 2007]. The SSRM module used in AFM measures the surface resistance between the conductive tip and the sample while the tip is scanned in contact mode across the sample surface. The most important application of the SSRM technique can be found in the mapping of carrier concentration inside a semiconductor device [Slater, 2000].In contrast to SSRM, there also exists a method called current sensing AFM (CSAFM) to measure the surface current between the conductive tip and the sample. This has been previously used in lithium ion battery research. A review of AFM techniques used in electrical characterization of battery materials has been presented in Nagpure and Bhushan [2009].

The nanoscale surface resistance measurements were taken by Nagpure et al. [2009] with a Nanoscope IIIa Dimension™ 3000 AFM equipped with the SSRM application module. The conductive SCM PIT (Veeco Instruments) probes used in this study were coated with platinum-Iridium on front and back side and had a nominal tip radius of 20 nm. A known DC bias voltage of +1 V was applied between the sample and the conductive tip, and the current was monitored using a logarithmic current amplifier built into the SSRM sensor, as shown in the schematic in **Fig. 7.3**.

The module applies the same bias to the 1M reference resistor mounted inside the module. The resistance is then measured by a comparator that compares the current flowing through the sample to the current flowing through the reference resistor. The output of the SSRM module is in volts. The module is calibrated by connecting several resistances of known value in the module instead of the tip-sample.

For example, if 1 M resistance is connected instead of the tip-sample, the output of the comparator is 0 V as the same current flows from the sample resistance and the reference resistor. Thus a 0 V output corresponds to a 1 M resistance between the tip and the sample. When a positive bias is applied between the tip and the sample, the output voltage is inversely proportional to the surface resistance while it is directly proportional to the surface resistance if a negative bias is applied. The total resistance between the tip and the sample depends on the contact resistance, the spreading resistance, and the bulk resistance. One of the resistances dominates the total resistance depending on the contact force applied on the tip, the applied bias and the condition of the sample material. Depending upon the material, when a high enough contact force and a suitable bias is applied, a stable electrical contact is established between the tip and the sample, and the total resistance measured will be the surface resistance dominated by the contact resistance and the spreading resistance [Anonymous, 2004].

Figure 7.4 shows the SSRM surface resistance image of the $LiFePO_4$ cathode sample harvested from the unaged and aged cells. As the module configuration when +1 V is applied between the tip and the sample, the higher voltage reading represent lower surface resistance. The surface resistance scale on the unaged sample is 0-2 V, while the scale on the aged sample is 0-20 mV. The lower voltage output in the case of aged samples indicates higher surface resistance as compared to unaged sample. Thus surface resistance increases as the cells are aged.

Based on their results Nagpure et al. [2009] have proposed a mechanism that leads to the increase in the surface resistance of the $LiFePO_4$ cathode sample, shown in **Fig. 7.5**. When the tip scans over the surface of the sample a circular contact

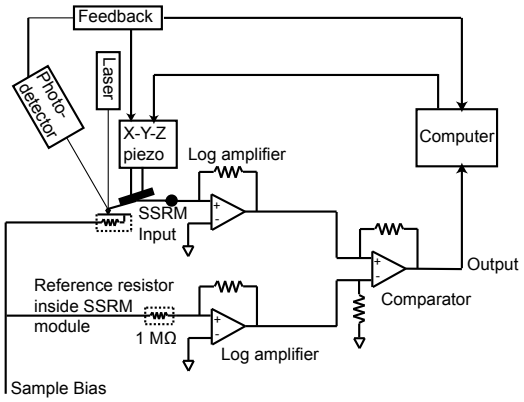

Figure 7.3: Schematic of the AFM-based resistance measurement technique where the surface height is measured in contact mode, and the resistance is measured by the current resulting from the applied sample DC bias voltage. (The schematic is for DimensionTM AFM (Veeco Instruments, Inc.). (Adapted from [Anonymous, 2004])

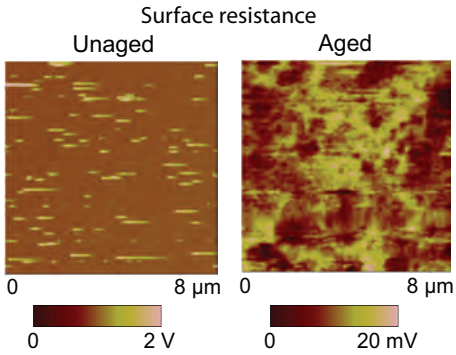

Figure 7.4: Surface resistance maps of a $LiFePO_4$ cathode sample harvested from unaged and aged cells. A +1V DC bias is applied to the sample

is formed between the $LiFePO_4$ nanoparticles and the tip. As mentioned earlier, the $LiFePO_4$ nanoparticles have very poor conductivity ($\sigma = 2.10^{-9}$ S cm^{-1}) [Franger et al., 2005; Benoit and Franger, 2008], and hence to increase their conductivity, they are coated with carbon [Goodenough, 2007]. In the case of the unaged sample the total surface resistance measured is the resistance of the carbon-coated $LiFePO_4$ nanoparticles [(R_u]. Due to the coarsening of the nanoparticles the overall resistance increases to [(R_a].

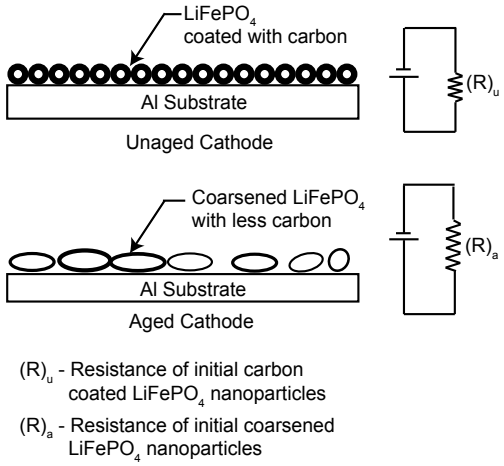

Figure 7.5: Schematic of a proposed mechanism explaining increase in the surface resistance of a $LiFePO_4$ cathode due to aging

The coarsening may also causes loss of the carbon coating which leads to the further increase in the resistance of these particles. In addition to this, the total surface resistance of the aged sample could increase due to the additional resistance from the nano crystalline deposit (NCD) formed on the cathode surface. NCD is

formed due to the chemical reactions taking place at the surface of the cathode. Further experiments are needed to investigate the details of NCD on the $LiFePO_4$ cathode surface, but it was observed by Kostecki and McLarnon [2002]; Zhang et al. [2001] on $LiNi_{0.8}Co_{0.2}O_2$ cathode surface.

7.3.1 Kelvin probe microscopy (KPM)

Another technique of interest is KPM, which has been used in a variety of applications to measure surface potential. Because of the sensitive nature of silicon to charge buildup and subsequent discharge which can damage small silicon parts, surface potential measurement has been of interest in the semiconductor industry. The technique has also been used successfully to detect wear precursors from wear at very low loads using AFM based Kelvin probe methods [Bhushan, 2008, 2007; De Vecchio and Bhushan, 1998]

The use of the Kelvin probe method was extended to the study of Li-ion batteries by [Nagpure et al., 2011a]. The KPM technique is based on the contact potential difference method for measuring the electronic work function (EWF) [Zharin and Rigney, 1998]. Since EWF is strongly influenced by the surface chemical composition and Fermi level of the material KPM can detect the structural and chemical changes of the surface and provide vital information about the onset of damage. Using KPM large areas of the entire cathode electrode can be scanned quickly giving spatial information of its surface. In this study, KPM was used for the first time to characterize aging of the cathode surfaces by measuring the change in the surface potential which can be attributed to physical and chemical changes of surface.

Nanoscale surface potential measurements were taken with a Dimension™ 3100 AFM. A schematic of this instrument with KPM setup is shown in **Fig. 7.6**. The KPM measures the surface potential of the samples in interleave mode. Along one scan line on the sample, in first pass, the surface height image is obtained in tapping mode. In second pass the tip is lifted off the sample surface and a surface potential map is obtained. Both images are obtained simultaneously [Rice, 2002]. During the first pass, the cantilever is mechanically vibrated by the X-Y-Z piezo near its resonance frequency. The amplitude of the tip vibrations (not shown) is maintained at a constant value by the feedback loop as the tip scans the surface of the sample. The signal from the feedback loop is used to construct the height map of the sample surface(**Fig. 7.6a**). During the interleaved scan, the X-Y-Z piezo is switched off. Instead, an AC signal is applied directly to the conductive tip which generates an oscillating electrostatic force on the tip. The tip is scanned along the surface topography line obtained in the tapping mode with a certain lift off the sample (dotted line in **Fig. 7.6**).

To briefly describe the operating principle of KPM, consider a tip and sample interaction as seen in **Fig. 7.6a-7.6d**. When the tip and sample are electrically connected (**Fig. 7.6a**) electrons flow from the material with the lower work function to the material with the higher work function. Due to the difference in the work function of the electrically connected tip and the sample an electrostatic contact potential difference (or surface potential difference) is created between the tip and the sample [Zharin and Rigney, 1998]. The value of this surface potential (Φ) is given by the following equation

$$\Delta\Phi = \frac{\Phi_{tip} - \Phi_{sample}}{e} \tag{7.1}$$

where Φ_{tip} and Φ_{sample} are work functions of the tip and the sample, respectively, and e is the magnitude of the charge of one electron. Φ will be affected by any adsorption layer and the phase of the material near the surface. Electrostatic force is created between the tip and sample under the influence of this surface potential difference and the separation dependent local capacitance C of the tip and sample. This force is given by

$$F = \frac{1}{2}(\Delta\Phi)^2 \frac{\partial C}{\partial z} \tag{7.2}$$

where z is the distance between the tip and sample.

Along with $\Delta\Phi$, in the operation of the KPM a compensating DC voltage signal (V_{DC}) and AC voltage signal, $V_{DC}\sin(\omega t)$ (**Fig. 7.6c** and **Fig. 7.6d**), is applied directly to the tip. Thus the electrostatic force between the tip and the sample becomes:

$$F = \underbrace{\frac{1}{2}\frac{\partial C}{\partial z}\{(\Delta\Phi + V_{DC})^2 + \frac{{V_{AC}}^2}{2}\}}_{DCterm} + \underbrace{\frac{\partial C}{\partial z}(\Delta\Phi + V_{DC})V_{AC}\sin(\omega t)}_{\omega term} - \underbrace{\frac{1}{4}\frac{\partial C}{\partial z}{V_{AC}}^2\cos(2\omega t)}_{2\omega term} \tag{7.3}$$

The cantilever responds only to the forces at or very near its resonance frequency. Thus, only the oscillating electric force at ω acts as a sinusoidal driving force that can excite oscillations in the cantilever. The DC and the 2ω terms do not cause any significant oscillations of the cantilever. In tapping mode, the cantilever response (RMS amplitude) is directly proportional to the drive amplitude of the tapping piezo.

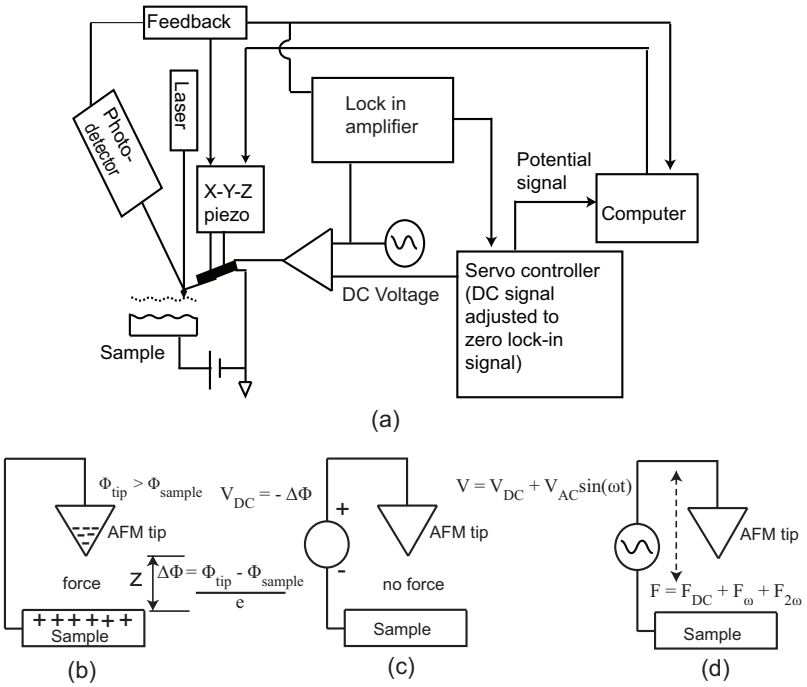

Figure 7.6: (a) Schematic of the two pass interleave scan method used in KPM. (Adapted from Rice, 2002). (b) Electrostatic potential and interaction force between a conducting tip and a sample (for illustration Φ_{tip} Φ_{sample} is assumed), (c) external DC voltage applied to nullify the force, and (d) external AC voltage with adjustable DC offset is applied to the tip which leads to its vibration. (Adapted from [Bhushan and Goldade, 2000])

Here, in the interleave mode the response is directly proportional to the amplitude of the term [Rice, 2002]. The servo controller applies a DC voltage signal equal and out of phase with so that the amplitude of the tip becomes zero ($F = 0$). This compensating signal from the servo controller creates the surface potential map of the sample [Bhushan and Goldade, 2000].

The conductive AFM tip is necessary for the KPM experiments. The tips used in these experiments had an electrically conductive 5 nm thick chromium coating and 25 nm thick platinum coating on both sides of the cantilever (Budget Sensors, Model # Multi75E-G). The resonant frequency of the tips was 75 kHz, and the radius was less than 25 nm. The interleave height was optimized to 150 nm for a good surface potential signal.

The surface potential maps of the unaged and aged $LiFePO_4$ cathode samples are shown in **Fig. 7.7**. The maps were collected by applying +1.0 V and +3.3 V from the external DC voltage source. Maps for samples without an externally applied voltage are shown for comparison. Within each surface potential map for both the unaged and aged sample, we observe no large difference in the contrast, suggesting an almost uniform dissipation of charge over the surface of the samples under the externally applied voltage. This indicates that under the external source the sample tends to charge uniformly even in an aged condition. The uniform charging is good for the cell as it avoids large local currents and subsequent damage to the cathode.

The surface potential image discussed above is generated by a matrix of 256 X 256 data points. The last column of **Fig. 7.7** also shows the distribution of these data points in unaged and aged cathodes. For each case a histogram is created with 17 equally spaced bins. The bin size was optimized using Sturgess rule [Sturges, 1926],

$$k = 1 + log_2(n) \tag{7.4}$$

where k is the number of bins, and n is total number of data points. Then a normal probability density function as shown below is used to fit the data [Bendat and Piersol, 1986].

$$f(x) = \frac{1}{\sqrt{2\pi\sigma^2}} e^{-\frac{(x-\mu)^2}{2\sigma^2}} \tag{7.5}$$

where μ is the mean, and σ is the standard deviation of the data points. The unaged sample had mean values of the surface potential almost equivalent to the external applied voltage. The mean values of surface potential on the aged sample are lower than that of the unaged sample. Thus, even though the externally applied voltage was the same for the unaged and aged samples the charge sustained on the surface of the aged cathode is less than that sustained on the unaged cathode.

The surface potential measured using KPM is the difference between the work functions of the tip and sample surface. Since the same kind of tip is used in these experiments, the work function of the tip is constant in each surface potential map. **Figure 7.7** shows the change in the work function of the aged sample as compared to the unaged sample. The work function is the property of the structure near the surface of the sample along with the chemical potential of the surface. The decreased surface potential in the aged sample is the indication of the surface modification and could occur due to one or all of the factors discussed below.

A phase change of the cathode material occurs from $LiFePO_4$ to $FePO_4$ and back to $LiFePO_4$ during respective charging and discharging cycles of the battery. During charging, the Li ions from the $LiFePO_4$ cathode are intercalated in the graphite anode.

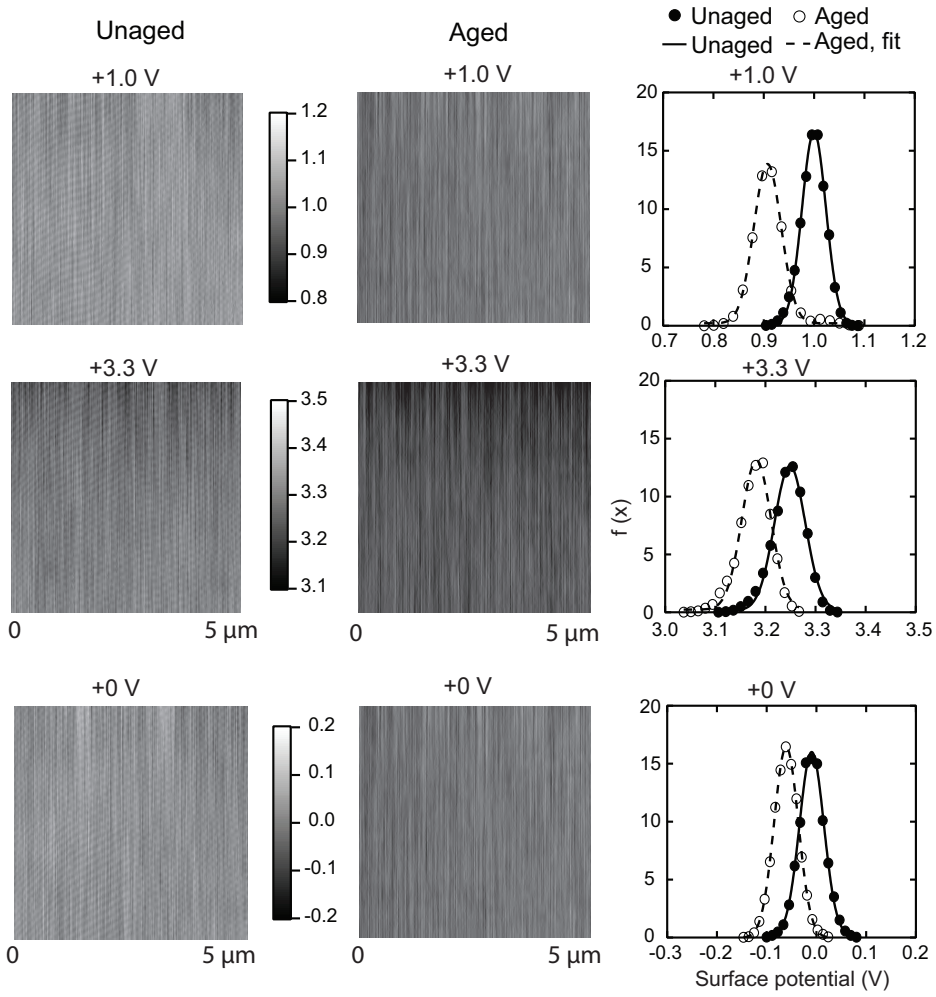

Figure 7.7: Surface potential map of the unaged (left column) and the aged (middle column) $LiFePO_4$ cathode samples with external voltage of +1.0 V and +3.3 V The data for sample without any external voltage is shown for comparison. The right column shows the normal probability density distribution of the surface potential values obtained for the unaged and aged samples. The mean value of the surface potential decreases after aging.

During discharging, the Li ions move out of the graphite anode and are intercalated back in the cathode. The olivine structured $LiFePO_4$ has a different work function that of the metastable $FePO_4$. The change in the surface potential map of the aged sample indicates that one of the phases might be growing in the cathode sample during the battery aging. Andersson and Thomas [2001] have demonstrated this phase change as a source of initial capacity loss using neutron diffraction data. Based on their experiments they have proposed a radial model and a mosaic model for the phase change between $LiFePO_4$ and $FePO_4$. In either of their models they have suggested unconverted inactive regions of $LiFePO_4$ entrapped by the $FePO_4$ phase. They concluded that, in reality the superposition of the essential features of the two models might be occurring.

7.4 Summary

The electrical properties of the $LiFePO_4$ based Li-ion batteries were studied at different scales. The capacity drop and internal resistance were used as the system level metrics. As the battery approached the EOL the knee in the discharge curve was approached rapidly. The batteries cycled at higher C-rate tend to age faster.

SSRM was used to measure the change in the surface resistance. The aged sample showed much higher surface resistance as compared to the unaged sample. The loss of performance can be attributed to the coarsening phenomena observed in the physical/morphological studies. The coarsening phenomenon can lead to the disbonding of the nanoparticles from the aluminum substrate causing loss of contact between the active material and the current collector leading to increase in the internal resistance. The coarsening can also lead to separation of particles leading to loss of

electrical contact between the particles. The coarsening phenomena can also cause the degradation in the carbon coating leading to further drop in the electrical performance of the cathode.

KPM was used to measure the change in the surface potential. The aged sample showed less charge sustaining capacity as compared to the unaged sample. The loss in the ability of the cathode to retain the applied charge can also be attributed to the coarsening phenomena. In this case, due to the larger particle size the overall distance travelled by the applied charge is increased thus leading to the loss of capability to sustain the applied charge within the applied time.

Chapter 8: Multi-scale Characterization of Cathode - Structural and Chemical

8.1 Introduction

In this chapter the chemical and structural changes in the cathode material due the aging of the batteries are examined. The long range structure of the $LiFePO_4$ nano particles is characterized with X-ray diffraction. Then Raman spectroscopy is used to characterize the carbon-coating of the cathode material. The electron energy loss spectroscopy was used to understand the changes in the local structure of the $LiFePO_4$ nanoparticles due to aging of the batteries. The electron techniques fail in characterizing the Li in the cathode material. Hence two neutron techniques are added to the scheme of the multi-scale characterization. The local lithium environment was probed with the nuclear magnetic spectroscopy. Finally, neutron depth profiling was used to measure the lithium concentration in the unaged and aged samples of the cathode material.

8.2 X-ray diffraction (XRD)

X-ray diffraction is non-destructive technique mainly used for studying long range structural ordering of materials and phase identification. It is also used for

quantitative analysis of phases, residual stress measurement, crystal structure and three-dimensional material properties. In lithium ion battery research it has been used for ex-situ phase identification of the cathode materials after being charged and discharges. Recently in-situ XRD has been demonstrated to analyze the crystalline structure of the cathode material during charging and discharging cycles [Li et al., 2003].

In this multi-scale study XRD is used to study the phases present in the aged cathode sample. **Figure 8.1** shows the XRD pattern of the unaged, aged samples. For comparison standard $LiFePO_4$ and $FePO_4$ patterns are also shown. As can be seen in the figure both the phases are present in the unaged and aged samples. This indicated that there are regions within the cathode strip, which are inactive during the charging-discharging process. A more quantitative analysis of the phases present within the samples is necessary to identify the ratios of the inactive material. The change in the volumetric concentration of the active material would be a very important input to the electrochemical and performance models of the Li-ion batteries.

8.3 Raman Spectroscopy (RS)

Raman spectroscopy is a unique analytical tool for identifying and characterizing the elements within the sample. It is a non-destructive tool and requires very minimal sample preparation. The atmospheric CO_2 and H_2O do not interfere with the Raman signal, so no special atmospheric conditions are necessary during the experiments. Several different researchers have used Raman spectroscopy to characterize different types of carbon in different forms such as crystalline, non-crystalline, amorphous carbons [Cho et al., 1990; Tamor and Vassell, 1994; Schwan et al., 1996;

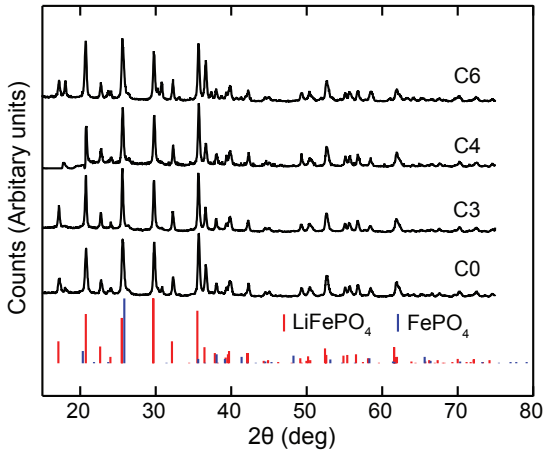

Figure 8.1: XRD spectra of unaged and aged samples. Both the samples show presence of $LiFePO_4$ and $FePO_4$ phases

Bhushan, 1999; Ferrari and Robertson, 2000]. Saito et al. [1998] have used Raman spectroscopy to analyze the single-wall carbon nanotubes.

Recently Raman spectroscopy has been used to analyze the carbon coating of $LiFePO_4$ nanoparticles used in lithium-ion batteries. The studies have been conducted to understand the effect of carbon coating on the electrochemical performance of $LiFePO_4$ based lithium-ion batteries. In the studies done by Doeff et al. [2003] they showed that the structure of the residual carbon present on the $LiFePO_4$ powder affects its electrochemical performance and the better performance is dependent on the quality of the carbon rather than the quantity of the carbon. Similarly, Cho et al. [2009] have used RS for studying the effect of the coating thickness on the capacity of $LiFePO_4$ composite cathodes. Julien et al. [2006] characterized the carbon-film coating on the $LiFePO_4$ nanoparticles and discussed the Li^+ diffusion through the

carbon coating. Wilcox et al. [2007] used RS to study the factors, in particular the synthetic additives, which can affect the quality of the carbon coatings. Also, the effects of the thermal treatments on the performance of the carbon coating using RS have been studied by Maccario et al. [2008]. RS is very useful in characterizing the carbon coating of $LiFePO_4$ nanoparticles for two main reasons. One, carbon is a strong scatterer with two E_{2g} modes predicted to be Raman active [Wilcox et al., 2007]. Second, the penetration depth of light inside the $LiFePO_4$ particles is very small, thus the first coating layer can be easily probed with RS [Julien et al., 2006].

In the multi-scale characterization plan RS is used to analyze the carbon coating on the $LiFePO_4$ nanoparticles in several commercial cells aged with different C-rate. As mentioned earlier it is a common practice in the production of lithium-ion battery electrodes to add carbon, either by use of carbon additives to the $LiFePO_4$ matrix or by surface coating of $LiFePO_4$ particles with thin layers of carbon to improve the electronic conductivity. Degradation in the quality of the carbon coating can lead to decreased electronic performance of the cathode.

Labram®, an integrated confocal Raman microscope system, made by ISA Group Horiba was used to analyze the carbon-coating. Since the positions of the Raman bands are dependent on the wavelength of the incident laser incident, a He-Ne laser with 512 nm excitation wavelength was used in these experiments for comparison of our data with the published literature. The laser power was adjusted to 2.5 mW and the laser spot size was at $\sim 5\ \mu m$. RS experiments were conducted under ambient conditions at room temperature. The data acquisition time was set at 10 s for all the samples. The commercial software package included in the Labram® system was used for background subtraction and baseline correction.

Figure 8.2 shows a typical Raman spectra obtained on sample C0 (solid dark line). The Raman spectroscopy of a disordered carbon shows two distinct peaks. The peak at $\sim$ 1600 cm^{-1} is referred to as G (graphite) peak and the peak at $\sim$ 1350 cm^{-1} is referred to as D (disordered) peak. The G peak is attributed to the optically allowed E_{2g} zone-center mode of crystalline graphite while D peak is attributed to the disorder allowed zone-edge modes of graphite [Schwan et al., 1996; Julien et al., 2006].

The Raman spectra is deconvoluted according to these two characteristic D and G peaks. As can be seen in **Fig. 8.2** the Raman spectra was satisfactorily deconvoluted with Breit-Wigner-Fano (BWF) plus Lorentzian scheme. A BWF line is used for the G peak and a Lorentzian line is used for the D peak. The BWF line shape is given by

$$I(\omega) = \frac{I_0[1 + 2(\omega - \omega_0)/Q\Gamma]^2}{1 + [2(\omega - \omega_0)/\Gamma]^2} \tag{8.1}$$

where I_0 is the peak intensity, ω_0 is the peak position, Γ is assumed as the full width at half maximum (FWHM) and Q^{-1} is the BWF coupling coefficient. Due to the coupling of a discrete mode to the continuum BWF line has an asymmetric line shape [Ferrari and Robertson, 2000; Klein, 1982]. A Lorentzian line shape given by **Eq. 8.2**, which belongs to the same family as BWF is used for the D peak:

$$L = I_0[\frac{\Gamma}{(\omega - \omega_0)^2 + \Gamma^2}] \tag{8.2}$$

The deconvolution of the Raman spectra based on BWF + Lorentzian scheme is shown for the data obtained for sample C0 in **Fig. 8.2**.

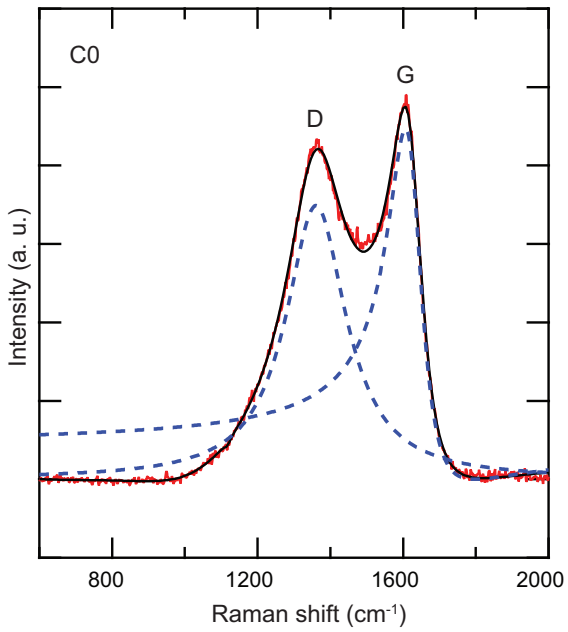

Figure 8.2: Deconvolution method used for fitting of experimental Raman spectra. The method is demonstrated with the experimental Raman spectra (dots) for C0 battery. The data is deconvoluted in two peaks (dotted line) and then fitted (solid line). The D peak is fitted wth Lorentzian and G peak is fitted with Breit-Wigner-Fano (BWF) line shape.

Figure 8.3 shows the fitted Raman spectra for all the samples using the deconvolution method described above. The deconvolution procedure satisfactorily fits the experimental Raman spectra for all the samples. The two characteristic D and G peak are observed in all the samples. Note that the positions of the Raman bands are dependent on the incident laser wavelength, so for quantitative comparison between spectra given here, the excitation wavelength of 512 nm was have maintained in this study. The data shows a uniform coating of carbon on the $LiFePO_4$ particles with highly disordered carbon. The relative intensities of the D and G band are associated with the increased carbon disorder similar to disorder in microcrystalline graphite [Vidano and Fischbach, 1978; Doeff et al., 2003].

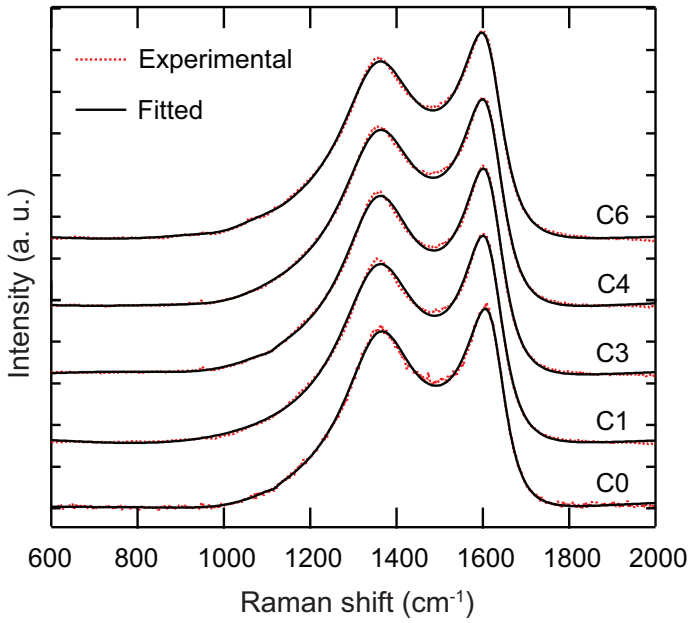

Figure 8.3: Raman spectra of all the cells. Each spectra was fitted with the deconvolution method shown in **Figure 8.2**.

According to Doeff et al. [2003] the electrochemical performance of carbon coated $LiFePO_4$ cathode is not only dependent on the quantity of the carbon but also on the quality of carbon. The quality of the carbon coating in the different samples is compared by comparing the intensity ratios of D and G band (I_D/I_G). Usually a lower I_D/I_G ratios are desired in a good quality $LiFePO_4$ cathode. As can be seen in **Figure 8.4**, I_D/I_G ratio increases with increasing C-rate. According to Tuinstra and Koenig [1970]the in-plane correlation length I_D/I_G is related to the I_D/I_G ratio, which quantifies the mean basal-plane diameter of graphite parallel to (001) [Maccario et al., 2008]. The following modified Tuinstra-Koenig relation gives the value of L_a,

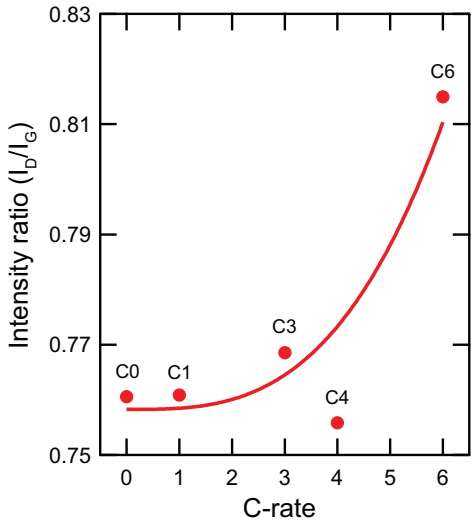

Figure 8.4: Intensity ratio analyses (I_D/I_G). The intensity is calculated as the area under the respective curve. The intensity increases with the C-rate indicating poor quality of carbon leading to loss of electrical conductivity in batteries cycled at higher C-rate.

$$L_a = \frac{C(\lambda_L)}{I_D/I_G} \tag{8.3}$$

where $C(\lambda_L)$ is a variable scaling coefficient depending on excitation wavelength λ_L and given by

$$C(\lambda_L) = C_0 + \lambda_L C_1 \tag{8.4}$$

where $C_0 = -126$ Åand $C_0 = 0.033$ [Matthews et al., 1999]. As the I_D/I_G ratio increases from 0.76 to 0.81 the in-plane correlation length I_D/I_G calculated using **Eq. 8.3** and **Eq. 8.4**, drops from 5.64 to 5.27 nm for cells C0 through C6. The increasing trend of the ratio and decreasing trend of the in-plane correlation length suggest the lower amounts of graphite clusters in very highly disordered carbon. Thus higher I_D/I_G ratio here indicates poor quality carbon in cells aged with higher C-rate [Wilcox et al., 2007]. This leads to poor electronic properties of the carbon coating and contributes to the increased ohmic resistance of the cell. Thus the overall electrode performance is affected in cells aged with higher C-rate. The composite cathode cycled with higher C-rate have poor electronic conductivity.

In summary RS was used to analyze the carbon coating of aged $LiFePO_4$ nanoparticles. According to the Raman studies the carbon coating degrades in quality as the batteries are aged at higher C-rates. The higher I_D/I_G ratio in case on batteries cycled at higher C-rate indicate poor quality of carbon leading to loss of electrical conductivity and subsequent decrease in the performance of the battery.

8.4 Electron energy loss spectroscopy (EELS) (nm)

Electron energy loss spectrometry (EELS) is based on the analysis of the energy distribution of electrons that have interacted inelastically with the specimen. These inelastic collisions carry information about the electronic structure of the specimen, which help in understanding the electronic bonding between the various elements of the specimen. The EELS studies can also help in identifying the thickness of the sample. The technique can be applied to any amorphous as well as crystalline samples. The EELS spectrum is gathered with a help of a magnetic prism spectrometer which is often interfaced into TEM [Williams and Carter, 2004].

So far, in lithium ion battery research, EELS has been used to study the local electron structure of the host material, intercalation/deintercalation process of the Li within the host material and the subsequent phase changes [Miao et al., 2007; Laffont et al., 2006]. In the multi-scale characterization plan EELS is included to analyze the local electronic bonding of the Li with its neighboring atoms and identify the changes in these electronic bonding schemes between the $LiFePO_4$ cathode samples harvested from the unaged and aged batteries. Such studies were conducted along with the high-resolution TEM imaging studies reported in **Section 6.6** by Nagpure et al. [2011c]. The sample preparation process has already been discussed in the **Section 6.6**.

Figure 8.5 shows the microstructure and the corresponding EELS measured for the unaged and aged samples. The areas were chosen for a single particle analysis. Due to the uncertainty in establishing the absolute value for the energy loss scale all the spectra were aligned at O K edge (532 eV). All the spectra were normalized to the intensity of the O K edge peak. As shown in **Fig. 8.5b**, a significant difference

in the shape of the O K edge peak is observed. The peaks in the data were fitted with a Gaussian function. The O K edge peak is at 532 eV, with a pre-peak at $\sim$ 528 eV found in the aged sample which is almost negligible in the unaged sample. **Figure 8.5c** shows changes in the Fe $L_{2,3}$ edge with aging. It can be seen in this figure that the main difference between the aged and unaged sample is the position of the Fe $L_{2,3}$ edge. The onset of the Fe $L_{2,3}$ edge for the aged sample is $\sim$ 2 eV higher than for the unaged sample. The EELS measurements were conducted from the periphery to the core of the $LiFePO_4$ particle in both, the unaged and aged sample, but note that in **Fig. 8.5b and c** not all spectra are shown, and only a representative of the phenomena is presented. As can be seen in **Fig. 8.5b**, the intensity of the O K edge pre-peak is higher at the core than at the periphery of the large particle in the aged sample. Thus the ratio of the pre-peak to the main feature of O K edge peak was less at the core of the larger particle in the aged sample than at the periphery. It is also interesting to note that if the EELS spectra are obtained at the core and the periphery of a large particle in the aged sample there is a shift of Fe $L_{2,3}$ edge to a higher energy.

The differences in the shape of the O K edge and the position of the Fe $L_{2,3}$ edge have been explained in previous spectroscopy work by Laffont et al. [2006] and Miao et al. [2007]. The pre-peak at the O K edge and the shift to higher energy of Fe $L_{2,3}$ edge observed in the aged sample is characteristic of a highly delithiated $LiFePO_4$ (a charged cell), while the spectra observed in the unaged sample is characteristic of a well lithiated $LiFePO_4$ (a discharged cell). Since in this study both samples were discharged before disassembly, it is believed the phenomena observed here is due to the aging of the cells. The measurements suggest that the core of

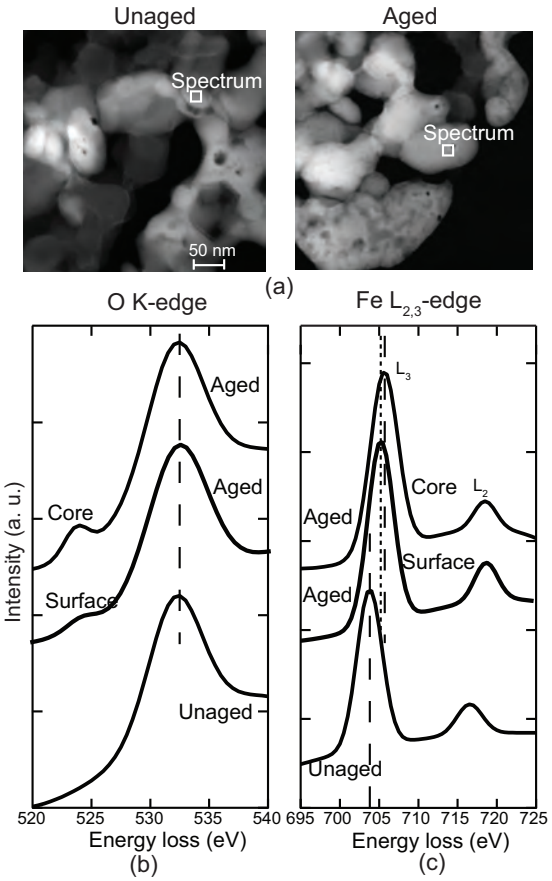

Figure 8.5: (a) TEM images of unaged and aged $LiFePO_4$ cathode samples showing the location of EELS spectrum (b) and (c). (b) O K edge of the unaged and aged $LiFePO_4$ cathode samples. There exists a pre-peak in the case of the aged sample suggesting a change in the density of states of O. (c) Fe $L_{2,3}$ edge of the unaged and aged $LiFePO_4$ cathode samples. The edges shift to the right in case of the aged sample. The EELS data was normalized with the O $L_{2,3}$ edge peak. The individual spectra were offset vertically in order to present the details

the larger, coarsened $LiFePO_4$ particle in the aged sample has a different lithium composition than the periphery. It is thus believed that during aging the $LiFePO_4$ nanoparticles sinter together resulting in coarsening of the particles. This coarsening is expected to increase the Li-ion diffusion length through the particles, and thus the transformation of nanoparticles during discharging of the cell from $FePO_4$ back to $LiFePO_4$ is expected to be incomplete, leaving a $FePO_4$ (or low Li-concentration) core and a $LiFePO_4$ shell around the core in large particles. As the cell ages the $FePO_4$ (or low Li concentration) core increases and the $LiFePO_4$ shell decreases. This leads to the conclusion that the aging has caused significant compositional changes in the $LiFePO_4$ nanoparticles. The active lithium is lost from the host cathode material, thus reducing its capacity. The diminished levels of Li in the cathode can be expected to lead to a compromised capability of the overall cell to recharge.

The electronic structure calculations were performed on supercells containing six formula units of Li_xFePO_4 with x = 0, 0.25, 0.5, 0.75, and 1 for detailed analysis and interpretation of the experimental results. The structural data for the starting materials in these calculations were adapted from Tang and Holzwarth [2003]. $LiFePO_4$ forms an orthorhombic olivine structure with a slightly distorted hexagonal close packed oxygen array belonging to the symmetry group Pnma [Islam et al., 2005], listed as no. 62 in the *International Tables for Crystallography* [Hahn, 2002]. **Figure 8.6** shows the crystal structure of this material with one unit cell constructed with Materials Studio™. The O atoms are located at the tetrahedral sites around each P atom. The divalent Fe ions form an octahedral arrangement with the O atoms. The Li atoms are located in channels along the b axis of the orthorhombic structure [Tang and Holzwarth, 2003].

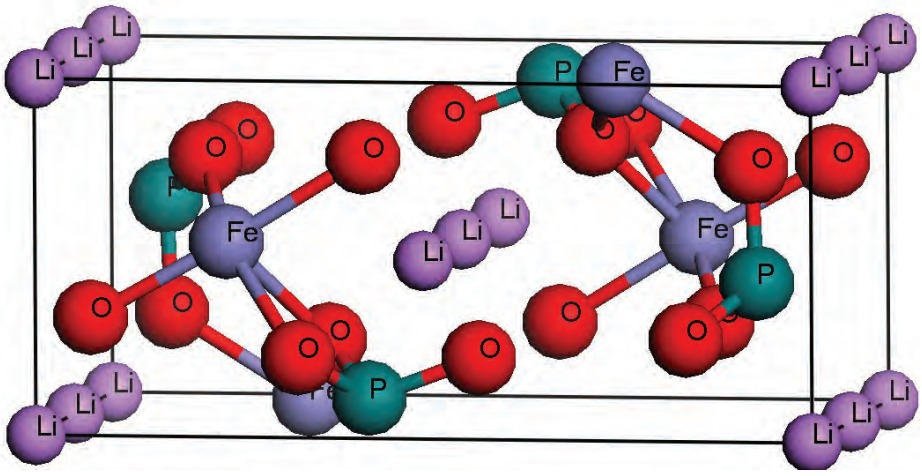

Figure 8.6: Crystal structure of $LiFePO_4$ showing one unit cell constructed with Materials Studio™

Density functional theory (DFT), as implemented in the Vienna Ab-initio Simulation Package (VASP) [Kresse and Furthmüller, 1996a,b] was employed to perform the electronic structure calculations within the generalized gradient approximation (GGA) with PW91 [Perdew et al., 1992] type projector augmented wave (PAW) potentials using a cutoff energy of 500 eV, enhanced by a coulombic term U [Anisimov et al., 1991] to include strong correlation effects (GGA + U) for the Fe d orbitals. Within this framework the exchange term J is combined with the coulomb term U and $(U - J)$, an effective value of U referred to as U_{eff}, is used. A value of 4.3 eV was chosen for U_{eff}, following Miao et al. [2007]. All the calculations here have been performed for the ferro-magnetic configuration for consistency. An energy convergence 10^{-6} of better than eV was achieved when relaxing the geometry. The initial and relaxed lattice parameters for structures with varying lithium contents calculated with the GGA + U approximation are shown in **Table 8.1**.

Table 8.1: Initial lattice parameters and relaxed lattice parameters for structures with varying lithium content obtained by generalized gradient approximation (GGA) with PW91 type of pseudopotentials, enhanced by a U term to include strong correlation effects (GGA+U). The structural co-ordinates were adapted from [Tang and Holzwarth, 2003] for $FePO_4$ and $LiFePO_4$, while the intermediate structures were created by subsequently removing lithium from $LiFePO_4$ structure.

Compound	a lattice(Å)		b lattice (Å)		c lattice (Å)	
	Initial	Relaxed	Initial	Relaxed	Initial	Relaxed
$FePO_4$	9.81	9.946	5.79	5.891	4.78	4.866
$Li_{0.25}FePO_4$	10.33	10.041	6.008	5.947	4.69	4.861
$Li_{0.5}FePO_4$	10.33	10.203	6.008	5.993	4.69	4.806
$Li_{0.75}FePO_4$	10.33	10.324	6.008	6.026	4.69	4.787
$LiFePO_4$	10.33	10.418	6.008	6.067	4.69	4.745

Following Duscher et al. [2001], the Z + 1 approximation method has been applied to simulate the electron energy loss near edge structure (ELNES). The ELNES onset was set up at the Fermi energy of the different structures. This approximation has been shown to model core hole excitation spectra in oxides well if dipole selection rules are used (change in orbital angular momentum quantum number by one) [Duscher et al., 2001; Windl et al., 2004]. Integration for the angular momentum resolved conduction band density of states (DOS) has been performed using the tetrahedron method with Blöchl corrections for 6 formula unit supercells created from the geometrically relaxed unit cells, with a $4 \times 4 \times 4$ Monkhorst-Pack k-point mesh for Brillouin zone sampling for the supercells [Monkhorst and Pack, 1976].

Figure 8.7 shows ELNES for the O K edge and Fe $L_{2,3}$ edge obtained by the first-principles calculations. A small pre-peak for the O K edge is found for $FePO_4$,

which is not found in structures with Li_xFePO_4 ($x > 0$). This is in agreement with the observed experimental trend presented in **Fig. 8.5b**. For the Fe $L_{2,3}$ edge (**Fig. 8.7b**) a peak shift towards higher energies can be observed with decreasing lithium content, which has also been observed in the experimental results (**Fig. 8.5c**). For $FePO_4$ with no lithium the calculated EELS shows a reverse shift in the Fe $L_{2,3}$ edge, in agreement with Miao et al. [2007], which the band structure calculations suggest could potentially be due to the fact that Li acts as a donor in $FePO_4$, causing a shift in the Fermi level.

Figure 8.8 shows O p states, Fe d states, and P s and p states and their hybridization based on band structure calculations. In a perfectly ionic state the O ions in $FePO_4$ could be expected to have a valence of 2 with fully filled $2p$ states. . Covalent bonding, however, leads to hybridization between the Fe $3d$, O $2p$, and P $3s$ and $3p$ states, giving rise to empty states (above the Fermi level) with some O $2p$ states. This can be seen from **Fig. 8.8**, where the atom resolved DOS, obtained from first-principles calculations, has been plotted for three compositions: $FePO_4$, $Li_{0.5}FePO_4$, and $LiFePO_4$. In all three compounds the valence band just below the Fermi level (region 1 in **Fig. 8.8**) has major contributions from the O $2p$ states with some Fe $3d$ states. The conduction band just above the Fermi level (region 2 in **Fig. 8.8**), on the other hand, is dominated by Fe $3d$ states with small contributions from O $2p$ states. Moving to higher energy bands ($>$ 10 eV, region 3 in **Fig. 8.8**, antibonding states are found with O $2p$, $3s$, and $3p$ states. In $FePO_4$ the contribution of O $2p$ states in region 2 is significant and gives rise to the pre-peak A observed in the simulated O K edge EELS spectra, shown in **Fig. 8.7a**, due to transitions from the $1s$ core orbital of oxygen. The O $2p$ states present in region 3 gives rise to peaks

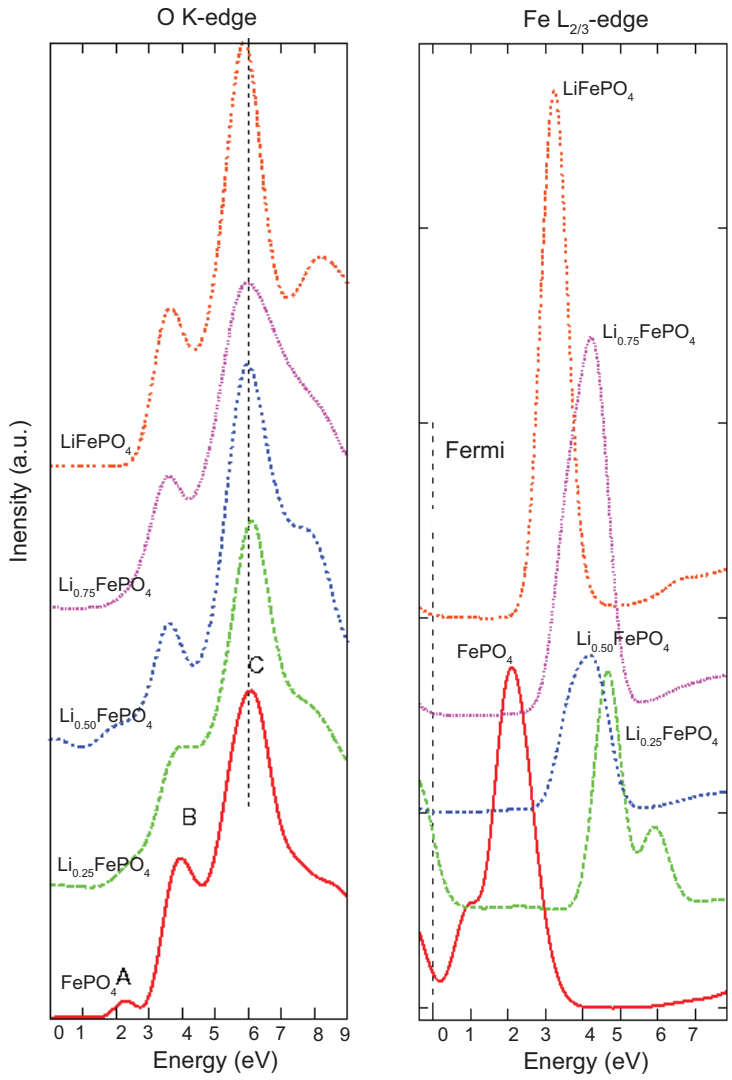

Figure 8.7: (a) The O K edge electron energy loss near edge structure (ELNES) calculated within the Z+1 approximation and dipole selection rules using the Vienna ab-initio simulation package (VASP). (b) Analogous calculation of the Fe $L_{2,3}$ edge ELNES. The energies are set at the Fermi energy, which is 0 eV on the x-axis. The ELNES intensities were normalized to the O K edge peak. The individual spectra were offset vertically in order to present the details.

B and C seen in **Fig. 8.7a**, after core hole corrections which shift these states towards lower energies by approximately 3 eV.

While Li addition does not affect the positions of peaks B and C, it does lead to a continuous decrease in the intensity of pre-peak A, as observed in both the experimental (**Fig. 8.5b**) and simulated (**Fig. 8.7a**) O K edge EELS spectra. This can be attributed to the following two causes. Firstly, on addition of Li the Fe $3d$ states shift to higher energies (from $\sim 3-5$ eV in $FePO_4$ to $\sim 6-8$ eV in $LiFePO_4$) because of the reduction in the oxidation state of Fe from Fe^{3+} to Fe^{2+} (region 2 in **Fig. 8.8**). Secondly, it leads to a continuous decrease in the extent of hybridization between Fe $3d$ and O $2p$ states, such that the contribution of O $2p$ states in region 2 becomes negligible in $LiFePO_4$. This analysis is similar to the arguments put forward by Kinyanjui et al. [2010], who studied only the end compounds. Based on the decrease in intensity of pre-peak A with Li addition, the pre-peak is expected to be completely absent for Li concentrations greater than ~ 75 %. Similarly, in the case of Fe L edges the intensities of the sharp lines themselves scale with the number of unoccupied $3d$ states of the Fe atom. In the aged sample the shift is ~ 2 eV. According to the first principles simulations presented this would correspond to a reduction in Li content of ~ 80 %. Thus, the $FePO_4$ core and $LiFePO_4$ shell, co-exist within large particles, and as the cell ages the $FePO_4$ (low Li content) core expands while the $LiFePO_4$ shell decreases.

The energy at the Fe $L_{2,3}$ edge peak obtained from first-principles calculations was plotted against the Li concentration in Li_xFePO_4 in **Fig. 8.9**. The shift to higher energy in the location of the Fe $L_{2,3}$ edge peak follows a linear trend with an approximate slope of -1.9 eV with increasing Li concentration. Considering the

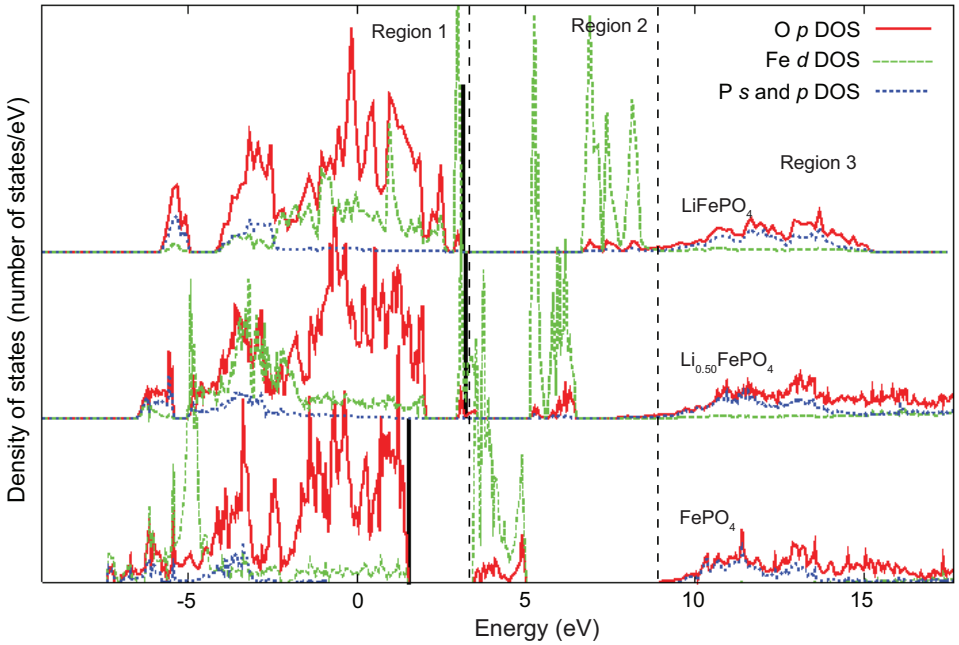

Figure 8.8: O p states Fe d states, and P s and p states and their hybridization showing how the states move with Li concentration and thus give rise to variations in the intensity of O K edge pre-peak. The black line is the Fermi level given by Vienna Ab-initio Simulation Package (VASP).

experimental shift of $\sim$ 2 eV between the unaged and aged samples, this would indicate a Li loss of $\sim$ 80 % in the aged sample. Since complete Li depletion from $LiFePO_4$ would lead to a downward rather than the observed upward peak shift, the calculation here indicates that the aged sample is not completely Li depleted, but rather remains at a low Li content of $\sim$ 20 %.

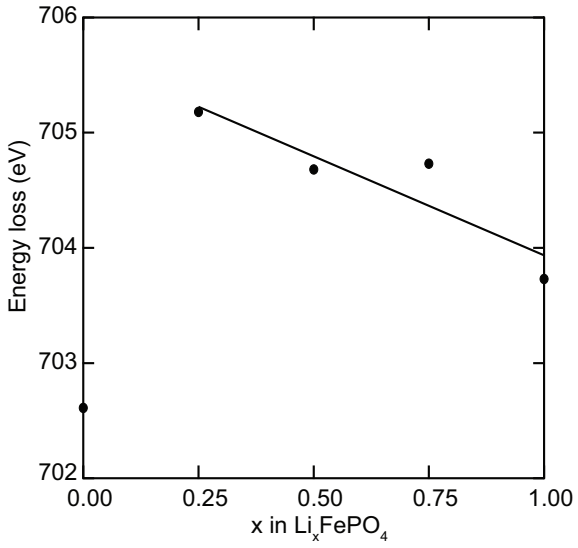

Figure 8.9: Calculated energy at the Fe $L_{2,3}$ edge peak vs. Li concentration in Li_xFePO_4. The data fits a straight line with slope -1.9 eV. Based on this plot it is estimated that the aged sample was $Li_{0.2}FePO_4$.

To summarize, EELS measurement showed that the density of states for O changes as the cell ages. This was evident in the presence of the pre-peak in the case of the O K edge. The increase in the ratio of the pre-peak to the O K edge peak in the EELS data from the core to the surface of the large $LiFePO_4$ particle indicates different lithium composition within the particle. There is also a shift of almost 2 eV for the $L_{2,3}$ edge of Fe in the aged sample. At a certain age of the cell

the particles start to coarsen. The ion diffusion length is expected to increase in the coarser particle, and this is expected to lead to an incomplete transformation between $LiFePO_4$ and $FePO_4$ while charging and discharging. The $FePO_4$ core is expected to expand in subsequent cycles, thus reducing the capacity of the host cathode material.

The experimental results were analyzed with the help of simulated ELNES spectra for the olivine structure (space group Pnma) of Li_xFePO_4 with x = 0, 0.25, 0.5, 0.75, and 1. The nature of the O pre-peak was confirmed by comparing the position of the O $2p$ bands arising due to strong hybridization among the O p states, Fe d states, and P s and p states with the Fermi level position. The Li loss was quantified by these calculations as 80 %, suggesting a strongly Li depleted, but not completely Li free, core region in the coarsened particles.

8.5 Nuclear Magnetic Resonance (NMR)

In lithium-ion batteries Li is the most important element as it is directly involved in the electrochemical process during the charging and discharging cycles of batteries. As such understanding the Li concentration as well as the local crystallographic and electronic structure of Li within the host $LiFePO_4$ structure is critical to predict the performance of the lithium-ion batteries in terms of operating voltage, residual capacity, and rate capability. The common electron spectroscopy techniques fail to identify and characterize lithium within the sample. The energy dispersive spectroscopy (EDS) technique, which is commonly used to identify the atomic percent of the elements in the component, fails to detect Li. The EDS detectors are very sensitive to impurities. To avoid repeated exposure of the detectors to atmosphere, they are maintained under vacuum and are separated from the column vacuum in the

electron microscope by beryllium window. The thin beryllium window on the EDS detector absorbs low energy X-rays and thus prevents the use of EDS in the detection of elements with an atomic number less than five. EELS provides an indirect method to probe the lithium and its local environment within the sample. The EELS study have showed the change in the density of states of O in the aged $LiFePO_4$ cathode sample and the subsequent loss of Li from the host $LiFePO_4$ structure. XRD techniques are useful in identifying the phases of the $LiFePO_4$ material present in the cathode and long-range structural data. However, it lacks the ability to provide local crystallographic and electronic structure of lithium within the sample.

As such neutron based techniques such as neutron imaging, neutron depth profiling (NDP) or NMR etc prove very vital in studying lithium within the sample as neutrons have high penetration power and detectors does not require any special protection from environment [Goers et al., 2004; Siegel et al., 2011]. Among all these neutron techniques, NMR can play a vital complementary role to study cathode materials in lithium-ion batteries as it directly probes the local Li environment [Grey and Lee, 2003].

Solid state NMR is extremely useful for studying the local structure in ordered and disordered materials. Solid state Li NMR in particular is very useful due to its high sensitivity towards the atomic and electronic environment at the lithium site within the host cathode structure [Tucker et al., 2002a]. NMR can distinguish between the metallic and semiconductor behavior of the materials. While probing the local and electronic environment of the nuclear probe it can also monitor the electronic structure of the surrounding cations [Grey and Lee, 2003]. In NMR spectroscopy it is also possible to quantify the species taking part in battery charging and discharging

and monitor the effect on the local structural changes of these species as the function of the aging of the battery. Due to its sensitivity towards the local electronic structure it can also distinguish between diamagnetic and paramagnetic behavior of materials. Most of the materials used as cathode in lithium-ion batteries show paramagnetic behavior in charged and discharged state [Grey and Dupre, 2004].

The natural abundant ^{7}Li isotope (93 %) has larger quadrupolar and gyromagnetic moments as compared to the less abundant ^{6}Li (7 %) isotope. The quadrupolar interactions result from the interactions between the quadrupolar nucleus and the electric field gradient at the nucleus. The quadrupolar interactions of ^{6}Li are smaller compared with ^{7}Li but they result in higher resolution spectrum that is easier to interpret Grey and Dupre [2004]. Thus the coupling between the lithium nucleus and the unpaired electrons can be exploited in magic angle spinning (MAS) NMR to study the changes in the local electronic structures as the function of the battery aging in the paramagnetic cathode materials.

Given these advantages of NMR it has been used by several researchers to study different types of cathode materials. Layered oxides such as $LiCoO_2$, $LiNiO_2$ have been studied by Dahn et al. [1990], Marichal et al. [1995], Levasseur et al. [2000], and Carlier et al. [2001a,b]. The spinel structured materials such as $LiMn_2O_4$ have been studied by Gee et al. [1998], Lee et al. [1998, 2000], Lee and Grey [2000], Morgan et al. [1994], Tucker et al. [2000], and Verhoeven et al. [2001]. The spinel structured materials such as $LiFePO_4$ have also been studied by Gaubicher et al. [2000], Arrabito et al. [2001], and Tucker et al. [2000, 2002a,b]. The goal in these studies has been to understand and predict the effect of local and electronic structure on lithium NMR shift in these battery materials. In-situ NMR studies using toroid

detector with limited resolution have also been conducted by Gerald et al. [2001]. Chevallier et al. [2003] have also shown that NMR signals from plastic bag batteries can be successfully obtained for analysis.

In the multi-scale characterization plan magic angle spinning (MAS) nuclear magnetic resonance (NMR) with ^{7}Li probe is used to probe the presence of lithium in the unaged and aged cells. As Li is vital in charging and discharging of the batteries NMR can provide vital understanding about its local environment within the host structure and any changes to the structure due to aging during cycling of the cells.

Bruker DSX^{TM} 300 MHz NMR spectrometer was used to probe the lithium in $LiFePO_4$ nanoparticles. A 7 mm triple resonance MAS probe was tuned to ^{7}Li frequency of 38.9 MHz. The shifts in the^{7}Li were referenced with 1 M LiCl(aq) solution. The Bloch Decay experiment method was used with relaxation delay of 10 s and spin rate of 10 kHz.

Figure 8.10 shows the NMR spectra for C0 and C6 samples. In case of the C0 sample a single isotropic ^{7}Li peak is observed while this peak is absent in case of C6 sample. The NMR spectra of C0 shows a small chemical shift of $\sim$ 8 ppm. There is also considerable broadening of the peak. The multiple spinning side bands accompanying the isotropic peak observed by Tucker et al. [2002a,b] are not observed in this case. The single isotropic band indicates one local environment for the lithium in case of C0. The crystal structure of the $LiFePO_4$ was shown in **Fig. 8.6** and discussed in **Section 8.4**. $LiFePO_4$ shows a paramagnetic behavior and the single isotropic peak in C0 is as expected for paramagnetic materials containing a single type of Li site. Lithium NMR spectra for paramagnetic materials are dominated by series of larger interactions such as quadrupole coupling (^{6}Li, I = 1; ^{7}Li, I = 3/2) and

hyperfine interactions between nucleus and the unpaired electrons [Grey and Dupre, 2004]. The possibility of a Knight shift in the battery materials is excluded due to their electronic insulating character [Tucker et al., 2002b].

According to Tucker et al. [2002a,b] the shift in case of $LiFePO_4$ can be attributed to the hyperfine interactions through-bond transfer (specifically Li-Fe-O bond) of unpaired electron density via the oxygen p-orbitals to the Li s-orbitals. Since $LiFePO_4$ is electronically less conductive the Knight shift characteristic of metal conductors is ignored for this material. The broadening of the peak can be attributed to the considerable local disorder in the coordination sphere of Li in $LiFePO_4$ [Tucker et al., 2002a]. The absence of peak in case of C6 samples indicates presence of $FePO_4$ instead of $LiFePO_4$ phase. This is consistent with observation by [Nagpure et al., 2011c], using EELNS. The Li depletion in case of aged samples caused the changes in the local electronic structure of the sample. The Li depletion in aged sample caused the transitions from the $1s$ core orbital of oxygen and strong hybridization between the Fe $3d$, O $2p$, and P $3s$ and $3p$ states, giving rise to empty states (above the Fermi level) with some O $2p$ states. The lithium starved $FePO_4$ phase indicates loss of cycling capability of the battery.

In summary NMR was used to probe the local Li environment of the $LiFePO_4$ nanoparticles. The solid state ^{7}Li NMR is very critical in studying the local environment and electronic structure of the $LiFePO_4$ nanoparticles as it directly probes the Li within the sample. An isotropic peak with small chemical shift, a characteristic of paramagnetic materials, is observed in unaged $LiFePO_4$ sample. The absence of such peak in the aged sample indicates the Li starved $FePO_4$ phase. The loss of active Li directly affects the loss of cycling capacity of the battery.

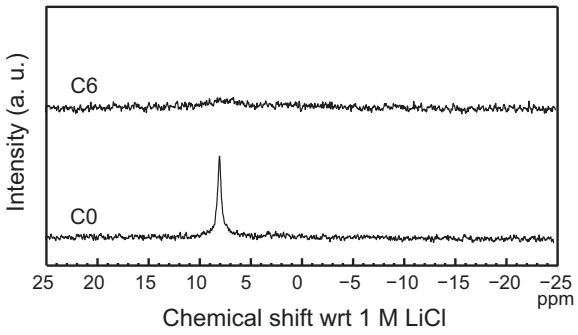

Figure 8.10: NMR spectra of samples harvested from C0 and C6 batteries. An isotropic ^{7}Li peak is observed in C0 while similar speak is absent in C6

8.6 Neutron depth profiling (NDP)

So far, the degradation of the $LiFePO_4$ cathode has been studied by various techniques. AFM has been used for physical/morphological studies along with CSAFM, SSRM and KPM for analysis of surface electrical properties [Nagpure et al., 2009, 2011a]. Spectroscopy techniques such as EELS has been used to conduct the structural analysis of the cathode material. Electron microscopic techniques have been used to analyze phase change, structural changes, etc. These techniques deliver some useful information about the changes in the cathode, but they fail to address the issue of lithium transport or lithium concentration within the cathode.

NDP is a very useful technique in studying the concentration of lithium within the sample. It is a non-destructive analytical technique based on the nuclear fission reaction between beam of neutrons with certain elements, such as lithium, throughout the sample. The cold neutrons are delivered through a neutron guide to the NDP chamber. In this work, the cold neutrons refer to neutrons with energy less than

5 meV. Since cold neutrons have extremely low energy and momentum, there is no center-of-mass motion in the neutron-lithium reaction. Furthermore, the neutron event rate is insufficient to cause significant temperature rise in the sample nor is there significant radiation damage to the sample during the measurement period.

Ziegler et al. [1972] for first time used the nuclear reaction experiment to determine the concentration of boron impurity in silicon wafers. The sample was bombarded with a well-collimated beam of low energy neutrons in vacuum, and the emitted energized particles were analyzed using a charged-particle spectroscopy for the concentration profile of the ^{10}B in the sample. Later, Downing et al. [1983] coined the term neutron depth profiling (NDP) for this technique. Since then there have been several applications of this technique to other neutron sensitive light-weight isotopes, some of which are listed by Downing et al. [1993]. Biersack and Fink [1975] were first to study the implantation of lithium in semiconductors using NDP. Later on Krings et al. [1999] studied lithium diffusion in electrochromic WO_3 films using NDP. They compared the secondary ion mass spectrometry (SIMS), elastic recoil detection (ERD), and NDP techniques while profiling the lithium concentration along the depth of lithium intercalated thin electrochromic WO_3 films. They concluded that the NDP technique has a very good depth resolution with high sensitivity and proves to be very useful over the other techniques because of its non-destructiveness. Lamaze et al. [2003] have demonstrated the use of NDP in two thin film battery materials. They profiled the lithium concentration in ion beam assisted deposition (IBAD) thin lithium phosphorus oxynitride films and thin lithium cobalt oxide films. The main advantage was again the non-destructive nature of the NDP technique. The study

was limited to the deposited thin films rather than electrodes extracted from actual lithium ion cell.

Whitney et al. [2009] used NDP to profile the lithium concentration in a cathode of the Li-ion lab cells and an anode of the off-the-shelf Li-ion cells. The lithium transportation was studied for storage of cells at different temperatures and cycling of the cells at different rates. They demonstrated a method to determine the thickness of the solid electrolyte interface on a graphite anode in a $LiFePO_4$ cell when stored for different lengths of time under different temperatures. They also profiled the lithium concentration in $LiFePO_4$ and $LiNi_{1/3}Mn_{1/3}Co_{1/3}O_2$ cathodes after cycling for only 100 cycles. This helped to understand the lithium distribution in initial cycles but did not address the issue of lithium transportation during the end of life of the cells.

The NDP technique was included in the multi-scale characterization plan for detailed analysis of the lithium concentration in the commercial cells. The effect of C-rate on the lithium concentration towards the EOL of the battery was measured. All NDP experiments discussed here were conducted at the NIST Center for Neutron Research (NCNR). A schematic of the NDP facility is shown in **Fig. 8.11**. The sample is attached to an aluminum disk (**Fig. 8.11**) which is held vertically at the center of a vacuum chamber by the grooves provided on the sample mount. The sample mount is oriented such that the sample faces the surface-barrier type charged particle detector. The detector has an active area of 150 mm^2 and is placed slightly more than 10 cm from the neutron beam-spot on the sample. A $\sim$0.8 cm^2 area of the sample is illuminated by the cold neutron beam entering the vacuum chamber. Upon the absorption of the neutron by the elemental atom in the sample, monoenergetically charged alpha and triton particles are emitted and travel diametrically opposite from

the site of the reaction. More specifically, when the neutron reacts with the ^{6}Li atom in this sample, monoenergetically charged alpha (^{4}He) and triton (^{3}H) particles are emitted are shown in the reaction below,

$$^6\mathrm{Li} + \mathrm{n} \longrightarrow {}^4\mathrm{He}(2055keV) + {}^3\mathrm{H}(2727keV) \tag{8.5}$$

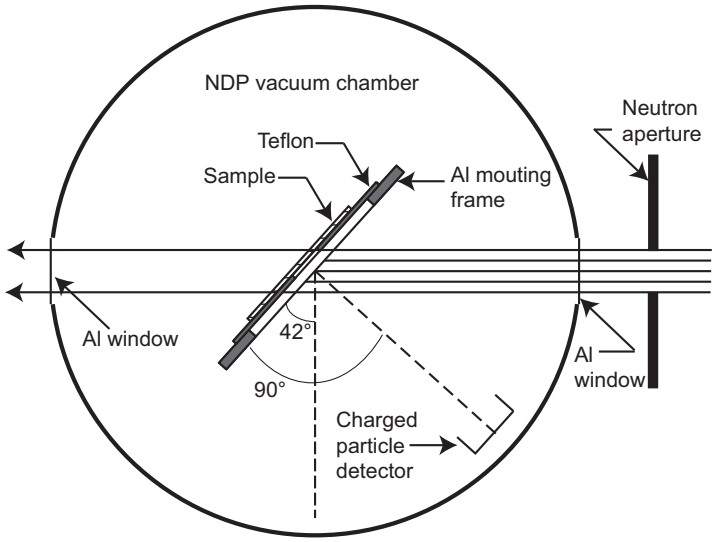

Figure 8.11: A schematic layout of the cold neutron depth profiling chamber at NIST (adapted from [Tun et al., 2010]). At the center of the chamber the sample is mounted using a 21 cm diameter aluminum ring shaped disk concentrically covered with a thick dielectric sheet. The dielectric has a 1 cm dia. hole at the center of the disk which serves as the defining window for charged particles exiting from the sample in the direction of the detector

The energy of the ^{4}He and ^{3}H particles at the reaction site is known to be at 2055 keV and 2727 keV, respectively [Downing et al., 1993]. These heavy charged particles lose energy via a stochastic collision with electrons along the path traveling outwards. Both, the count rate and the residual energy are simultaneously measured

from all depths for the particle species emerging in the direction of the detector (**Fig. 8.11**). The charged particles do not lose any energy after leaving the surface of the sample traveling to the detectors, since the sample chamber is maintained at a vacuum less than 1.33 mPa (10^{-6} Torr). Calibration performed prior to the experiment determined the full width half maximum (FWHM) energy resolution of 18 keV for the charged particle detector. The samples were exposed to the neutron beam for various time lengths ranging between 3 to 4 hours. The exposure time was not fixed so the data was normalized with respect to the run time, but the samples were exposed long enough so that the statistical error in counting of the ^{4}He or ^{3}H particles is no higher than 3 %.

The reaction center of mass is coincident with the site of the lithium atom. Thus the ^{4}He and triton ^{3}H particles originate from the same location as that of the original lithium atom, and their respective energies are directly related to the location of the lithium atom in the sample. The energy loss of the charged particle per unit length traveled through the sample is given by the stopping power function of the sample. Mathematically, to the first-order approximation, the depth is related to the stopping power by Braggs law given as

$$x = \int_{E(x)}^{E_o} \frac{dE}{S(E)} \tag{8.6}$$

Here x is the path length traveled by the particle through the material, E_o is the initial energy of the particle, $E(x)$ is the energy of the particle emerging from the surface, and $S(E)$ is the stopping power of the sample material [Ziegler et al., 1972]. The Stopping and Range of Ions in Matter (SRIM) code developed by Ziegler et al. [2008] is then used to obtain the stopping power of the $LiFePO_4$ cathode and

the graphite anode and assign the residual energies of the charged particle to the corresponding depth in the sample. The concentration of ^{6}Li within the sample is determined by comparing the count rate observed from the sample with that of a well characterized boron concentration standard, labeled as N6 [Gilliam et al., 1993]. Since the natural abundance of ^{6}Li in the sample is only 7.5 %, the total Li elemental concentration is obtained by dividing the determined ^{6}Li concentration by 0.075.

The energy spectrum of the 2727 keV ^{3}H particle is used here because of its two advantages over the corresponding energy spectrum of the 2055 keV ^{4}He particle. First, since the ^{3}H particle has higher energy and less mass, the concentration profiles can be obtained to greater depth in the sample. Second, ^{3}H energy spectrum is not overlapped by the ^{4}He energy spectrum, but the ^{4}He energy spectrum is interfered with by the ^{3}H energy spectrum at low energies, i.e., by the charged particles generated from deeper below the sample surface.

Figure 8.12 shows the lithium concentration profile in the anode and cathode of the various cells aged with different C-rates. The lithium profile obtained from cell C0 is established as the baseline for comparison. In the left column the lithium concentration profiles of the anode can be seen changing from section # 1 to section # 5 at the same C-rate. The surface concentration increases across the different cells with the C-rate. The right column shows the lithium concentration profile in the cathode. The profiles remain identical from sections 1 to 5 at the same C-rate, but the slope of the profile decreases with increasing C-rate.

Figure 8.13 shows the effect of the SOC combined with the C-rate on the lithium concentration profile. **Fig. 8.13a** shows the lithium concentration profile in the cell cycled between 60 and 70 % SOC with ∼6 C-rate (C6) for sections #

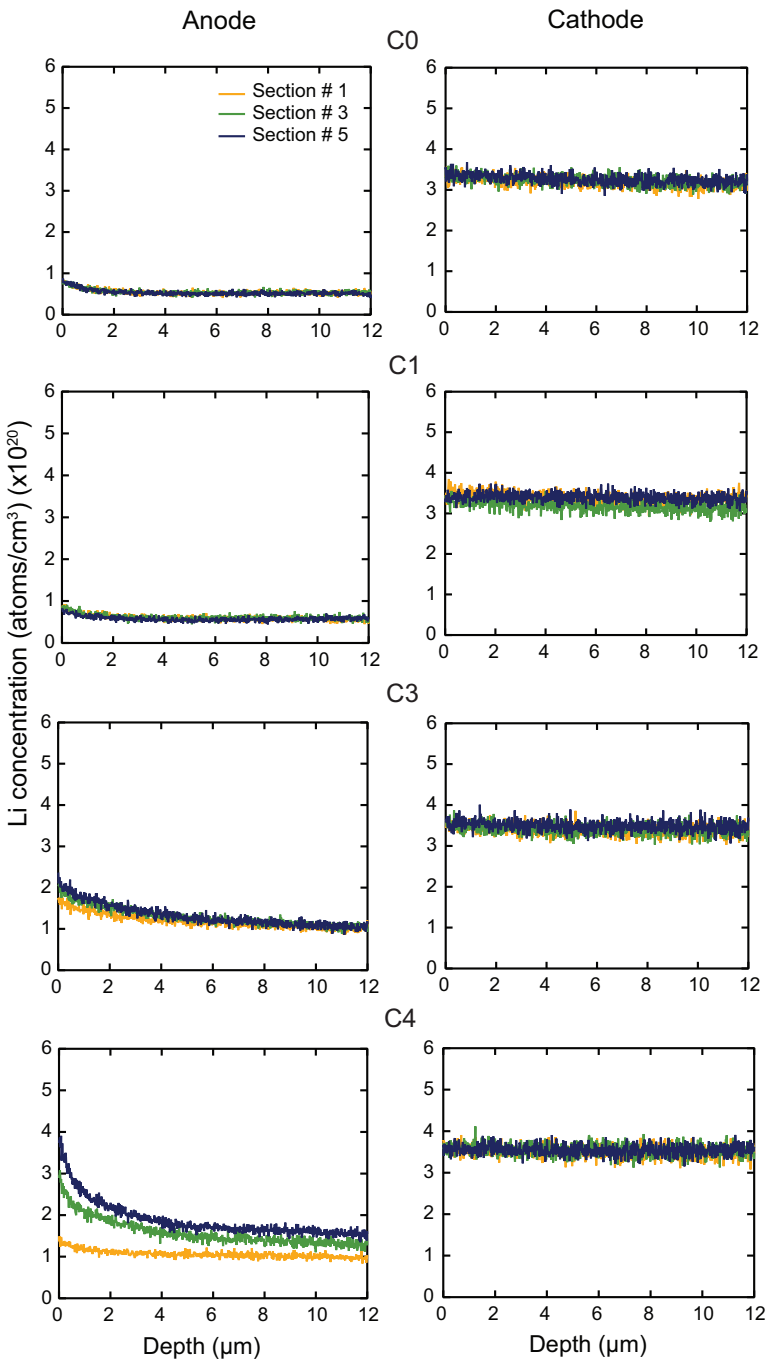

Figure 8.12: Effect of C-rate on the lithium concentration in anode and cathode. The profiles were measured in all six sections from C0, C1, C3, and C4; only profiles over section 1, 3 and 5 are shown here. Based on the Li concentration profile in the anode, the lithium tends to build up at the surface of the anode samples aged with higher C-rates, whereas the lithium concentration drops along the thickness of the cathode anode samples. The SOC varies from 0 to 10 %

1, 3, and 5. The lithium concentration profile in cell C4 (same as in **Fig. 8.12**) is shown again in this figure for comparison. In C6, even though the C-rate is high, the amount of lithium buildup near the surface of the anode is less as compared to C4. The prominent change of lithium concentration profiles in the anode from section # 1 to section # 5 observed in C4 is also absent in C6 except for minor deviations near the sub-surface. Similar to C4, the lithium concentration profiles in sections # 1, 3, and 5 of cell C6 are identical to each other. However the lithium concentration profile for C6 has dropped below the concentration profile in C4. Thus, the overall lithium concentration in the cathode has dropped significantly in C6 as compared to C4. Thus at a higher SOC and moderate C-rate, the lithium buildup on the surface of the anode is contained, but lithium is lost from the host cathode material. In **Fig. 8.13b** the lithium concentration profile in section # 5 of C16 is compared with C0. In this case cell C16 is cycled between 45 and 55 % but with a very high C-rate of 16C. It should be noted that cells C0 and C16 in this data were chosen from a different batch than the earlier cells. The basic chemistry was the same, but the initial lithium concentration in the cathode was much higher in these cells. The lithium buildup on the surface of the anode was very high in C16 compared to any other cell in this study. The concentration in the anode dropped across its thickness with a steep slope. The lithium concentration profile in the cathodes of cells C0 and C16 are identical, but the concentration of lithium in the cathode was significantly lower than in C0. Thus, at moderate SOC but very high C-rate the process of lithium buildup on the surface of the anode is enhanced while there is significant loss of lithium from the host cathode. These results suggest that a cell operating at high SOC and moderate

C-rate has the least amount of lithium build up on the anode surface, and also the least amount of lithium is lost from the host cathode.

Figure 8.14 shows the lithium concentration profiles obtained on section # 3 of cell C0 and C6 at various locations within the same section. The aim here was to identify any change in the lithium concentration profiles measured at spots away from the center of the given section. The lithium concentration profiles in the anode shown in the left column of **Fig. 8.14** are similar for both cells at various locations on section # 3. This indicates that the lithium concentration in the anode does not vary along the height of the anode. The right column shows the lithium concentration profile in the cathode from both cells. The profiles for C0 measured at various locations on section # 3 are identical, but the profile measured at the center spot on the front side has a higher surface concentration and shows a higher gradient along the thickness than at any other location on the section # 3. The profiles for C6 measured at various locations on section # 3 are identical. Since the intensity and change in the lithium concentration in the unaged cell (C0) were greater at the center of the section, the measurements were taken at the center of each section throughout this study.

As expected for a completely discharged unaged cell (C0) (**Fig. 8.12**), the lithium concentration in the anode is significantly lower with little buildup of lithium at the surface, while most of the lithium is concentrated in the cathode. The lithium concentration profiles in the anode show higher surface concentration as the C-rate increases. The lithium concentration is at maximum near the surface, and it decays exponentially with the depth (thickness) of the sample. The lithium buildup on the anode surface from a cell cycled at higher SOC is less but increases with increasing C-rate. The lithium concentration drops in the cathode with higher SOC and higher

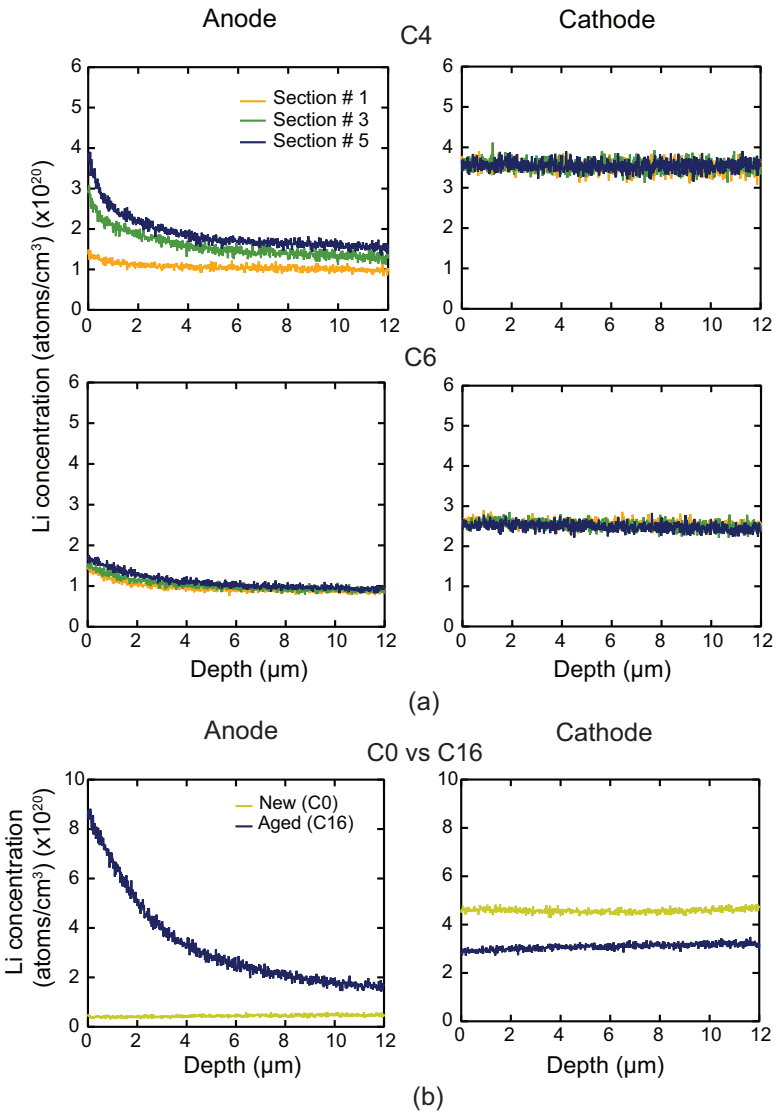

Figure 8.13: Effect of state of charge (SOC) and C-rate on the lithium concentration profile in anode and cathode, (a) in section 1, 3 and 5 from C4 and C6, and (b) comparison between section 5 from C0 and C16. The lithium buildup on the anode surface from a cell cycled at higher SOC is less but increases with increasing C-rate. The lithium concentration drops in the cathode with higher SOC and higher C-rate. The SOC varies from 0 to 10 % for C4, 45 to 55 % for C6, and 60 to 70 % for C16 during cycling of the cell.

C-rate. The lithium concentration profiles in the cathode show a uniform gradient, but the concentration decreases with increasing C-rate.

The analysis of the surface lithium concentration in the anode is shown in **Fig. 8.15**. As seen in **Fig. 8.15a** the surface lithium concentration is nearly constant over all the sections for C0 and C1. In the case of C3 and C4 the surface lithium concentration increases from section # 1 to section # 5. Thus the buildup of lithium on the surface of the anode is greater towards the core of the cylindrical cell than against the outer edge. For example, in the case of cell C4 where the highest change is observed, the concentration increases from 1.36×10^{20} to 3.74×10^{20} atoms/cm^3 from edge to core. In **Fig. 8.15b** the effect of C-rate on the lithium concentration gradient in anode is shown. The lithium concentration gradient increases with the C-rate. The lithium concentration gradient is very small in the case of cells C0 and C1 and is very prominent in the case of cells C3 and C4. The lithium concentration gradient in all cells exists only for a certain depth from the surface of the anode. The depth up to which the lithium concentration gradient exists in the anode also increases with the C-rate. In the case of cell C4 the lithium concentration gradient exists up to $\sim 1\mu m$ in the anode. Thus with increasing C-rate not only does the lithium buildup on the surface increase, but the lithium build up in the sub-surface area also increases.

It is well known that a solid electrolyte layer (SEI) composed of the decomposition products of the electrolyte salt and the solvent is formed on the surface of the anode [Vetter et al., 2005]. The thickness of the SEI is usually of the order of tens of nanometer [Edström et al., 2006; Yoshida et al., 2006]. This thickness of the SEI on a given type of anode varies depending on the electrolyte components, mode of cycling, overpotential, temperature etc. [Peled et al., 1998; Li et al., 2001; Zhang et al., 2004;

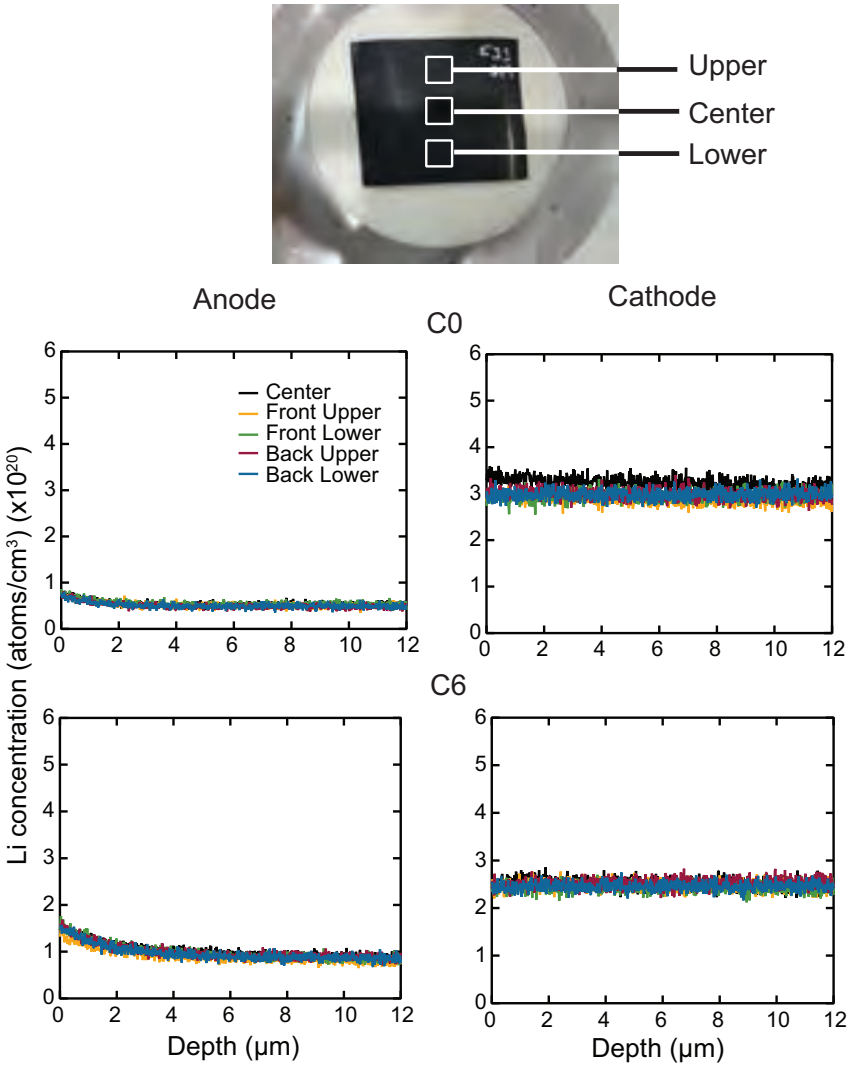

Figure 8.14: Lithium concentration profiles measured at different locations on section # 3 in the anode and cathode of C0 and C6 cell. The profiles were measured at three different spots along a straight line on one face (front) and on two spots on the opposite face (back). There is no change in the concentration profiles along the straight vertical line in a section.

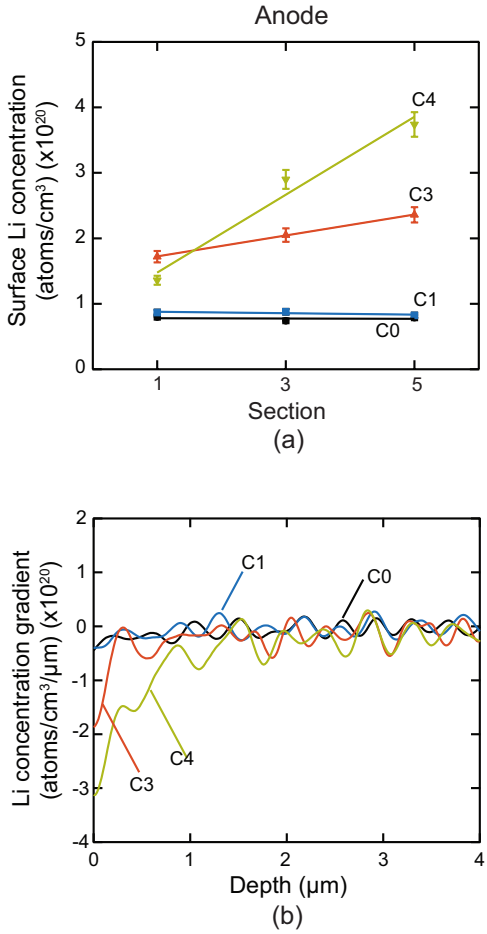

Figure 8.15: (a) Surface lithium concentration of the anode samples taken from cells aged with different C-rate. The surface concentration increases linearly with C-rate. The surface concentration also increases from section 1 to 5 within a cell. (b) Lithium concentration gradient in section # 3 of the anode samples taken from cells aged with different C-rate. The concentration gradient increases with C-rate up to a certain depth of the anode. The depth at which concentration gradient disappears increases with C-rate

Verma et al., 2010]. The lithium concentration profiles for the anode presented here not only indicate higher lithium content in the SEI layer at higher C-rate, but also show that the lithium concentration in the SEI layer is changing from the outer edge to the core of the cylindrical cell aged at a certain C-rate. This has never been reported before in literature. This study reveals that the anode-electrolyte interphase cannot be assumed to be alike over the length of the anode in a cylindrical cell as is the common practice adapted in Li-ion cell modeling.

The analysis of the surface lithium concentration was also conducted and is presented in **Fig. 8.16**. A buildup of lithium on the surface as seen in the anode is not observed in cathode samples from different cells. Since there is no buildup it is certain that there is no lithium plating occurring at the cathode surface. The initial expectation was a decrease in the lithium concentration in the aged sample as compared to the unaged sample. The decrease in the lithium concentration in the case of cells C1, C3, and C4 (**Fig. 8.12**) is not very prominent, but the results in **Fig. 8.13** are in good agreement with this hypothesis. Therefore, there is a critical C-rate beyond which the drop in the lithium concentration from the cathode is noticeable. In **Fig. 8.16**, the analysis of the lithium concentration gradient along the depth of the cathode is shown for section # 3 of different cells. The lithium concentration gradient observed on a particular section decreases exponentially with the C-rate, as shown by the curve in **Fig. 8.16**. For example, in the case of cells C0 and C4 the gradients are -1.63×10^{18} atoms/cm^3/μm and -0.46×10^{18} atoms/cm^3/μ m. For a higher C-rate the concentration gradient is lower, indicating that the flux available for diffusion of lithium into the cathode particles is decreasing. Thus the further cycling of the cells at still higher C-rate will be strongly affected. Since the

concentration gradient has a negative slope, it indicates that the lithium diffusion within the $LiFePO_4$ is restricted as the diffusion front moves towards the current collector. No fluctuations were observed in the concentration profile as were observed by Whitney et al. [2009]. Thus there is no structural breakdown of the cathode material, unlike that concluded by Whitney et al. [2009].

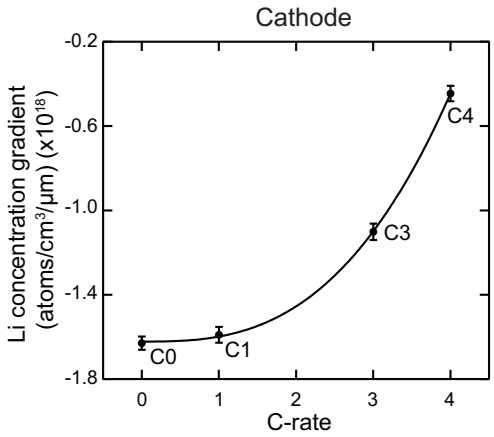

Figure 8.16: Lithium concentration gradient in section # 3 of the cathode samples taken from cells aged with different C-rate. The concentration gradient decreases with C-rate

The decrease in the lithium concentration can be explained by a change in the particle size or coarsening of the $LiFePO_4$ nanoparticles observed in physical/morphological studies. Due to the coarsening of the nanoparticles, the diffusion length for the lithium increases within each particle. As a result, the net uptake of lithium during the discharging processes is low. During each charge cycle lithium diffuses out of the $LiFePO_4$, and phase change occurs from $LiFePO_4$ to $FePO_4$. In the discharge cycle the lithium diffuses back in the host $FePO_4$ particle, and the phase changes from $FePO_4$

to $LiFePO_4$. During the early life of the battery the phase change from $LiFePO_4$ to $FePO_4$ and back to $LiFePO_4$ might be complete, but as the particle size increases due to coarsening, the diffusion length changes, and this will affect the phase change. The incomplete phase change continues to occur in subsequent cycles while the particle size tends to increase. Thus the lithium retaining capacity of the particle drops in each subsequent cycle. The loss of active lithium in the cathode is directly related to the drop in capacity of the battery while the increase in the particle size and the subsequent increase in the diffusion length are directly related to the rate capabilities of the battery.

In summary, The Li concentration profile across the electrodes of the cells at the end of life is affected by the C-rate of the charge/discharge cycle and SOC of the battery. The Li concentration profile changes along the length of the electrode from outer edge to the core of the cylindrical cell, but it remains constant along the height of the electrode. In the case of anode, the lithium concentration profile decays exponentially along the thickness of the anode. The Li builds up on the surface of the anode, and the buildup rate increases along the length of the anode and also with the Crate. This buildup below the surface extends to higher depth in cells cycled at higher C-rate. There is no buildup of the lithium near the cathode surface. Beyond a certain critical C-rate the lithium concentration drops with increasing C-rate, and it has a constant gradient along the depth of the cathode. The gradient of the lithium concentration profile in the cathode decreases with increasing C-rate. While the coarsening of the $LiFePO_4$ particles limits the diffusion of the lithium in the cathode, the surface concentration of the lithium on the anode increases with the

C-rate. The quantitative measure of the lithium profiles for anode and cathode can prove instrumental in calibrating the diffusion models of the Li-ion cells.

8.7 Summary

In summary the chemical and structural characterization of the $LiFePO_4$ nanoparticles reveals change in the lithium concentration, local lithium bonding and local Li environment. According to the XRD studies both $LiFePO_4$ and $FePO_4$ phases coexisted in the aged samples. The presence of the $FePO_4$ could indicate that there are regions within the cathode strip, which are inactive during the charging-discharging process. A more quantitative analysis of the phases present within the samples is necessary to identify the ratios of the inactive material. The change in the volumetric concentration of the active material would be a very important input to the electrochemical and performance models of the Li-ion batteries.

Raman studies show the degradation in the quality of the carbon coating. This has direct effect on the electronic conductivity of the composite cathode material. Due to the loss in the quality of the carbon the electrical resistance between the particles and the particles and the current collector can increase leading to the loss of the performance of the batteries. EELS showed that the density of states for O changes as the cell ages. This was evident in the presence of the pre-peak in the case of the O K edge. The increase in the ratio of the pre-peak to the O K edge peak in the EELS data from the core to the surface of the large $LiFePO_4$ particle indicates different lithium composition within the particle. There is also a shift of almost 2 eV for the $L_{2,3}$ edge of Fe in the aged sample. At a certain age of the cell the particles start to coarsen. The ion diffusion length is expected to increase in the

coarser particle, and this is expected to lead to an incomplete transformation between $LiFePO_4$ and $FePO_4$ while charging and discharging. The $FePO_4$ core is expected to expand in subsequent cycles, thus reducing the capacity of the host cathode material. The experimental results when analyzed with the help of simulated ELNES spectra for the olivine structure (space group Pnma) of $LixFePO_4$ with x = 0, 0.25, 0.5, 0.75, and showed 80 % loss of Li in aged cathode suggesting a strongly Li depleted, but not completely Li free, core region in the coarsened particles. Thus coarsening of the nanoparticles and the increase of the $FePO_4$ phase within the coarsened particle will lead to the loss of performance of the batteries.

NMR and NDP are used to overcome the limitation of electron spectroscopic studies in detecting the lithium in the samples. According to the NMR studies a single Li environment is present in the unpaged sample. The absence of the Li peak in the aged sample reasserted the results of the EELS suggesting the loss of the active Li from the host cathode material. The loss of active Li directly affects the cycling capacity of the battery. NDP measurements help in quantifying the loss of the active Li. The Li concentration profile measured with NDP across the electrodes of the cellsis affected by the C-rate of the charge/discharge cycle of the battery. The Li concentration profile is also affected by the state of charge of the cell. NDP measurements have also proved the effects of the cell shape and size on the aging of the battery. The Li concentration profile changes along the length of the electrode from outer edge to the core of the cylindrical cell, but it remains constant along the height of the electrode. In the case of anode, the lithium concentration profile decays exponentially along the thickness of the anode. The Li builds up on the surface of the anode, and the buildup rate increases along the length of the anode and also with

the C-rate. This buildup below the surface extends to higher depth in cells cycled at higher C-rate. There is no buildup of the lithium near the cathode surface. Beyond a certain critical C-rate the lithium concentration drops with increasing C-rate, and it has a constant gradient along the depth of the cathode. The gradient of the lithium concentration profile in the cathode decreases with increasing C-rate.

Chapter 9: Outlook and Summary

The increasing awareness about the green house gases has lead to the demand for clean renewable energy sources. The goal to reduce CO2 emissions from concentrated sources such as coal fired power plants or distributed sources such as automobiles along with reduced dependency on foreign oil can be achieved with efficient electrical energy storage devices. Understanding the degradation mechanisms in the EES is instrumental in developing safe, reliable and efficient devices with long cycle life.

Automobile industry is actively pursuing the development of electric vehicles and has adopted battery technology as the EES devices. Recently, advanced Li-ion batteries have been actively pursued as the electrical energy storage device for electric vehicles (EV), hybrid electric vehicles (HEV) and plug-in HEVs (PHEV) due to their high energy and power density over other battery chemistries. Use of current Li-ion batteries or future Li-air batteries in EV, HEV, PHEV, and also the temporary storage systems for renewable energy sources would reduce the dependence on fossil fuels and provide a clean energy technology.

While the mechanism of the operation of these batteries is known the aging mechanisms are still under investigation. Aging of the cells at the macroscopic or system level is quantified by the change in the internal resistance measured by impedance techniques. To understand the related loss of capacity, it is imperative to understand

the degradation of the electrode materials of the battery. The degradation of the material is caused by several simultaneous physiochemical processes that occur within the batteries which makes material characterization of the electrodes a challenging task.

Performance of any electrode material is investigated by testing these materials in a small experimental (so-called coin) cell. In commercial batteries the electrodes are made up of nanomaterials to leverage the effects of high surface area. These nanomaterials are packed together on an either copper or aluminum current collector strips. These long electrode strips are then rolled and packed into a cylindrical can. Thus commercial batteries are larger in size as they provide the necessary building blocks for the battery packs. The effects of scaling in the commercial cell might be overlooked if the results of the so-called coin cell experiments are to be believed alone. This further adds to the complexity of analyzing the degradation mechanisms in commercial batteries. As such a systematic multi-scale characterization plan is necessary to understand the degradation mechanisms of the battery.

The electrodes within the battery have been characterized by several different techniques with resolutions ranging from mm to nm. Techniques including thermography, scanning electron microscopy (SEM), transmission electron microscopy (TEM), atomic force microscopy (AFM), X-ray diffraction (XRD), Raman spectroscopy, nuclear magnetic resonance (NMR) and neutron depth profiling (NDP) have been applied at different length scales to obtain spatial and temporal data about the degradation of the electrode materials. Such multi-scale characterization plans are applicable to any existing battery chemistry or upcoming battery chemistries such as Li-air,

metal-air etc. In this overview paper a review of the results of such a multi-scale characterization applied to $LiFePO_4$ based Li-ion batteries has been presented.

Thermography maps provide the necessary visual data of the cathode strips in identifying the damaged areas for further characterization. Once the areas of interest are identified SEM and AFM are useful in studying the surface morphology and grain coarsening at μm to nm length scales. AFM is also useful in studying certain functional properties such as surface resistance and surface potential. TEM provides high resolution micrographs for particle analysis. Electron energy loss spectroscopy (EELS) is useful in identifying the bonding of the elements in the active material. XRD provides useful information about the lattice parameter, and Raman gives information about the carbon coating over the $LiFePO_4$ nanoparticles. NMR is useful in identifying the different chemical compositions of the $LiFePO_4$ nanoparticles after aging. NDP is instrumental in providing the lithium concentration profiles in the electrodes. These multi-scale studies reveal changes in thermal diffusivity, permanent phase change, structural disordering, coarsening of nanoparticles and loss of active lithium in the cathode over the life of the battery.

Coarsening has been identified a major aging parameter in these studies, but quantify the coarsening of the nanoparticles has remained a major challenge. Since the commercial cathodes are densely packed identifying the correct particle size distribution has been a difficult task so far. High-resolution imaging combined with image processing algorithms would be necessary to establish the particle size distribution in the cathode. Such a distribution would be a very important input to the modeling process as one can vary the distribution as the function of the aging of the battery and identify its performance.

The aging mechanisms identified above need to be further investigated. The multi-scale techniques that give spatial information should be applied such as to get the temporal data of the aging mechanisms. The above study was conducted on the batteries aged till they lost %20 of the capacity. Thus only the final effects of aging are visible through characterization. The batteries should be aged to different degrees between 100% and 80% capacity and then characterized according to the multi-scale techniques. Such a study would provide knowledge about on-set of aging and its progress through the life of the battery.

Aging of the batteries remains a challenge in such studies, because as the chemistries improve the life of the batteries improve. But to achieve conditions and see the effects of cycling similar to the real life aging cycle, the batteries should be aged properly with a synthetic aging cycle. Often even in synthetic aging cycle the battery aging has be accelerated to accomplish the studies within a certain time limit. Thus one should study the effects of accelerated aging cycles on actual aging of the batteries. These effects should then be filtered from the data to identify the true aging mechanisms.

Lastly, the studies selected in the multi-scale characterization are not limited to the device or to the chemistry of the device. They can be easily extended to the future generations of EES including but not limited to Li-air, Li-metal.

Appendix A: A Guide to Understanding Battery Specifications

(Taken from MIT Electric Vehicle Team, December 2008)

Battery Basics

This section explains the different battery classifications you might see in the electric vehicle literature.

- ***Cell, Module, and Pack*:** Hybrid and electric vehicles have a high voltage battery pack that consists of individual modules and cells organized in series and parallel. A cell is the smallest, packaged form a battery can take and is generally on the order of one to six volts. A module consists of several cells generally connected in either series or parallel. A battery pack is then assembled by connecting modules together, again either in series or parallel.

- ***Battery Classifications*:** There are several ways batteries are classified. Firstly the batteries are classified based on their usability as secondary and primary batteries. A primary battery is one that cannot be recharged. A secondary battery is one that is rechargeable.

  Secondly, the batteries are classified based on their chemistry. For e.g: Lead

acid, Nickel metal hydride, Li-ion etc... Batteries of same chemistry are further classified based on their application or shape. Based on the application, the main trade-off in battery development is between power and energy. Batteries can be either high-power or high-energy, but not both. Often manufacturers will classify batteries using these categories. Other common classifications are High Durability,meaning that the chemistry has been modified to provide higher battery life at the expense of power and energy.

Thirdly, the batteries are classified based on their shape as prismatic, cylindrical or pouch batteries.

- ***C- and E- Rates*:** In describing batteries, discharge current is often expressed as a C-rate in order to normalize against battery capacity, which is often very different between batteries. A C-rate is a measure of the rate at which a battery is discharged relative to its maximum capacity. A 1C rate means that the discharge current will discharge the entire battery in 1 hour. For a battery with a capacity of 100 Ah (Amp-hr), this equates to a discharge current of 100 Amps. A 5C rate for this battery would be 500 A, and a C/2 rate would be 50 A. Similarly, an E-rate describes the discharge power. A 1E rate is the discharge power to discharge the entire battery in 1 hour.

Battery Condition

This section describes some of the variables used to describe the present condition of a battery.

- ***State of Charge (SOC)* (%):** An expression of the present battery capacity as a percentage of maximum capacity. SOC is generally calculated using current integration to determine the change in battery capacity over time.

- ***Depth of Discharge (DOD)* (%):** The percentage of battery capacity that has been discharged expressed as a percentage of maximum capacity. A discharge to at least 80 %DOD is referred to as a deep discharge.

- ***Terminal Voltage* (V):** The voltage between the battery terminals with load applied. Terminal voltage varies with SOC and discharge/charge current.

- ***Open-circuit Voltage* (V):** The voltage between the battery terminals with no load applied. The open-circuit voltage depends on the battery state of charge, increasing with state of charge.

- ***Internal Resistance* (Ω):** The resistance within the battery, generally different for charging and discharging, also dependent on the battery state of charge. As internal resistance increases, the battery efficiency decreases and thermal stability is reduced as more of the charging energy is converted into heat.

Battery Technical Specifications

This section explains the specifications you may see on battery technical specification sheets used to describe battery cells, modules, and packs.

- ***Nominal Voltage* (V):** The reported or reference voltage of the battery, also sometimes thought of as the normal voltage of the battery.

- ***Cut-off Voltage* (V):** The minimum allowable voltage. It is this voltage that generally defines the empty state of the battery.

- ***Capacity or Nominal Capacity (for a specific C-rate)* (Ah):** The coulometric capacity, the total Amp-hours available when the battery is discharged at a certain discharge current (specified as a C-rate) from 100 percent state-of-charge to the cut-off voltage. Capacity is calculated by multiplying the discharge current (in Amps) by the discharge time (in hours) and decreases with increasing C-rate.

- ***Energy or Nominal Energy (for a specific C-rate)* (Wh):** The energy capacity of the battery, the total Watt-hours available when the battery is discharged at a certain discharge current (specified as a C-rate) from 100 percent state-of-charge to the cut-off voltage. Energy is calculated by multiplying the discharge power (in Watts) by the discharge time (in hours). Like capacity, energy decreases with increasing C-rate.

- ***Cycle Life (number for a specific DOD)*:** The number of discharge-charge cycles the battery can experience before it fails to meet specific performance criteria. Cycle life is estimated for specific charge and discharge conditions. The actual operating life of the battery is affected by the rate and depth of cycles and by other conditions such as temperature and humidity. The higher the DOD, the lower the cycle life.

- ***Specific Energy* (Wh/kg):** The nominal battery energy per unit mass, sometimes referred to as the gravimetric energy density. Specific energy is a characteristic of the battery chemistry and packaging. Along with the energy consumption of the vehicle, it determines the battery weight required to achieve a given electric range.

- ***Specific Power* (W/kg):** The maximum available power per unit mass. Specific power is a characteristic of the battery chemistry and packaging. It determines the battery weight required to achieve a given performance target.

- ***Energy Density* (Wh/L):** The nominal battery energy per unit volume, sometimes referred to as the volumetric energy density. Energy density is a characteristic of the battery chemistry and packaging. Along with the energy consumption of the vehicle, it determines the battery size required to achieve a given electric range.

- ***Power Density* (W/L):** The maximum available power per unit volume. Power density is a characteristic of the battery chemistry and packaging. It determines the battery size required to achieve a given performance target.

- ***Maximum Continuous Discharge Current* (A):** The maximum current at which the battery can be discharged continuously. This limit is usually defined by the battery manufacturer in order to prevent excessive discharge rates that would damage the battery or reduce its capacity. Along with the maximum continuous power of the motor, this defines the top sustainable speed and acceleration of the vehicle.

- ***Maximum 30-sec Discharge Pulse Current* (A):** The maximum current at which the battery can be discharged for pulses of up to 30 seconds. This limit is usually defined by the battery manufacturer in order to prevent excessive discharge rates that would damage the battery or reduce its capacity. Along with the peak power of the electric motor, this defines the acceleration performance (0-60 mph time) of the vehicle.

- ***Charge Voltage* (V):** The voltage that the battery is charged to when charged to full capacity. Charging schemes generally consist of a constant current charging until the battery voltage reaching the charge voltage, then constant voltage charging, allowing the charge current to taper until it is very small.

- ***Float Voltage* (V):** The voltage at which the battery is maintained after being charge to 100 percent SOC to maintain that capacity by compensating for self-discharge of the battery.

- ***(Recommended) Charge Current* (A):** The ideal current at which the battery is initially charged (to roughly 70 percent SOC) under constant charging scheme before transitioning into constant voltage charging.

- ***(Maximum) Internal Resistance* (Ω):** The resistance within the battery, generally different for charging and discharging.

Bibliography

Abraham, D. P., Dees, D. W., Knuth, J., Reynolds, E., Gerald, R., Hyung,Y.-E, and et al.,"Diagnostic Examination of Generation 2 Lithium-Ion Cells and Assessment of Performance Degradation Mechanisms," Eds. Abraham., D. P., Oak Ridge National Laboratory, TN. Report # **ANL-05/21**. Available from: <http://www.osti.gov/bridge/product.biblio.jsp?query_id=0&page=0&osti_id=861617&Row=0&formname=basicsearch.jsp>

Andersson, A. S. and Thomas, J. O, "The Source of First Capacity Loss in $LiFePO_4$," *J. Power Sources* **97-98**, 498-502 (2001).

André, S., and Degiovanni, A., "A Theoretical Study of the Transient Coupled Conduction and Radiation Heat Transfer In Glass: Phonic Diffusivity Measurements By the Flash Technique," *Int. J. Heat Mass Transfer* textbf38, 3401-3412 (1995).

Anisimov, V. I., Zaanen, J., and Andersen, O. K., "Band Theory and Mott Insulators: Hubbard U instead of Stoner I," *Phys. Rev. B* **44**, 943-954 (1991).

Anonymous, "Standard Test Method for Thermal Diffusivity of Solids by the Flash Method," ASTM Designation: E 1461 92, 1992.

Anonymous, "FreedomCAR 42 V Energy Storage System End-of-Life Performance Goals," Southfield, MI, USABC, 2002. Available from: <http://www.uscar.org/guest/view_team.php?teams_id=12>

Anonymous, "Application Modules Training Supplement," Veeco Instruments Inc., Santa Barbara, CA (Feb. 2004).

Anonymous, "USABC Goals for Advanced Batteries for Evs," Southfield, MI, USABC, (2006a). Available from: <http://www.uscar.org/guest/view_team.php?teams_id=12>

Anonymous, "USABC Requirements of End of Life Energy Storage Systems for PHEVs," Southfield, MI, USABC, (2006b). Available from: <http://www.uscar.org/guest/view_team.php?teams_id=12>

Anonymous, Overview of lithium-ion batteries, Panasonic Corp., Secaucus, NJ, 2007. <http://www.panasonic.com/industrial/battery/oem/chem/lithion/index.html>.

Arnold, G., Garche, J., Hemmer, R., Ströbele, S. , Vogler, C., and Wohlfahrt-Mehrens, A., "Fine-particle Lithium Iron Phosphate $LiFePO_4$ Synthesized by A New Low-cost Aqueous Precipitation Technique," *J. Power Sources*, **119-121**, 247-251 (2003).

Arrabito, M., Bodoardo, S., Penazzi, N., Panero, S., Reale, P., Scrosati, B., Wang, Y., Guo, X., and Greenbaum, S. G., "Correlation Between Structural and Electrochemical Properties of Li Metal Vanadates," *J. Power Sources*, **97-98**, 478-481 (2001).

Azizi, S., Batsale, J.-C.,Moyne, C., and Degiovanni A., "Mesure de la conductivité thermique de milieux poreux non saturés : analyse théorique et expériences," *High Temp-High Press.* **21**, 383-389 (1989).

Baba, T., and Ono, A., "Improvement of the Laser Flash Method to Reduce Uncertainty in Thermal Diffusivity Measurements," *Meas. Sci. Technol.* **12**, 2046-2057 (2001).

Balageas, D., "Thermal Diffusivity Measurement by Pulsed Methods," *High Temp-High Press.* **21**, 85-96 (1989).

Batsale, J.-C., Gobbe, C., and Quintard, M., "Local Non-equilibrium Heat Transfer in Porous Media," *Recent Res. Devel. Heat, Mass Momentum Transfer* **1** (1996).

Bendat, J. S. and Piersol., Engineering Applications of Correlation and Spectral Analysis, second ed. (Wiley, New York, 1986).

Benoit, C., and Franger, S., "Chemistry and Electrochemistry of Lithium Iron Phosphate ," *J. Solid State Electrochem.* **12**, 987-993 (2008).

Bhattacharya, A., Calmidi, V. V., and Mahajan, R. L., "Thermophysical Properties of High Porosity Metal Foams," *Intl. J. Heat Mass Transfer* **45**, 1017-1031 (2002).

Bhushan, B., "Chemical, Mechanical and Tribilogical Characterization of Ultra-thin and Hard Amorphous Carbon Coatings As Thin As 3.5 nm: Recent Developments," *Diam. Relat. Mater.* **8**, 1985-2015 (1999).

Bhushan, B., and Goldade A., "Measurements and Analysis of Surface Potential Change During Wear of Single-Crystal Silicon (100) at Ultralow Loads using Kelvin Probe Microscopy," *Appl. Surf. Sci.* **157**, 373-381 (2000).

Bhushan, B., Springer Handbook of Nanotechnology, second ed. (Springer-Verlag, Heidelberg, Germany, 2007).

Bhushan, B., Nanotribology and Nanomechanics An Introduction, second ed. (Springer-Verlag, Heidelberg, Germany, 2008).

Biersack, J.P., and Fink, D. Implantation of Boron, and Lithium in Semiconductors, and Metals, in: S. Namba (Ed.), Ion Implantation in Semiconductors, Plenum Press, New York, NY, 1975, pp. 211-218.

Binnig, G., Quate, C.F., and Gerber, C., "Atomic Force Microscope," *Phys. Rev. Lett.* **56**, 930-933 (1986).

Blint, R. J., "Binding of Ether and Carbonyl Oxygens to Lithium Ion," *J. Electrochem. Soc.* **142**, 696-702 (1995).

Brown, A. I., and Marco, S. M., Introduction to Heat Transfer, 3rd Ed, McGraw-Hill, (1958).

Bruce, P. G., Scrosati, B. and Tarascon, J-M., "Nanomaterials for Rechargeable Lithium Batteries," *Angew. Chem. Int.* **47**, 2930-2946 (2008).

Buchmann I (2001)," Batteries in a portable world: a handbook on rechargeable batteries for non-engineer," 2nd ed. Cadex Electronics Inc., Richmond.

Carlier, D., Ménétrier, M., and Delmas, C., "^{7}Li MAS NMR Study of Electrochemically Deintercalated LixNi$_{0.30}$Co$_{0.70}$O$_2$ Phases: Evidence of Electronic and Ionic Mobility, and Redox Processes," *J. Mater. Chem.* **11**, 594-603 (2001a).

Carlier, D., Saadoune, I., Croguennec, L., Ménétrier, M., Suard, E., and Delmas, C., "On the Metastable O$_2$-type LiCoO$_2$," *Solid State Ionics* **144**, 263-276 (2001b).

Carrette, L., Friedrich, K. A. and Stimming, U., "Fuel cells: Principles, types, fuels and applications," *Chem. Phys. Chem.* **1**, 162-193 (2000).

Chehab, Z., Serrao, L., Guezennec, Y., and Rizzoni, G., "Aging characterization of nickel metal hydride batteries using electrochemical impedance spectroscopy," In: *Proceedings of the 2006 ASME International Mechanical Engineering Congress and Exposition: Dynamic Systems Parts A and B* **IMECE2006-14608**, 343-349 (2006).

Chen, G., Song, X., and Richardson T. J., "Electron Microscopy Study of LiFePO$_4$ to FePO$_4$ Phase Transition," *Electrochem. Solid. St. Lett.* **9**, A295-A298 (2006).

Chevallier, F., Letellier, M., Morcrette, M., Tarascon, J.-M., Frackowiak, E., Rouzaud, J.-N., and Béguin, F., "In Situ ^{7}Li-Nuclear Magnetic Resonance Observation of Reversible Lithium Insertion into Disordered Carbons," *Electrochem. Solid St.* **6**, A225-A228 (2003).

Cho, N-H., Krishnan, K. M., Veirs, D. K., Rubin, M. D., Hopper, C. B., and Bhushan, B., "Chemical Structure and Physical Properties of Diamond-like Amorphous Carbon Films Prepared by Magnetron Sputtering," *J. Mater. Res.* **5**, 2543-2554 (1990).

Cho, Y., Fey, G. H., and Kao, H., "The Effect of Carbon Coating Thickness on the Capacity of $LiFePO_4$/C Composite Cathodes," *J. Power Sources* **189**, 256-262 (2009).

Coquard, R., and Panel, B., "Adaptation of the FLASH Method to the Measurement of the Thermal Conductivity of Liquids or Pasty Materials," *Int. J. Thermal Sci.* **48**, 747-760 (2009).

Dahn, J. R., von Sacken, U., and Michal, C. A., "Structure and Electrochemistry of $Li_{1\pm y}NiO_2$ and a New Li_2NiO_2 Phase with the $Ni(OH)_2$ Structure," *Solid State Ionics* **44**, 87-97 (1990)

Degiovanni, A., "Diffusivity and the Flash Method," *Rev. Gen. Therm.* **185**, 417-442 (1977).

Degiovanni, A., Batsale, J.-C., and Maillet, D., "Mesure de la diffusivité longitudinale de matériaux anisotropes: Measurement of In-plane Diffusivity of Anisotropic Samples Survey of the Techniques Developed at LEMTA:: Panorama des techniques développées au LEMTA," *Revue générale de Thermique* **35**, 141-147 (1996).

Delacourt, C., Poizot, P., Levasseur, S., and Masquelier, C., "Size Effects on Carbon-Free $LiFePO_4$ Powders. The Key to Superior Energy Density," *Electrochem. Solid St.* **9**, A352-A355 (2006).

Delmas, C., Maccario, M., Croguennec, L., Cras F. LE, and Weill, F., "Lithium Deintercaltion in$LiFePO_4$ Nanoparticles via A Domino-cascade Model," *Nat. Mater.* **7**, 666-671 (2008).

DeVecchio, D., and Bhushan, B., "Use of a Nanoscale Kelvin Probe for Detecting Wear Precursors," *Rev. Sci Intsrum.* **60**, 3618-3624 (1998).

Doeff, M. M., Hu, Y., McLarnon, F., and Kostecki, R., "Effect of Surface Carbon Structure on the Electrochemical Performance of $LiFePO_4$" *Electrochem. Solid St.* **6**, A207-A209 (2003).

Downing, R. G., Fleming, R. F., Langland, J. K., and Vincent, D. H., "Neutron Depth Profiling at National Bureau of Standards," *Nuel. Inst. Methods* **218**, 47-51 (1983).

Downing, R. G., Lamaze, G. P., Langland, J. K., and Hwang S. T., "Neutron Depth Profiling: Overview and Description of NIST Facilities," *J. Res. Natl. Inst. Stand. Technol.* **98**, 109-126 (1993).

Duscher, G., Buckzo, R., Pennycook, S. J., and Pantelides, S. T., "Core Hole Effects on Energy Loss of Near Edge Structure," *Ultramicroscopy* **86**, 355-362 (2001).

Eckert, E. R., and Drake, R. M., Heat and Mass Transfer, McGraw-Hill, (1959).

Edström, K., Herstedt, M., and Abraham, D., "A New Look at the Solid Electrolyte Interphase on Graphite Anodes in Li-ion Batteries," *J. Power Sources* **153**, 380-384 (2006).

Exner, H. E., and Arzt, E., "Sintering Processes," Chapter 30 in Physical Metallurgy 3rd and revised Ed., Edited by R. W. Cahn and P. Haasen, Elsevier Science Publication 1983.

Fan, Q., Chupas, P. J. and Whittingham, M.S., "Characterization of Amorphous and Crystalline Tin-cobalt Anodes," *Electrochem. Solid-State Lett.* **10**, A274-A278 (2007).

Ferg, E., Gummow, R. J., de Kock, A. and Thackeray, M. M., "Spinel Anodes for Lithium-ion Batteries," *J. Electrochem. Soc.* **141**, L147-L150 (1994).

Ferrari, A. C., and Robertson, J., "Interpretation of Raman spectra of disordered and amorphous carbon," *Phys. Rev. B* **61**, 14095-14107 (2000).

Franger, S., Le Cras, F. , Bourbon, C., and Rouault, H., "Comparison Between Different $LiFePO_4$ Synthesis Routes and Their Influence on its Physico-chemical Properties," *J. Power Sources* **119-121**, 252-257 (2003).

Franger, S., Cras, F. Le., Bourbon, C., Benoit, C., Soudan, P., and Santos- Peña, J., In Recent Research Developments in Electrochemistry, Vol. 8, S. G. Pandalai (ed.) pp. 225-256, (Transworld Research Network, Kerala, India, 2005).

Fuller, T. F., Doyle, M., and Newman, J., "Simulation and Optimization of the Dual Lithium Ion Insertion Cell," *J. Electrochem. Soc.* **141**, 1-10 (1994).

Gaubicher, J., Wurm, C., Goward, G., Masquelier, C., and Nazar, L., "Rhombohedral Form of $Li_3V_2(PO_4)_3$ as a Cathode in Li-Ion Batteries," *Chem. Mater.* **12**, 3240-3242 (2000) .

Gee, B., Horne, C. R., Cairns, E. J., and Reimer, J. A., "Supertransferred Hyperfine Fields at ^{7}Li: Variable Temperature ^{7}Li NMR Studies of $LiMn_2O_4$-Based Spinels," *J. Phys. Chem. B* **102**, 10142-10149 (1998).

Gerald, R. E., Sanchez, J., Johnson, C. S., Klinger, R. J., and Rathke, J. W., "In Situ Nuclear Magnetic Resonance Investigations of Lithium Ions in Carbon Electrode Materials Using A Novel Detector," *J. Phys. Condens. Mater.* **13**, 8269-8285 (2001).

Giannuzzi, L. A., Drown, J. L., Brown, S. R., Irwin, R. B., and Stevie, F. A., "Focused Ion Beam Milling and Micromanipulation Lift-out for Site Specific Cross-Section TEM Specimen Preparation," *Materials Research Society Symposium Proceedings* 480 (Anderson, R.M. and Walck, S.D., Editors), pp. 19-27, 1997, Materials Research Society, Pittsburgh, PA.

Giannuzzi, L. A., and Stevie, F. A., "A Review of Focused Ion Beam Milling Techniques for TEM Specimen Preparation," *Micron* **30**, 197-204 (1999).

Gilliam, D. M., Lamaze, G. P., Dewey, M. S., and Greene, G. L., "Mass Assay and Uniformity Tests of Boron Targets by Neutron Beam Methods," *Nucl. Instrum. Methods Phys. Res. Sect. A-Accel. Spectrom. Dect. Assoc. Equip.* **334**, 149-153 (1993).

Goers, D., Holzapfel, M., Scheifele, W., Lehmann, E., Vontobel, P., and Novák P., "In Situ Neutron Radiography of Lithium-ion Batteries: The Gas Evolution on Graphite Electrodes During the Charging," *J. Power Sources* **130**, 221-226 (2004).

Goodenough, J. B., "Cathode Materials: A Personal Perspective ," *J. Power Sources* **174**, 9961000 (2007).

Grey, C. P., and Dupre, N., "NMR Studies of Cathode Materials for Lithium-ion Rechargeable Batteries," *Chem. Rev.* **104**, 4493-4512 (2004).

Grey, C. P., and Lee, Y. J., "Lithium MAS NMR Studies of Cathode Materials for Lithium-ion Batteries," *Solid State Sci.* **5**, 883-894 (2003).

Hahn, O., Raether, F., Arduini-Schuster, M. C., and Fricke, J., "Transient Coupled Conductive/radiative Heat Transfer in Absorbing, Emitting and Scattering Media: Application to Laser-Flash Measurements on Ceramic Materials," *Int. J. Heat Mass Transfer* **40**, 689-698 (1997).

Hahn T. (ed), *International Tables for Crystallography, Volume A: Space-Group Symmetry*, 5th revised ed., Kluwer, Dordrecht (2002).

Haile, S. M., "Fuel Cell Materials and Components," *Acta Mater.* **51**, 5981-6000 (2003).

Holman, J.P., Heat Transfer, 9th Ed., McGraw-Hill 2002

Hossain, S., Kim, Y-K., Saleh, Y. and Loutfy, R., "Comparative Studies of MCMB and C-C Composite as Anodes for Lithium-ion Battery Systems," *J. Power Sources* **114**, 264-276 (2003).

Islam, M. S., Driscoll, D. J., Fisher, C. A. J., and Slater, P. R., "Atomic-Scale Investigation of Defects, Dopants, and Lithium Transport in the $LiFePO_4$ Olivine-Type Battery Material," *Chem. Mater.* **17**, 5085-5092 (2005).

Jansen, A. N., Kahalan, A. J., Kepler, K. D., Nelson, P. A., Amine, K., Dees, D.W., Vissers, D. R. and Thackeray, M. M., "Development of a high-power lithium-ion battery," *J. Power Sources* **81**, 902-905 (1999).

Jacobson, A. J., "Materials for Solid Oxide Fuel Cells," *Chem. Mater.* **22**, 660-674 (2010).

Julien, C. M., Zaghib, K., Mauger, A., Massot, M., Ait-Salah, A., Selmane, M., and Gendron, F., "Characterization of the Carbon Coating onto $LiFePO_4$ Particles Used in Lithium Batteries," *J. Appl. Phys.* **100**, 063511 (2006).

Kanno, R., Kawamoto, Y., Takeda, Y., Ohashi, S., Imanishi, N. and Yamamoto, O., "Carbon Fiber as a Negative Electrode in Lithium Secondary Cells, *J Electrochem. Soc.* **139**, 3397-3404 (1992).

Kinyanjui, M. K., Axmann, P., Wohfahrt-Mehrens, M, Moreau, P., Boucher, F, and Kaiser, U., Origin of valence and core excitations in $LiFePO_4$ and $FePO_4$," *J. Physics: Condens. Matter* **22**, 275501-275509 (2010).

Klein, M. V., in Light Scattering in Solids III, Eds Cardona M., and Guntherodt G., Topics in Applied Physics Vol. 51, 121-171, Springer-Verlag, Berlin (1982).

Koch, V. R., Goldman, J. L., Mattos, C. J., and Mulvaney, M., "Specular Lithium Deposits from Lithium Hexafluoroarsenate/Diethyl Ether Electrolytes," *J. Electrochem. Soc.* **129**, 1-4 (1982) .

Kong, F., Kostecki, R., Nadeau, G., Song, X., Zaghib, K., Kinoshita, K. and McLarnon F., "In-situ Studies of SEI Formation," *J. Power Sources* **97-98**, 58-66 (2001).

Kononenko, V. I. Baranovskii, V. M., and Dushchenko, V. P. "Thermal Conductivity of Porous Sintered Iron," *Powder Metallurgy and Metal Ceramics* **7(3)**, 175-177 (1968).

Kostecki, R., and McLarnon, F., "Degradation of $LiNi_{0.8}Co_{0.2}O_2$ Cathode Surfaces in High-Power Lithium-Ion Batteries," *Electrochem. Solid State Lett.* **5**, A164-A166 (2002).

Kostecki, R. and McLarnon, F., "Local Probe Studies of Degradation of Composite $LiNi_{0.8}Co_{0.15}Al_{0.05}O_2$ Cathodes in High-power Lithium-ion Batteries," *Electrochem Solid State Lett.* **7**, A380-A383 (2004).

Kötz, R., and Carlen, M., "Principles and Application of Electrochemical Capacitors," *Electrochim. Acta* **45**, 2483-2498 (2000).

Krapez, J.-C., "Mesure de diffusivit longitudinale de plaques minces par mthode de grille," In : Proceedings of Journe SFT **Thermographie IR quantitative**, ONERA, (1999).

Kresse, G., and Furthmüller, J., "Efficiency of Ab-initio Total Energy Calculations for Metals and Semiconductors Using a Plane-wave Basis Set," *Comp. Mater.Sci.* **6**, 15-50 (1996a).

Kresse, G., and Furthmüller, J., "Efficient Iterative Schemes for Ab-initio Total-energy Calculations Using a Plane-wave Basis Set," *Phys. Rev. B* **54**, 11169-11186 (1996b).

Krings, L. H. M., Tamminga, Y., Berkumc, J. van, Labohm, F., Veen, A. van, and Arnoldbik W. M., "Lithium Depth Profiling in Thin Electrochromic WO_3 Films," *J. Vac. Sci. Technol. A* **17**, 198-205 (1999).

Laffont, L., Delacourt, C., Gibot, P., Wu, M. Y., Kooyman, P., Masquelier, C., and Tarascon, J. M., "Study of the $LiFePO_4/FePO_4$ Two-Phase System by High-Resolution Electron Energy Loss Spectroscopy," *Chem. Mater.* **18**, 5520-5529 (2006).

Lafond-Huot, M., and Bransier, J., "Caracterisation thermocinetique de materiaux composites fibreux soumis a un flux de rayonnement impulsionnel," *Lett. Heat Mass Trans.* **9**, 49-58 (1982).

Lamaze, G. P., Chen-Mayer, H. H., Becker, D. A., Vereda, F., Goldner, R. B., Haas, T., and Zerigian, P., "Cold Neutron Depth Profiling of Lithium-Ion Battery Materials," *J. Power Sources*, **119-121**, 680-685 (2003).

Larson, K. B., and Koyama, K., "Measurement by the Flash Method of Thermal Diffusivity, Heat Capacity, and Thermal Conductivity on Two-Layer Composite Samples," *J. Appl. Phys.* **39**, 4408-4416 (1968).

Lazard, M., André, S., and Maillet, D., "Diffusivity Measurement of Semitransparent Media: Model of the Coupled Transient Heat Transfer and Experiments on Glass, Silica Glass and Zinc Selenide," *Int. J. Heat Mass Transfer* **47**, 477-487 (2004).

Lee, Y.J., Wang, F., and Grey, C.P., "^{6}Li and ^{7}Li MAS NMR Studies of Lithium Manganate Cathode Materials," *J. Am. Chem. Soc.* **120**, 12601-12613 (1998).

Lee, Y. J., and Grey, C. P., "^{6}Li Magic-Angle Spinning (MAS) NMR Study of Electron Correlations, Magnetic Ordering, and Stability of Lithium Manganese(III) Oxides," *Chem. Mater.* **12**, 3871-3878 (2000).

Lee, Y.J., Wang, F., Mukerjee, S., McBreen, J., and Grey, C.P., "^{6}Li and ^{7}Li Magic-Angle Spinning Nuclear Magnetic Resonance and In Situ X-Ray Diffraction Studies of the Charging and Discharging of $Li_xMn_2O_4$ at 4 V," *J. Electrochem. Soc.* **147**, 803-812 (2000).

Lee, Y. J., Eng, C., and Grey, C. P., "^{6}Li Magic Angle Spinning NMR Study of the Cathode Material $LiNi_xMn_{2-x}O_4$:The Effectof Ni Doping on the Local Structure during Charging," *J. Electrochem. Soc.* **148**, A249-A257 (2001).

Levasseur, S., Ménétrier, M., Suard, E., and Delmas, C., "Evidence for Structural Defects in Non-stoichiometric HT-$LiCoO_2$: Electrochemical, Electronic Properties and ^{7}Li NMR Studies," *Solid State Ionics* **128**, 11-24 (2000).

Li, J., Murphy, E., Winnick, J., and Kohl, P., "The Effects of Pulse Charging on Cycling Characteristics of Commercial Lithium-ion Batteries," *J. Power Sources* **102**, 302-309 (2001).

Li, Z. G., Harlow, R. L, Gao, F., Lin, P., Miao, R., and Liang, L., "Crystalline Characterization of An Operational Li-ion Battery by Synchrotron X-ray Diffraction," *J. Electrochem. Soc.* **150**, A1171-A1175 (2003).

Luc, A. M., and Balageas, D. L., "Comportement thermique des composites á renforcement orienté soumis á des flux impulsionnels," *High Temp-High Press.* **16**, 209-219 (1984).

Maccario, M., Croguennec, L., Desbat, B., Couzi, M., Le Cras, F., and Servant, L., "Raman and FTIR Spectroscopy Investigations of Carbon-Coated Li_xFePO_4 Materials," *J. Electrochem. Soc.* **155**, A879-A886 (2008).

Maglić K. D., and Taylor R. E., In: *Compendium of Thermophysical Property Measurement Methods* Vol. 2 *Recommend Measurement Techniques and Practices* pp. 281 (Plenum, New York, 1984).

Marano, V., Onori, S., Guezennec, Y., Rizzoni, G., Madella, N., "Lithium-ion Batteries Life Estimation for Plug-in Hybrid Electric Vehicles," *Vehicle Power and Propulsion Conference, 2009. VPPC'09. IEEE* 536-543 (2009).

Mantia, F. A., "Characterization of Electrodes for Lithium-Ion Batteries through Electrochemical Impedance Spectroscopy and Mass Spectrometry," PhD Thesis, (2008).

Marcicki, J., Rizzoni, G., Conlisk, A. T., and Canova, M., "A Reduced-Order Electrochemical Model of Lithium-Ion Cells for System Identification of Battery Aging, " *Proceedings of the 4th Annual Dynamic Systems and Control Conference, invited session "Modeling and Estimation for Automotive & Energy Systems"*. Arlington, VA, (2011).

Marichal, C., Hirschinger, J., Granger, P., Ménétrier M., Rougier, A., and Delmas, C., "^{6}Liand ^{7}Li NMR in the $LiNi_{1-y}Co_yO_2$ Solid Solution ($0 \leq y \leq 1$)," *Inorg. Chem.* **34**, 1773-1778 (1995).

Matthews, M. J., Pimenta, M. A., Dreesselhaus, G., Dreesselhaus, M. S., and Endo, M., "Origin of Dispersive Effects of The Raman D Band In Carbon Materials," *Phys. Rev. B* **59**, R6585-R6588 (1999).

Miao, S., Kocher, M., Rez, P., Fultz, B., Yazami, R., and Ahn, C. C., "Local Electronic Structure of Olivine Phases in Li_xFePO_4," *J. Phys. Chem. A* **111**, 4242-4247(2007).

Miller, J. R., and Simon, P., "Electrochemical Capacitors for Energy Management," *Science* **321**, 651-652 (2008).

Miller, J. R., and Burke, A. F., "Electrochemical Capacitors: Challenges and Opportunities for Real-World Applications," *Electrochem. Soc. Interf.* **17**, 53-57 (2008).

Monkhorst, H. J., and Pack, J. D., "Special Points for Brillouin-zone Integrators," *Phys. Rev. B* **13**, 5188-5192 (1976).

Morgan, D., Van der Ven, A., and Ceder, G., "Li Conductivity in Li_xMPO_4 (M = Mn, Fe, Co, Ni) Olivine Materials ," *Electrochem. Solid St.* **7**, A30-A32 (2004).

Morgan, K. R., Collier, S., Burns, G., and Ooi, K., "A ^{6}Li and ^{7}Li MAS NMR Study of the Spinel-Type Manganese Oxide $LiMn_2O_4$ and The Rock Salt-Type Manganese Oxide Li_2MnO_3," *J. Chem. Soc.* **Chem. Commun.**, 1719-1720 (1994).

Moyne, C., Batsale, J.-C., and Degiovanni, A., " Approche expérimentale théorique de la conductivité thermique des milieux poreux humides," *Int. J. Heat Mass Transfer* **31**, 2305-2317 (1988).

Moyne, C., Batsale, J.-C., Degiovanni, A., and Maillet, D., "Thermal Conductivity of Wet Porous Media: Theoretical Analysis and Experimental Measurements," In: C.J. Cremers, H.A. Fine (Eds.), *Proceedings of Thermal Conductivity* **21**, 109-120 Plenum Press, Lexington, Kentucky, (1990).

Nagpure, S. C., and Bhushan, B., In Applied Scanning Probe Microscope Methods Biomimetics and Industrial Applications Vol. 13, (B. Bhushan and H. Fuchs, eds.) pp. 203-233, (Springer-Verlag, Heidelberg, Germany, 2009).

Nagpure, S. C., Bhushan, B., Babu, S. S., and Rizzoni, G., "Scanning Spreading Resistance Characterization of Aged Li-ion Batteries Using Atomic Force Microscopy," *Scripta Mater.* **60**, 933936 (2009).

Nagpure, S. C., Dinwiddie, R., Babu, S. S., Rizzoni, G., Bhushan, B., and Frech, T., "Thermal Diffusivity Study of Aged Li-ion Batteries Using Flash Method," *J. Power Sources* **195**, 872-876 (2010).

Nagpure, S. C., Babu, S. S., and Bhushan, B., "Surface Potential Measurement of Aged Li-ion Batteries Using Kelvin Probe Microscopy," *J. Power Sources* **196**, 1508-1512 (2011a).

Nagpure, S.C., Downing, R.G., Bhushan, B., Babu, S.S., and L. Cao, "Neutron Depth Profiling Technique for Studying Aging in Li-Ion Batteries," *Electrochimica Acta* **56(13)**, 4735-4743 (2011b).

Nagpure, S.C., Babu, S. S., Bhushan, B., Kumar, A., Mishra, R., Windl, W., Kovarik, L., and Mills, M., "Local Electronic Structure of $LiFePO_4$ Nanoparticles in Aged Li-Ion Batteries," *Acta Materialia* **59**, 6917-6926 (2011c).

Ohzuku, T., Ueda, A., and Yamamoto, N., "Zero-strain Insertion Material of $Li[Li_{1/3}Ti_{5/3}]O_4$ For Rechargeable Lithium Cell," *J. Electrochem. Soc.* **142**, 1431-1435 (1995).

Parker, W. J., Jenkins, R. J., Butler, C. P., and Abbott, G. L., "Flash Method of Determining Thermal Diffusivity, Heat Capacity, and Thermal Conductivity," *J. Appl. Phys.* **32**, 1679-1684 (1961).

Peled, E., "The Electrochemical Behavior of Alkali and Alkaline Earth Metals in Non-aqueous Battery Systems-The Solid Electrolyte Interphase Model," *J. Electrochem. Soc.* **126**, 2047-2051 (1979).

Peled, E., Golodnistsky, D., Menachem, C., and Bar-Tow, D., "An Advanced Tool for the Selection of Electrolyte Components for Rechargeable Lithium Batteries," *J. Electochem. Soc.* **145**, 3482-3486 (1998).

Perdew, J. P., Chevary, J. A., Vosko, S. H., Jackson, K. A., Pederson, M. R., Singh, D. J., and Fiolhais, C., "Atoms, Molecules, Solids, and Surfaces: Applications of the Generalized Gradient Approximation for Exchange and Correlation," *Phys. Rev. B* **46**, 6671-6687 (1992).

Philippi, I., Batsale, J.-C., Maillet, and D., Degiovanni, A., "Measurement of Thermal Diffusivity Through Processing of Infrared Images," *Rev. Sci. Instrum.* **66**, 182-192 (1995).

Ramond, L., Batsale, J.-C., Gobbe, C., and Quintard, M., "Measurement of a Thermal Exchange Coefficient in Porous Media by Infrared Thermography -Two Temperature Model Application," In: *Proceedings of 11t̂h Int. Heat Transfer Conference*, Kyong Ju Korea, (1998).

Ramond, L., Batsale, J.-C., and Gobbe, C., "Mesure de coefficient d'échange thermique en milieux hétérogčnes par thermographie infrarouge application d'un modčle a deux températures: Measurement of the Macroscopic Heat Transfer Coefficient in Heterogeneous Media by Infrared Thermography. A Two-temperature Model Application," *Int. J. Thermal Sci.* **38**, 250-257 (1999).

Rice, A., "Nanoscope Controller Manual," Rev. B, Veeco Instruments Inc., Santa Barbara, CA (2002).

Righini, F., and Cezairliyan, A., "Pulse Method of Thermal Diffusivity Measurements," *High Temp-High Press.* **5**, 481-501 (1973).

Saito, R., Takeya, T., and Kimura, T., "Raman Intensity of Single-wall Carbon Nanotubes," *Phy. Rev. B* **57**, 4145-4153 (1998).

Schwan, J., Ulrich, S., Bathori, V., Erhardt, H. , and Silva, S. R. P., "Raman Spectroscopy on Amorphous Carbon Films," *J. Appl. Phys.* **80**, 440-447 (1996).

Shearing, P. R., Howard, L. E., Jørgensen, P. S., Brandon, N. P., and Harris, S. J., "Characterization of the 3-Dimensional Microstructure of a Graphite Negative Electrode from a Li-ion Battery," *Electrochem. Commun.* **12**, 374-377(2010).

Sheindlin, M., Halton, D., Musella M., and Ronchi, C., "Advances in the Use of Laser-Flash Techniques for Thermal Diffusivity Measurement," *Rev. Sci. Instru.* **69**, 1426-1436 (1998).

Siegel, J. B., Lin, X., Stefanopoulou, A. G., Hussey, D. S., Jacobson, D. L., and Gorsich, D., "Neutron Imaging of Lithium Concentration in LFP Pouch Cell Battery," *J. Electrochem. Soc.* **158**, A523-A529 (2011).

Simon, P. and Gogotsi, Y., "Materials for Electrochemical Capacitors," *Nature Materials* **7**, 845-854 (2008).

Slater, K., Scanning Spreading Resistance Microscopy (SSRM)," Support Note No. 294 Rev. A, Veeco Instruments Inc., Santa Barbara, CA (2000).

Song, J. Y., Wang, Y. Y., and Wan, C. C., "Review of Gel-type Polymer Electrolytes for Lithium-ion Batteries," *J. Power Sources* **77**, 183-197 (1999).

Spagnol, P., Onori, S., Madella, N., Guezennec, Y., and Neal, J., "Aging and Characterization of Li-Ion Batteries in a HEV Application for Lifetime Estimation," *Proc. of IFAC Symposium Advances in Automotive Control,* (2010).

Srinivasan, V., and Newman J., "Discharge Model for the Lithium Iron-Phosphate Electrode," Lawrence Berkeley National Laboratory, LBNL-55444 (2004) Retrieved from: <http://escholarship.org/uc/item/7dq154dd>

Sturges, H. A., "The Coice of a Class-Interval," *J. Amer. Statist. Assoc.* **21**, 65-66 (1926).

Tamor, M. A., and Vassell, W. C., "Raman "fingerprinting" of Amorphous Carbon Films," *J. Appl. Phys.* **76**, 3823-3830 (1994).

Tang, P., and Holzwarth, N. A. W., "Electronic Structure of $FePO_4$, $LiFePO_4$ and Related Materials," *Phys. Rev. B* **68(16)**, 165107-165107-10 (2003).

Taylor R. E., "Heat-Pulsse Thermal Diffusivity Measurements," *High Temp-High Press.* **11**, 43-58 (1979).

Taylor R. E., and Maglić K. D., In: *Compendium of Thermophysical Property Measurement Methods* Vol. 1 *Survey of Measurement Techniques* pp 305 (Plenum, London, 1984).

Tucker, M. C., Reimer, J. A., and Cairns, E. J., "A ^{7}Li NMR Study of Lithium Insertion into Lithium Manganese Oxide Spinel," *Electrochem. Solid St.* **3**, 463-466 (2000).

Tucker, M. C., Doeff, M. M., Richardson, T. J, Fiñones, R., Reimer, J. A., and Cairnsa, E J., ^{7}Li and ^{31}P Magic Angle Spinning Nuclear Magnetic Resonance of LiFePO4-Type Materials," *Electrochem. Solid St.* **5**, A95-A98 (2002a).

Tucker, M. C., Doeff, M. M., Richardson, T. J., Fiñones, R., Cairns, E. J., and Reimer, J. A., "Hyperfine Fields at the Li Site in $LiFePO_4$-Type Olivine Materials for Lithium Rechargeable Batteries: A ^{7}Lii MAS NMR and SQUID Study," *J. Am. Chem. Soc.* **124**, 3832-3833 (2002b).

Tuinstra, F. and Koenig, J. L., "Raman Spectrum of Graphite," *J. Chem. Phys.* **53**, 1126-1130 (1970).

Tun, Z., Noël, J. J., Bohdanowicz, Th., Cao, L. R., Downing, R. G., and Goncharova, L. V., "Cold-neutron Depth Profiling As A Research Tool for The Study of Surface Oxides on Metals," *Can. J. Phys.* **88**, 751-758 (2010).

Ue, M., Mori, S., "Mobility and Ionic Association of Lithium Salts in a Propylene Carbonate-Ethyl Methyl Carbonate Mixed Solvent," *J. Electrochem. Soc.* **142**, 2577-2581 (1995) .

Verhoeven, V.W.J., de Schepper, I. M., Nachtegaal, G., Kentgens, A.P.M., Kelder, E. M., Schoonman, J., and Mulder, F. M., "Lithium Dynamics in $LiMn_2O_4$ Probed Directly by Two-Dimensional ^{7}Li NMR," *Phys. Rev. Lett.* **86**, 4314-4317 (2001).

Verma, P., Marie, P., and Novák, P., "A Review of the Features and Analyses of the Solid Electrolyte Interphase in Li-ion Batteries," *Electrochim. Acta* **55**, 6332-6341 (2010).

Vetter, J., Novák, P., Wagner, M. R., Veit, C., Möller, K. C., Besenhard, J. O., Winter, M., Wohlfahrt-Mehrens, M., Vogler, C., and Hammouche, A., "Ageing Mechanisms in Lithium-ion Batteries," *J. Power Sources* **147**, 269-281 (2005).

Vidano, R. and Fischbach, D. B., "New Lines in the Raman Spectra of Carbons and Graphite," *J. Am. Ceram. Soc.* **61**, 13-17 (1978).

Vozár, L., and Hohenauer, W., "Flash Method of Measuring the Thermal Diffusivity: A Review," *High Temp-High Press.* **35/36**, 253-264 (2003/2007).

Vozár, L., and Hohenauer, W., "Measurement of the Thermal Diffusivity by the Laser-Flash Method with Repeated Pulses," *High Temp-High Press.* **33(1)**, 9-16 (2001).

Whitney, S., Biegalski, S. R. F., Huang, Y. H., and Goodenough, J. B., "Neutron Depth Profiling Application to Lithium-ion Cell Research," *J. Electrochem. Soc.* **156**, A886-A890 (2009).

Whittingham, M.S., "Electrical Energy Storage and Intercalation Chemistry," *Science* **192**, 1126-1127 (1976).

Whittingham, M. S., "Lithium Batteries and Cathode Materials," *Chem. Rev.* **104**, 4271-4301 (2004).

Whittingham, M. S., "Materials Challenges Facing Electrical Energy Storage," *MRS Bulletin* **33**, 411-419 (2008).

Whittingham, M.S., Materials Challenges Facing Electrochemical Energy Storage: Batteries and Capacitors in Fundamentals of Materials for Energy and Environmental Sustainability (eds. D.S. Ginley and D. Cohen), Materials Research Society, Warrendale, PA (2011).

Wilcox, J. D., Doeff, M. M., Marcinek, M., and Kostecki, R., "Factors Influencing the Quality of Carbon Coatings on $LiFePO_4$," *J. Electrochem. Soc.* **154**, A389-A395 (2007).

Williams D. B., and Carter C. B., Transmission Electron Microscopy: A Textbook for Materials Science Vol. 1, First ed. (Plenum, New York and London, 2004).

Williams D. B., and Carter C. B., Transmission Electron Microscopy: A Textbook for Materials Science Vol. 4, First ed. (Plenum, New York and London, 2004).

Windl, W., Liang, T., Lopatin, S., and Duscher, G., "Modeling and Characterization of Atomically Sharp Perfect Ge-SiO_2 Interfaces," *Mater. Sci. Eng. B* **114-115**, 156-161(2004).

Winter, M., Besenhard, J. O., Albering, J. H., Yang, J. Y., and Wachtler, M., "Lithium Storage Alloys as Anode Materials in Lithium Ion Batteries," *Prog Batteries Battery Mater.* **17**, 208-213 (1998).

Xu, K., "Nonaqueous Liquid Electrolytes for Lithium-Based Rechargeable Batteries," *Chem. Rev.* **104**, 4303-4417 (2004).

Yamada, A., Chung, S. C., and Hinokuma, K., "Optimized $LiFePO_4$ for Lithium Battery Cathodes," *J. Electrochem. Soc.* **148**, A224-A229 (2001).

Yoshida, T., Takahashi, M., Morikaa, S., Ihara, C., Katsukaa, H., Shiratsuchi, T., and Yamaki, J., "Degradation Mechanism and Life Prediction of Lithium-ion Batteries," *J. Electrochem. Soc.* **153(3)**, A576-A582 (2006).

Zhang, X., Ross, Jr., P. N., Kostecki, R., Kong, F., Sloop, S., Kerr, J. B., Striebel, K., Cairns, E. J., and McLarnon, F., "Diagnostic Characterization of High Power Lithium-Ion Batteries for Use in Hybrid Electric Vechiles," *J. Electrochem. Soc.* **148**, A463-A470 (2001).

Zhang, S. S., Xu, K., and Jow, T. R., "Electrochemical Impedance Study on the Low Temperature of Li-ion Batteries," *Electrochim. Acta* **49**, 1057-1061 (2004).

Zhang, W.J., and, Miser, D.E., "Coalescence of Oxide Nanoparticles: In Situ HRTEM Observation," *J. Nanopart. Res.* **8(6)**, 1027-1032 (2006).

Zharin, A. L. and Rigney, D. A., "Application of the Contact Potential Difference Technique for On-line Rubbing Surface Monitoring (Review)," *Tribol. Lett.* **4**, 205-213 (1998).

Ziegler, J. F., Cole, G. W., and Baglin, J. E. E., "Technique for Determining Concentration Profiles of Boron Impurities in Substrates," *J. Appl. Phys.* **43**, 3809-3815 (1972).

Ziegler, J. F., Biersack, J. P., and Ziegler,M. D., SRIM - The Stopping and Range of Ions in Matter, Lulu Press Co., Morrisville, NC (2008).